Computational Aeroacoustics

in the Automotive Industry

Rocío Martín Navarrete

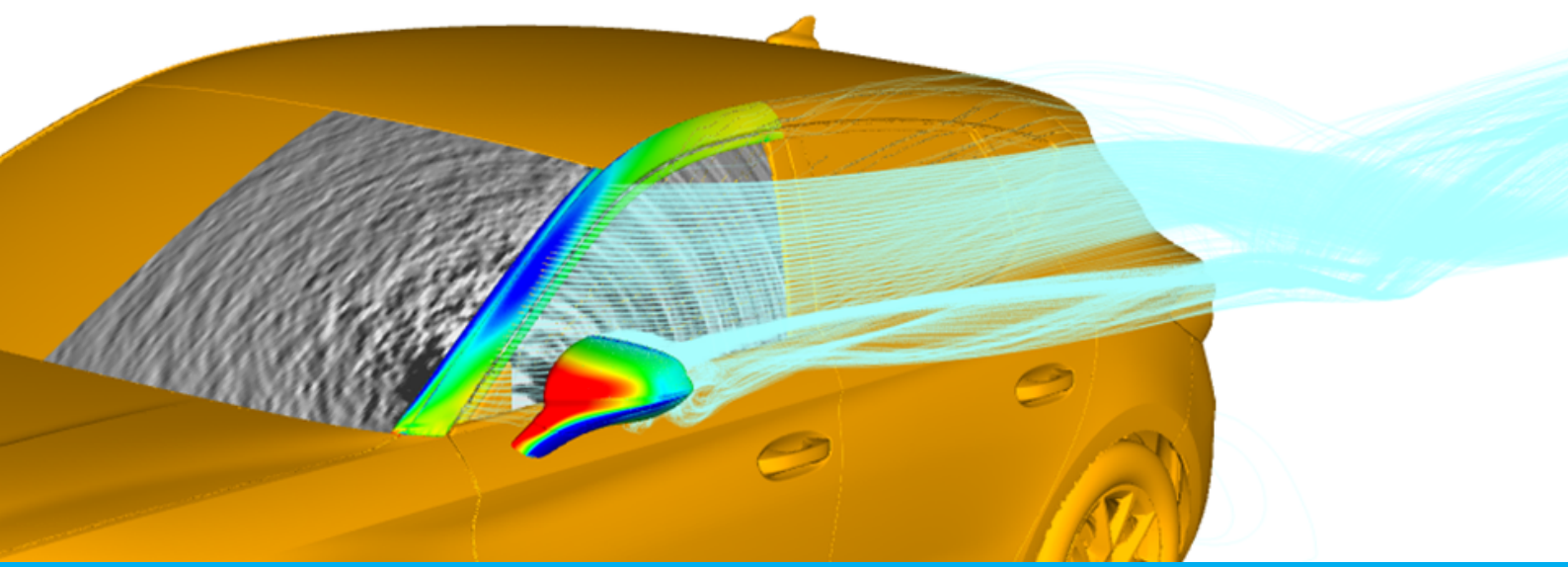

UNIVERSITAT POLITÈCNICA
DE CATALUNYA
BARCELONATECH

SEAT

UNIVERSITAT POLITÈCNICA
DE CATALUNYA
BARCELONATECH

Computational aeroacoustics in the automotive industry

by

Rocío Martín Navarrete

Computational Aeroacoustics

in the Automotive Industry

by

Rocío Martín Navarrete

A thesis submitted in fulfilment of the requirements
for the degree of Doctor
by the Universitat Politècnica de Catalunya.

PhD Candidate	**Rocío Martín Navarrete**	Department of Physics and Aerospace Division, School of Industrial, Aerospace and Audiovisual Engineering of Terrassa (ESEIAAT), Universitat Politècnica de Catalunya, BARCELONATECH
Supervisor/s	**Dr. Manel Soria Guerrero** **Dr. Juan Carlos Cante Teràn**	Department of Physics and Aerospace Division, School of Industrial, Aerospace and Audiovisual Engineering of Terrassa (ESEIAAT), Universitat Politècnica de Catalunya, BARCELONATECH
Company Supervisor	**Mr. Pere Vidal Pairot**	Whole Car Development Department, SEAT, S.A.

November 2020

UNIVERSITAT POLITÈCNICA DE CATALUNYA BARCELONATECH

SEAT

Thanks to mathematics, today I can flow on your equations.
Thanks to physics, today I can hear your world.
Thanks to engineering, today I can drive further.

Abstract

The acoustic field inside a car cabin for low driving speeds is dominated by the engine or the tire noise. However, for mid to high velocities, the noise generated by the interaction of the car with the external air becomes more relevant. The flow separation from the A-pillar or the side mirror generates strong pressure fluctuations which result in acoustic waves propagated to the interior via excitation of the side window or the windshield.

At each point of the flow field domain, the pressure is composed by the hydrodynamic pressure (i.e., the incompressible part of the flow field) and the acoustic pressure (i.e., the acoustic field associated to the compressible part of the flow field). For typical car speeds, the Mach number is so low that the fluctuations of the compressible part of the flow are much smaller than those of the incompressible part but their characteristic lengths and convection velocities have a higher correlation with the bending waves of the windows of the vehicle. As a consequence, it is usually accepted that the major part of the interior noise in the car cabin is generated by the compressible part of the external flow field arriving to the transmission surfaces. The distinction of the acoustic pressure from the total pressure on the window is not easily done neither experimentally nor computationally.

The present thesis is focused on the research of a suitable computational methodology that enables to obtain the acoustic pressure near the transmission surfaces. To this aim, an extensive review of the most popular methods for Computational Aeroacoustics is carried out in order to understand the physical mechanisms of sound generated by a fluid in motion around a solid body and the mathematical models that describe it based on the up-to-date available literature. Due to its simplicity, efficiency and usefulness, the so-called 'acoustic analogy' proposed by Curle as an extension of the theory developed by James Lighthill is chosen to evaluate the acoustic pressure of the cases of study within this dissertation.

In particular, among all the different components of a vehicle, the flow pattern and acoustic performance of very wide open cavities have been deeply analysed. Such cavities are very common in any type of ground vehicle designs for soiling management or manufacturing restrictions. However, this configuration is also known to be

the cause of conspicuous acoustic problems such as whistles. Its well defined tonal noise is known in the literature as Rossiter mode. The flow nature of this phenomena as well as its radiating pattern and response to different geometrical modifications (e.g., length of the cavity, radius of the trailing, leading and bottom edge or difference in heights between the left and right wall of the cavity) are addressed in this work. A particular feature of this configuration is the oscillatory mode: shear layer mode (SL) or wake mode (WM). For the parameters considered in the present dissertation it is seen that while in SL the flow shows a two-dimensional behaviour, in WM the flow is three-dimensional, resulting in significantly different sound sources. The computation of the acoustic pressure is done using Curle's formulation evaluated as a post-process of an unsteady incompressible three-dimensional Navier-Stokes solution and compared with the results obtained with Direct Simulation (DS). It is found that DS and Curle's analogy are in good agreement except in the wake area, where quadrupole acoustic sources are relevant. Regarding the evaluation of the passive noise control techniques, the results show that the modifications on the trailing edge are the most effective to control the flow. They allow to reduce the pressure fluctuations produced by the recirculation confined inside the cavity and the abrupt ejection of the flow at the trailing edge. As a consequence, the overall sound pressure level can be decreased up to 9dB. In summary, the complex behaviour of the cavity flow allows to fully understand the proposed model and also highlight its limitations.

Once the model has been validated for an isolated geometry, the application of the same method is extended to a real car geometry from the automotive company SEAT. The acoustic radiation to the side window and windshield of the side mirror and A-pillar of the vehicle is shown as an example of the potential of this procedure for aeroacoustic analysis and optimisation of a vehicle straight from the drawing table.

Keywords: Aeroacoustics; Automobile; Acoustic Analogy; Curle; DNS; LES; Numerical Simulation; Open Cavity.

Preface

This thesis has been done in candidature for a Ph.D degree at Universitat Politècnica de Catalunya and the content of this dissertation corresponds to the culmination of the research carried out during the last four years inside the research group TUAREG (TUrbulence and Aerodynamics Research Group) in collaboration with the automotive company SEAT S.A. Financial support has been obtained from the Industrial Doctorate project from the Government of Catalonia and was sponsored by the Agència de Gestió d'Ajuts Universitaris i de Recerca (AGAUR) and the company SEAT S.A (2016 DI068). The results were obtained thanks to the computational resources awarded by the competitive projects of Red Española de Supercomputación (RES, refs. FI-2018-3-0007, FI-2019-1-0016 and IM-2019-2-0025) in LaPalma and MareNotrum IV supercomputers. Moreover, part of this work has been possible thanks to the collaboration of the members of Kurchatov Institute (MCC NRC) and Barcelona Supercomputer Center (BSC), who kindly shared their computer resources as well as their technical support. The author thankfully acknowledges these institutions.

Furthermore, I would like to express my gratitude to my advisor Dr. Manel Soria for the continuous support during my Ph.D studies. Thank you for your patience, guidance and eloquence but foremost thank you for being a friend. I can not imagine all these years of research and writing of this thesis without your outstanding sense of humour and particular way of understanding life. Also, my most sincere gratitude to my co-supervisor Mr. Pere Vidal, for always believing in the opportunity of transferring academical knowledge into industrial context and trusting me to carry out such exciting challenge. I would also like to thank Dr. Juan Carlos Cante, for making possible this project and guide a new generation of aeronautical engineers.

I can not forget about my colleagues of the SEAT acoustics department. Thanks to the experienced ones for sharing your knowledge and to the youngsters for all the enthusiasm you transmit. Special mention to Mr. Ignacio Zabala and Mr. Joan Casas, for all the long conversations about aeroacoustics. I like to think that experiments and simulations are a bit closer now thanks to us.

My sincere thanks also goes to the outstanding CFD and CAA references I had

the opportunity to meet: Dr. Oriol Lehmkuhl, Dr. Ivette Rodriguez, Dr. Andrey Gorobets, Dr. Alexey Duben, Dr. Michael Hartmann, Dr. Alexandra Mutzke,... It has been an honour learning from all of you.

Also, to my fellow colleagues Dr. Arnau Mirò and Dr. David de la Torre. Since the first day of this adventure, your help has been immeasurable. I admire you and 'while(0)' you deserve all the success in your professional careers.

Finally, I would like to dedicate this work to my family and to my life partner, Jon. Vuestro amor incondicional es lo más valioso que tengo.

Contents

List of Figures

List of Tables

Symbols

a_0	=	sound speed in the fluid
C_D	=	cavity drag coefficient, $\frac{F_D}{\frac{1}{2}\rho_\infty U_\infty^2 DW}$
D	=	cavity depth
f	=	fundamental frequency
F_D	=	force contribution from the cavity walls
H	=	shape factor, $H = \frac{\delta^*}{\theta}$
L	=	cavity length
l	=	unitary vector pointing from source point to observation point.
$OASPL$	=	overall averaged sound pressure level, $20log_{10}\left(\frac{p'_{rms}}{p'_{ref}}\right)$
M	=	Mach number, $\frac{U_\infty}{a_0}$
p	=	pressure
p'_{rms}	=	root mean square of the acoustic pressure
p'_{ref}	=	reference acoustic pressure, $\sqrt{\rho_\infty a_0 \times 10^{-12}}$
n	=	surface normal vector pointing to the surface
$\mathcal{Q}$	=	second invariant of the velocity gradient tensor, $-\frac{1}{2}\frac{\partial u_i}{\partial x_j}\frac{\partial u_j}{\partial x_i}$
r	=	distance between an observer position and a source point
R_{ii}	=	autocorrelation coefficient
$Re_{D,L,\theta}$	=	Reynolds number, $\frac{U_\infty D}{\nu}$, $\frac{U_\infty L}{\nu}$, $\frac{U_\infty \theta}{\nu}$
St_L	=	Strouhal number based on L, $St_L = \frac{fL}{U_\infty}$
s	=	distance from the leading edge along the wall
t	=	time
TU	=	time units, $\frac{tU_\infty}{D}$
u	=	velocity in the streamwise direction
u^*	=	friction velocity
U_∞	=	freestream velocity
v	=	velocity in the cross-stream direction
W	=	cavity width
w	=	velocity in the spanwise direction
x	=	streamwise coordinate

y	=	cross-stream coordinate
y_n	=	wall normal coordinate
y^+	=	dimensionless wall-normal distance, $y^+ = \frac{u^* y_n}{\nu}$
z	=	spanwise coordinate
α	=	counterclockwise angle taken from the downstream wall of the cavity
δ^*	=	displacement thickness, $\int_0^{\delta_{99}} \left(1 - \frac{\rho(y_n)u(y_n)}{\rho_\infty U_\infty}\right) dy_n$
δ_{ij}	=	Kronecker delta
Δx^+	=	wall spacing in the x-axis, $\Delta x^+ = \frac{u^* \Delta x}{\nu}$
Δz^+	=	wall spacing in the z-axis, $\Delta z^+ = \frac{u^* \Delta z}{\nu}$
θ	=	momentum thickness, $\int_0^{\delta_{99}} \frac{\rho(y_n)u(y_n)}{\rho_\infty U_\infty} \left(1 - \frac{u(y_n)}{U_\infty}\right) dy_n$
μ	=	dynamic viscosity
ν	=	kinematic viscosity
ρ	=	density
ρ_∞	=	freestream density
$\tilde{t}$	=	retarded time, $t - r/a_0$

Abbreviations

APE	**A**coustic **P**erturbation **E**quations
BISPL	**B**and **I**ntegrated **S**ound **P**ressure **L**evel
CAA	**C**omputational **A**ero**A**coustics
CFD	**C**omputational **F**luid **D**ynamics
FW-H	**F**wocs **W**illiam **H**awkings
LEE	**L**inear **E**uler **E**quations
OASPL	**O**verall **A**veraged **S**ound **P**ressure **L**evel
PDE	**P**artial **D**ifferential **E**quations

1

Introduction

The noise generated by a flow is an area of research with increasing relevance due to its technological challenges and societal implications. According to the World Health Organisation, environmental noise exposure is responsible for a wide range of health effects such as cardiovascular disorders or sleep disturbances [3]. The increased awareness of the consequences of noise pollution on humans and other living beings is accelerating the creation of more stringent regulations to minimise its effects (e.g. Environmental Noise Directive (END) 2002/49/EC in Europe). This puts every industry under pressure to deliver new technologies that meet these requirements.

Research centres from all industries are facing the need of a better understanding of the acoustic performance of their technology. To mention a few examples, in the aeronautic industry continuous effort is devoted to the reduction of noise produced, among others, by landing gears [4, 5] or jets [6, 7]. In ground vehicles, due to the increase in speed and the reduction of the powertrain noise (especially in electric cars), aerodynamic noise is becoming an important reason of discomfort for passengers and many studies have lately been devoted to this issue. For instance, [8] studied the noise generated by different train roof configurations where the noise is dominated by the pantograph, the roof cavity and the insulation plates. In the automotive industry, a large amount of work has been done regarding the noise generated by the air flow around side mirrors, either as parts of a generic vehicle model [9, 10] or as simplifications of an isolated side mirror in form of a half cylinder or a hemisphere [11, 12]. Cavities are also common parts of vehicle designs and their acoustic performance is a key issue of comfort for passengers. To highlight a recent example where the indus-

trial relevance of cavity acoustics is pointed out, the noise generated by the rear door gap considered as a wide cavity with a small opening was studied numerically and experimentally in [13].

Vehicle manufacturers aim not only to improve and validate their products but also to leverage current technological advances to speed up their development processes. For this reason, Computational Aeroacoustics (CAA) has become a very appealing area of research since it allows to predict the noise generated by air flow excited systems in early stages of the design process. The aim of the present doctoral thesis is precisely to acquire the required expertise in the area of CAA in order to understand the physical mechanisms of sound generated by a fluid in motion around a vehicle and the mathematical models that describe it based on the up-to-date available literature.

The present dissertation is structured as follows. In Chapter 2, the reader can find a review of the most popular methods in CAA and an assessment of the most suitable one for the pursued purpose of this research. In Chapter 3, an extensive numerical study applied to a wide open cavity, considered as an ideal geometry modelling the gap between the windshield and the ceiling of a car is described. Chapter 4 explains how the aeroacoustics of a vehicle is typically determined during the current development process based on the experience of the experts in the sector and in the empirical evidences encountered during this research. The complete understanding of this process is essential to correctly identify how CAA can help to the industry. Chapter 5 summarises the main conclusions of this thesis and suggests some open points to continue with the research. Finally, in Chapter 6 a collection of the authored accepted and under review publications derived of this research is presented.

2

Mathematical Modelling of Aeroacoustics

In this section a review of the existing CAA methods and an assessment of the most suitable one for the automotive industry is made.

Computational aeroacoustic problems can be addressed from two general approaches: Direct Simulation (DS) and hybrid methods (Figure 2.1). DS is based on the solution of the compressible Navier-Stokes equations without using any modelling of the sound. This method is the most direct way to compute sound generation since the governing equations completely describe the physics of the problem. However, solving the full set of equations implies extreme computational costs, out of the scope for the majority of industrial applications. On the other hand, hybrid approaches are more affordable to predict aeroacoustic noise in an engineering context. These methods consist in the use of two different numerical solvers: an unsteady CFD tool as the sound source generator and an acoustic solver as the transport method. The acoustic solver can be based on the solution of a system of partial differential equations, such as Linear Euler Equations (LEE) [14, 15] or Acoustic Perturbation Equations (APE) [16], or as an integral method. The latter, frequently used in the industry, is mainly based on the work of James Lighthill, [17].

From a computational point of view, integral methods are less expensive and allow to have an explicit solution for the acoustic pressure, which has to be numerically evaluated from source terms obtained by the Navier Stokes solver. Two of the most widely used integral methods are the extension of Lighthill's theory for the interaction of the fluid with a surface at rest, known as Curle's solution [18], and for

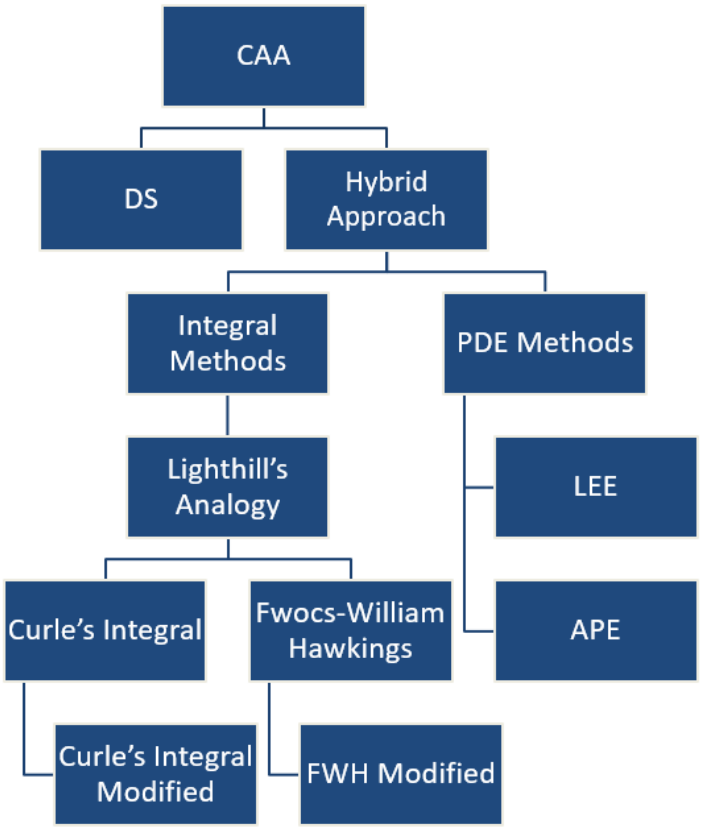

Figure 2.1: CAA Methods.

the interaction of the fluid with a surface in motion, Ffwocs-Williams and Hawkings (FW-H) solution [19].

This thesis has focused on integral methods and in order to understand the benefits and restrictions of their application, their mathematical formulations are derived in the remaining of the section. To this aim, it is important to first have some insight into DS and into the pioneering work of James Lighthill in the field of aeroacoustics.

2.1. Direct Simulation

The compressible Navier-Stokes equations are used to model the flow based in three basic principles of physics: the conservation of mass, conservation of momentum and conservation of energy. The mathematical expressions of these three laws under no external forces are written as:

$$\frac{\partial \rho}{\partial t} + \frac{\partial}{\partial x_i}\rho u_i = 0, \tag{2.1}$$

$$\frac{\partial}{\partial t}\rho u_j + \frac{\partial}{\partial x_i}(\rho u_i u_j + p_{ij} - \tau_{ij}) = 0, \tag{2.2}$$

$$\begin{aligned} &\frac{\partial}{\partial t}\left(\rho\left[e + \frac{U^2}{2}\right]\right) \\ &+\frac{\partial}{\partial x_i}\left(\rho\left[e + \frac{U^2}{2}u_i\right] - k\frac{\partial T}{\partial x_i} - u_i p_{ij} - u_1\tau_{i1} - u_2\tau_{i2} - u_3\tau_{i3}\right) - \rho\dot{q} = 0, \end{aligned} \tag{2.3}$$

where U is the modulus of the velocity vector, $\dot{q}$ is the rate of volumetric heat addition per unit mass, k is the thermal conductivity and τ_{ij} is the viscous stress tensor:

$$\tau_{ij} = \mu\left(\frac{\partial u_i}{\partial x_j} + \frac{\partial u_j}{\partial x_i} - \frac{2}{3}\frac{\partial u_k}{\partial x_k}\delta_{ij}\right). \tag{2.4}$$

The compressible Navier-Stokes equations describe both the flow field and the aerodynamically generated acoustic field, therefore, solving them, the latter could be obtained without the necessity of an additional model for the sound. For this reason, this approach is the most direct way to compute sound since the governing equations completely describe all the physics of the case. However, solving the complete set of equations implies extreme computational costs. Moreover, DS requires very high numerical resolution due to the large differences in the length scale between the acoustic pressure and the total pressure. Physically, the acoustic pressure, $p'(\mathbf{x},t) = p(\mathbf{x},t) - p_0$, is defined as the local pressure deviation from the ambient pressure caused by a sound wave. Due to the sensitive human perception of noise, the length scale of the acoustic pressure is usually much smaller than the hydrodynamic pressure (in air, the reference acoustic pressure is $p'_{ref} = 0.00002Pa$). Furthermore, in order to correctly capture the wave propagation, this method needs at least a few nodes per wavelength, so the mesh cannot be coarsen much outside the non-homogeneous region of the domain. Moreover, in order to avoid spurious pressure waves which interfere with the solution, the transition between different resolution areas has to be very smooth. As a result, the number of elements of the meshes is often very high. In addition, boundary conditions are specially critical due to the reflection of acoustic waves into the domain, usually forcing the use of artificial damping models. Some works done using DS are found in [2, 20–24].

2.2. Hybrid Approach

Hybrid methods combine two different numerical solvers: a purely CFD tool as the source generator and an acoustic solver as the transport method. Transport methods are usually divided into PDE methods and integral methods.

On one hand, PDE methods, such as LEE or APE, solve a system of PDEs, which describe the acoustic wave propagation in the entire field. The CFD solution is used as the exciting source for the system of PDEs solved in the CAA simulation. Owing to the change in discretization and resolution, proper coupling between the Navier-Stokes solver and the wave solver is a highly nontrivial task. In addition, due to the high computational costs, this method is not recommendable neither to compute a single observer's spectrum nor to simulate the far field. However, if an entire field sufficiently close to the non-homogeneous flow region has to be computed, this may be the most efficient approach.

On the other hand, integral methods integrate the relevant aerodynamic variables from the CFD simulation over a certain surface or volume to obtain the sound pressure at a certain observer in a certain time. These methods are based on the work of James Lighthill and they are often referred as 'analogies' since they intend to find the solution of a wave equation propagating in a medium at rest excited by sources generated from the region where the fluid is in motion. These methods are computationally simpler and allow to have an analytic solution for the acoustic pressure which has to be numerically evaluated from the source terms.

Overall, considering the advantages and disadvantages explained this far, integral methods are the most suitable approach for a great number of aeroacoustic problems in the automotive industry and, thus, it is the methodology chosen for the cases of study within this thesis.

2.2.1. Lighthill's Analogy

In 1952, James Lighthill initiated the theory of aeroacoustics publishing his celebrated work '*On sound generated aerodynamically*' [17]. Lighthill started out with the compressible expression of the continuity and momentum equations in the form of Equations 2.1 and 2.2 and in a genuinely but simply way manipulated them to obtain an inhomogeneous wave equation, which by definition describes the acoustic field. The steps followed were:

1. derive the continuity equation with respect to time;
2. derive the momentum equation with respect to x_i;
3. subtract the resulting expression from step 2 to the expression from step 1;
4. subtract the term $\frac{\partial^2}{\partial x_i \partial x_j}(a_0^2 \rho \delta_{ij}) = a_0^2 \nabla^2 \rho$ from both sides of the resulting equation of step 3.

Indeed, the expression obtained was:

$$\frac{\partial^2 \rho}{\partial t^2} - a_0^2 \nabla^2 \rho = \frac{\partial^2 T_{ij}}{\partial x_i \partial x_j}, \tag{2.5}$$

where $T_{ij} = \rho u_i u_j + p_{ij} - a_0^2 \rho \delta_{ij} - \tau_{ij}$ is known as the Lighthill's stress tensor. Lighthill showed that it is sufficient to assume that $T_{ij} \approx \rho_\infty u_i u_j$ when considering low subsonic, isentropic and inviscid flow.

Equation 2.5 is an inhomogeneous wave equation which was already solved by Stratton in 1941 [25]. The analytical solution of a general inhomogeneous wave equation is given by the next proposition. The reader can find its proof in Appendix A.

Proposition 1. *Let $g(x,y,z,t)$ be an homogeneous source function defined inside a closed domain V bounded by a regular surface S. Let ψ be a scalar potential excited by g. Then, ψ satisfies the inhomogeneous wave equation:*

$$\nabla^2 \psi - \frac{1}{v^2} \frac{\partial^2 \psi}{\partial t^2} = -g(x,y,z,t). \tag{2.6}$$

The solution of Equation 2.6 at a point $(x',y',z',t) \in V$ is:

$$\begin{aligned} \psi(x',y',z',t) - \psi_0 = & \frac{1}{4\pi} \int_V \frac{1}{r} [g] dV \\ & + \frac{1}{4\pi} \int_S \left(\frac{1}{r} \left[\frac{\partial \psi}{\partial n} \right] + \frac{[\psi]}{r^2} \frac{\partial r}{\partial n} + \frac{1}{vr} \frac{\partial r}{\partial n} \left[\frac{\partial \psi}{\partial t} \right] \right) dS, \end{aligned} \tag{2.7}$$

where $[*]$ means the evaluation of the function at the retarded time $\tau = t - \frac{r}{v}$, n is the surface normal vector pointing to the surface and:

$$r = \sqrt{\sum_i (x_i - x_i')^2}. \tag{2.8}$$

Using the last result, the solution of Equation 2.5 can be written as:

$$\boxed{\begin{aligned}\rho(x,y,z,t)-\rho_0 = &\frac{1}{4\pi a_0^2}\int_V \frac{1}{r}\left[\frac{\partial^2 T_{ij}}{\partial y_i \partial y_j}\right] dV \\ &+ \frac{1}{4\pi}\int_S \left(\frac{1}{r}\left[\frac{\partial \rho}{\partial n}\right] + \frac{[\rho]}{r^2}\frac{\partial r}{\partial n} + \frac{1}{a_0 r}\frac{\partial r}{\partial n}\left[\frac{\partial \rho}{\partial t}\right]\right) dS,\end{aligned}} \tag{2.9}$$

where it has been considered:

$$g(x,y,z,t) = \frac{1}{a_0^2}\frac{\partial^2}{\partial x_i \partial x_j}(\rho v_i v_j + p_{ij} - a_0^2 \rho \delta_{ij} - \tau_{ij}) \ , \ \psi(x',y',z',t) = \rho(x,y,z,t).$$

2.2.2. Curle's Analogy.

In 1955, Curle published his investigations in '*The influence of solid boundaries upon aerodynamic sound*' [18]. In his work, Curle extended Lighthill's theory rewriting the solution of Equation 2.5 when the boundary of the domain includes a solid surface. To this aim, Curle considered the Equation 2.9 and made it dependent on the position of the observer instead of the position of the noise source by developing the volume integral and simplifying the surface integral. Equation 2.10 was the final expression obtained and its complete mathematical deduction is provided in Appendix B.

$$\boxed{\rho(\mathbf{x},t) - \rho_0 = \frac{1}{4\pi a_0^2}\frac{\partial^2}{\partial x_i x_j}\int_V \frac{[T_{ij}]}{r} dV + \frac{1}{4\pi a_0^2}\frac{\partial}{\partial x_i}\int_S \frac{n_j}{r}[p_{ij} - \tau_{ij}] dS.} \tag{2.10}$$

However, the evaluation of Equation 2.10 from a CFD simulation is not straightforward and further mathematical manipulations should be done. Many works of the literature have followed the procedure done by Myers and Farassat in [26] to modify the solution of Kirchhoff's formula [27], primarily used in the theory of diffraction of light and in other electromagnetic problems. Such modification consists on taking the spatial derivatives inside the integral and to transform them into time derivatives. Therefore, omitting the viscous term and expressing ρ in terms of p (assuming that the flow is isentropic), the final expression to compute the acoustic pressure is:

$$\boxed{\begin{aligned} p(\mathbf{x},t) - p_0 = \frac{1}{4\pi}\int_V \left(\frac{l_i l_j}{a_0^2 r}[\ddot{T}_{ij}] + \frac{3l_i l_j - \delta_{ij}}{a_0 r^2}[\dot{T}_{ij}] + \frac{3l_i l_j - \delta_{ij}}{r^3}[T_{ij}]\right) dV \\ + \frac{1}{4\pi}\int_S -l_i n_j \left(\frac{1}{r a_0}[\dot{p}_{ij}] + \frac{1}{r^2}[p_{ij}]\right) dS. \end{aligned}} \tag{2.11}$$

The detailed deduction of Equation 2.11 can be found in Appendix B.1.

As aforementioned, acoustic analogies intend to model the problem obtaining a wave equation propagating in an homogeneous medium excited by sources arising from the non homogeneous region. In this case, Equation 2.11 accounts for two type of sources: a quadrupole source arising from the volume integral and a dipole source arising from the surface integral. Curle showed that for low Mach numbers quadrupoles sources are less efficient producing acoustic waves than monopoles or dipoles sources. In particular, it was seen that under this condition the relation between the acoustic power generated by quadrupoles and dipoles is:

$$\frac{P_{quad}}{P_{dip}} \approx M^2. \tag{2.12}$$

Indeed, Larsson et al. [23] numerically confirmed that the contribution of the source terms inside the volume integral for an open cavity at $M = 0.15$ was orders of magnitude smaller than the source terms inside the surface integral. Therefore, many works reduce Curle's formulation to a surface integral, which is especially convenient since the computation of the volume integral is very expensive and memory demanding. Therefore, if volume sources are considered negligible Equation 2.11 simplifies to:

$$\boxed{p(\mathbf{x},t) - p_0 = \frac{1}{4\pi}\int_S -l_i n_j \left(\frac{1}{r a_0}[\dot{p}_{ij}] + \frac{1}{r^2}[p_{ij}]\right) dS.} \tag{2.13}$$

The simplicity of Equation 2.13 together with the information provided about the contribution of each point of the surface to the total acoustic intensity (highlighting the parts of a design that can be potentially optimised) makes Curle's approach very popular for industrial applications. Nevertheless, in Curle's formulation, special attention needs to be paid to the compactness of the body. As previously mentioned, the surface integral of Equation 2.13 acts as a distribution of dipole sources located on solid boundaries and radiating noise with free field properties. This analogy does not take into account phenomena related with acoustic scattering, such as reflection or diffraction [28]. Mathematically, the acoustic compactness is defined in terms of the Helmholtz number [29]:

$$He = \frac{2\pi f D}{a_0} < 1. \tag{2.14}$$

In physical terms, last expression means that when the acoustic wavelength is smaller than the source body, properties of acoustic scattering cannot be reproduced by Equation 2.13. Despite being out of the scope for this thesis, there exist some work in the literature which propose modified formulations to take into account these phenomena [28, 30].

2.2.3. Ffwocs Williams and Hawkings' Analogy

In 1969, J.E. Ffwocs Williams and D.L. Hawkings [19] generalized Lighthill's solution for equivalent sources arising from moving surfaces immersed in the flow. To this aim, the authors assumed that the unbounded fluid region was partitioned into two regions separated by a continuous arbitrary surface, S_F (defined by the implicit function $f(\mathbf{x},t) = 0$), moving at velocity v as sketched in Figure 2.2. This surface was thought as a fictitious separation surface enclosing most of the strong nonlinear structures of the flow so the homogeneity assumption could be made outside S_F. The non-homogeneous region of the flow was artificially replaced by an equivalent distribution of mass and momentum sources describing the acoustic waves generated inside S_F and propagated to the exterior.

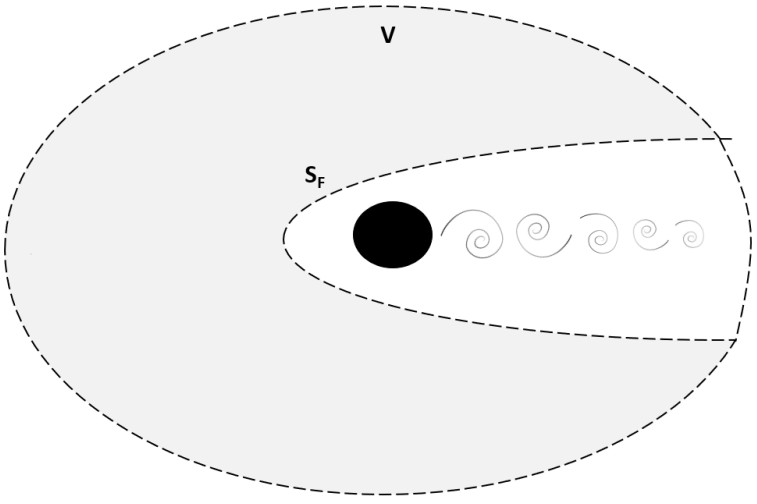

Figure 2.2: Surface definition in FW-H's Formulation.

Indeed, let us consider the continuity equation with the addition of the term $\frac{\partial \rho_\infty}{\partial t} = 0$ and multiply it by the heaviside step function $H(f)$:

$$\frac{\partial(\rho - \rho_\infty)}{\partial t} H(f) + \frac{\partial \rho u_i}{\partial x_i} H(f) = 0.$$

Using the chain rule, last equation can be rewritten as:

$$\frac{\partial(\rho - \rho_\infty)H(f)}{\partial t} - (\rho - \rho_\infty)\frac{\partial H(f)}{\partial t} + \frac{\partial \rho u_i H(f)}{\partial x_i} - \rho u_i \frac{\partial H(f)}{\partial x_i} = 0.$$

After rearranging the terms and taking into account that f satisfies $\frac{\partial f}{\partial t} + v_i \frac{\partial f}{\partial x_i} = 0$, the continuity equation becomes

$$\frac{\partial(\rho - \rho_\infty)H(f)}{\partial t} + \frac{\partial \rho u_i H(f)}{\partial x_i} = Q|\nabla f|\delta(f), \tag{2.15}$$

where $Q = (\rho_\infty v_i + \rho(u_i - v_i))n_i$.

With a similar process, the momentum equation becomes

$$\frac{\partial \rho u_i H(f)}{\partial t} + \frac{\partial \rho u_i u_j H(f)}{\partial x_j} + \frac{\partial p H(f)}{\partial x_i} - \frac{\partial \tau_{ij} H(f)}{\partial x_j} = F_i|\nabla f|\delta(f), \tag{2.16}$$

where $F_i = (\rho u_i(u_j - v_j) + p\delta ij - \tau_{ij})n_j$.

As done with Lighthill's equation, a mathematical manipulation of the rewritten continuity and momentum equations 2.15 and 2.16 leads to an analogous wave equation:

$$\left(\frac{\partial^2}{\partial t^2} - a_0^2 \frac{\partial^2}{\partial x_i^2}\right)(\rho - \rho_\infty)H(f) = \frac{\partial^2 T'_{ij} H(f)}{\partial x_i \partial x_j} - \frac{\partial F_i |\nabla f|\delta(f)}{\partial x_i} + \frac{\partial Q|\nabla f|\delta(f)}{\partial t}, \tag{2.17}$$

where $T'_{ij} = \rho u_i u_j - \tau_{ij} + (p - a_0^2(\rho - \rho_\infty))\delta_{ij} = T_{ij} + a_0^2 \rho_\infty \delta_{ij}$.

The solution of Equation 2.17 is derived in Appendix C. Its expression is:

$$\begin{aligned} \rho(\mathbf{x},t) - \rho_0 = {} & \frac{1}{4\pi a_0^2}\frac{\partial^2}{\partial x_i \partial x_j}\int_V \frac{[T'^*_{ij}]}{r(1 - \frac{l j v_j}{a_0})} dV \\ & - \frac{1}{4\pi a_0^2}\frac{\partial}{\partial x_i}\int_{S_F} \frac{[F_i^*]}{r(1 - \frac{l j v_j}{a_0})} dS_F \\ & + \frac{1}{4\pi a_0^2}\frac{\partial}{\partial t}\int_{S_F} \frac{[Q^*]}{r(1 - \frac{l j v_j}{a_0})} dS_F, \end{aligned} \tag{2.18}$$

where,

$$T'^{*}_{ij} = \rho(u^*_i + v_i)(u^*_j + v_j) - \tau^*_{ij} + (p - a_0^2(\rho - \rho_\infty))\delta_{ij}, \tag{2.19}$$

$$F^*_i = -(\rho(u^*_i + v_i)u^*_j + p\delta_{ij} - \tau^*_{ij})n_j, \tag{2.20}$$

$$Q^* = -(\rho_\infty v_i + \rho u^*_i)n_i. \tag{2.21}$$

As it was done in Curle's formulation, it is recommendable to take the derivatives inside the integral and transform spatial derivatives into time derivatives. Thus, after neglecting the volume sources and considering that the body is at rest, Equation 2.18 transforms to:

$$\boxed{\begin{aligned} p(\mathbf{x},t) - p_0 = -\frac{1}{4\pi}\Bigg(&\int_{S_F} l_i n_j \left(\frac{1}{r a_0}[\dot{p}_{ij}] + \frac{1}{r^2}[p_{ij}]\right) dS_F \\ &+ \int_{S_F} l_i n_j \left(\frac{1}{r a_0}\left[\frac{\partial(\rho u_i u_j)}{\partial \tau}\right] + \frac{1}{r^2}[\rho u_i u_j]\right) dS_F \\ &+ \int_{S_F} \frac{n_j}{r}\left[\frac{\partial(\rho u_j)}{\partial \tau}\right] dS_F\Bigg). \end{aligned}} \tag{2.22}$$

May the reader notice that in the limit case when the surface of integration in FW-H's formulation coincides with the solid surface of the body at rest, the expression 2.22 reduces to Curle's formulation expressed in Equation 2.13.

Overall, for the cases of study within this thesis, the relative position between the source and the observer is always constant, $\mathbf{v} = 0$, and the Mach number is low (around $M = 0.1$). Hence Curle's analogy considered in the form of Equation 2.13 will be the most suitable method to be applied for the cases presented.

3

Cavity Noise

3.1. Introduction

A broad body of literature has been devoted to cavity noise generation over the last decade. A significant fraction of the studies deals with finite width cavities in presence of high subsonic and supersonic flows, that are of interest for aerospace applications. The side walls of a finite width cavity are known to play an important role in the flow dynamics. Sun et al. [31] studied their effect by analysing spanwise-periodic and finite-span cavity flows at $Re_D = 10^4$ and $M = 0.6$ for a cavity of aspect ratio $L/D = 6$, finding significant differences in the flow behaviour. In particular, the authors pointed out that the side walls bend the shed vortex detached from the leading edge, triggering its earlier break into smaller vortices and reducing the root mean square of the pressure by approximately 30%. While sound radiation was not addressed in their paper, this is also likely to be significantly reduced. Lai and Luo [32] studied the acoustic radiation of a cavity with dimensions $L/D = 5$ and $W/D = 1$ at $Re_L = \frac{\rho_\infty U_\infty L}{\mu} = 1.36 \times 10^6$ and $M = 0.85$ using FW-H formulation. The authors concluded that the directivity of the sound waves was correctly captured by the acoustic analogy but some significant discrepancies (in the order of 10 dB) among DS and FW-H solutions occurred in the near field. Kuhn et al. [33] also studied the open cavity for low Mach number, $M = 0.1$, at $Re_\theta = 8300$ with geometrical parameters $L/D = 0.5$ and $W/D = 0.6$ using DS. A good agreement was found between the experiments and the numerical results, which correctly predicted the frequency spectrum up to 10kHz.

Because of the industrial application of this work, this thesis considers very wide

open cavities with no interaction between the flow and the side walls. Some of the first computations of acoustic radiation for very wide cavities assumed the flow to be two-dimensional. Hardin and Pope [34] calculated the sound generated by an open cavity with aspect ratio $L/D = 4$, at Reynolds number based on the cavity length $Re_L = 5000$ and Mach number $M = 0.1$. They concluded that the cavity flow undergoes a characteristic regular oscillation which leads to the radiation of tonal noise. The open cavity with the same aspect ratio at $Re_D = 1500$ and $M = 0.15$ was studied by Larsson et al. [21]. The authors confirmed that Curle's solution based on a compressible simulation was in good agreement with DS for observers located in the far field. They also found that the contribution of the wall pressure fluctuations accounted for approximately 90% of the radiated intensity. Ask and Davidson [2, 22] extended this study evaluating Curle's integral based on an incompressible simulation, also finding acceptable results though highlighting the sensitivity of Curle's equation to the size of the domain.

Regarding the assumption of a two-dimensional flow, Brès and Colonius [35] numerically showed that for cavities of aspect ratio $L/D = 4$, the transition to three-dimensional flow occurred at $Re_D \approx 1200$, in agreement with previous experimental data by Faure at al. [36]. As it will be presented in Section 3.4.1 the assumption of a two-dimensional flow for our case of study can produce unrealistic results. In a two-dimensional simulation, the vortical structures formed in the cavity trailing edge travel downstream almost unaltered and attached to the wall of the domain due to the absence of the vortex stretching mechanism. As a consequence, the pressure value over the wall changes completely, predicting too high acoustic radiation.

Another important aspect of the cavity flow is the oscillation mode. Gharib and Roshko [37] experimentally found that, depending on the development of the boundary layer at the cavity inlet, there are two different oscillation modes (in addition to a non-oscillating mode): shear layer (SL) and wake mode (WM). Later, Colunius et al. [38, 39] numerically determined the transition between modes using a compressible flow solver for cavities with aspect ratios ranging from $L/D = 1$ to $L/D = 5$ and a wide range of Re_θ values. The transition from SL to WM is obtained as L/θ or Re_θ increase. On one hand, the SL mode is characterised by a feedback loop between the large-scale vortex shedding at the leading edge of the cavity and the acoustic waves generated at the trailing edge and then travelling upwards. On the other hand, the WM is characterised by a more energetic large-scale vortex shedding and a more violent ejection at the trailing edge of the shedding vortices towards the downstream wall. While in the SL mode the acoustic waves play an important role for the self-

sustained oscillations in the cavity, these are no longer involved in the WM flow [38, 40]. In Section 3.4.1, the results of a series of incompressible simulations near the transition between SL and WM are shown, proving that in SL the flow oscillations decay if an incompressible model is used due to the absence of acoustic waves in the solution. Thus, in SL mode, even at very low Mach numbers, a compressible model is needed to correctly describe the flow physics.

As can be seen, the understanding of the physical mechanism producing noise in cavities has attracted a lot of attention due to the wide range of real-world applications. For this reason, many works have also been devoted to the creation of control mechanisms that suppress the generation of such noise. These mechanisms are usually classified into active control mechanisms [41–47] based on flow injection or suction, which significant and continuously change the dynamics of the flow in the cavity and passive mechanisms [48–57] based on permanent geometrical modifications such as spoilers mounted in the leading edge or trailing edge slants. Passive noise control mechanisms are usually simpler but very effective in noise reduction. For this reason, the aim of this thesis is also to study different cavity geometries that optimise the acoustic performance of cavities in vehicle designs.

Among some of the works done using active noise control, Lamp and Chokani [46] studied the effectiveness of controlling noise via flow injection through a small jet placed within the upstream wall of a cavity with $L/D = 4.33$ at supersonic speed, $M = 1.75$, and $Re_D = 5.58 \times 10^7$. The two-dimensional numerical results showed that the suppression depended on the amplitude and frequency of the jet injection. In particular, a larger blowing rate provided the greatest reductions. Suponitsky et al. [41] also focused on an active control technique based on simultaneous injection and suction through the front and rear walls of a cavity with $L/D = 4$ at $Re_D = 5000$ considering the limit case where $M = 0$. The results showed that the major effect of the control technique was the reduction of the reverse flow inside the cavity and, for injection levels exceeding a certain threshold value, the tonal noise was nearly vanished. A different approach of active noise control was experimentally addressed by Fabris and Williams [47] for a cavity with aspect ratio $L/D = 4$ and $M = 0.15, 0.23$ for $Re_D = 4.4 \times 10^5, 6.7 \times 10^5$. The technique consisted on the forcing of the shear layer by means of an acoustic perturbation produced by three speakers located below the inlet wall, showing that an acoustic disturbance was also capable of perturbing the system and its acoustic response.

With respect to passive noise control techniques, Saddington et al. [48] experimentally tested different trailing and leading edge configurations for a finite cavity

with $L/D = 5$ and $W/D = 2$ at $Re_D = 1.31 \times 10^7$ and $M = 0.71$. The control technique was based on the addition of different geometries such as spoilers, ramps or steps, reaching the conclusion that these devices were more effective when attached to the leading edge as a consequence of the shear layer being deflected away from it by the spoiler. Other authors such as Knowles et al. [49] (experimental work with $L/D = 4$ at $M = 0.85$ and $Re_D = 4.9 \times 10^5$) or Mancini and Kolb [52] (numerical work with $L/D = 5$ at $M = 0.8, 1.35$ and $Re_D = 1.29 \times 10^7, 2.2 \times 10^7$) varied the yaw angle of the front and rear walls of the cavity. Both authors concluded that the effectiveness in cavity tones suppression was only significant when the angle of rotation of the rear wall was greater than 15 degrees. Hao et al. [58] studied the effect of the cavity length ($L/D = 1, 4, 8$) and the trailing edge height with respect to the leading edge height, ($h/D = -0.5, 0, 1$) when the incoming boundary layer is turbulent, $Re_\theta = 4755$. The authors observed that the acoustic field increased with gap width and trailing-edge height. These geometrical parameters will also be studied in this work.

The results presented in this chapter focus on wide open cavities with no interaction between the flow and the side walls at low subsonic speeds. Firstly, the study is focused on the methodological aspects of the case. To this aim, a cost-effective Reynolds number is considered, $Re_D = 1500$, for a baseline cavity with aspect ratio $L/D = 4$. Under these conditions, the following points are deeply studied:

1. **Dimensional behaviour of the flow:** at $Re_D = 1500$, only slightly above the transition point, the flow is three-dimensional. In this study, it is presented an investigation of the effects of such structures on the sound generation with respect to a two-dimensional model using an incompressible simulation together with Curle's integral at $M = 0.15$;

2. **Oscillation mode:** SL and WM oscillation modes are analysed in order to understand the role of the acoustic feedback mechanism (missing in incompressible simulations) at $M = 0.15$;

3. **Compressibility effects:** DS and Curle's analogy acoustic results are compared in order to understand how the acoustics in the near field is affected by quadrupole sources at $M = 0.1$;

Once the advantages and limitations of the proposed method are defined and well understood, the investigation focuses on a more realistic case for the industrial application contemplated. To this aim, the Reynolds number is increased up to $Re_D = 5000$ and the following analysis are addressed:

1. **Reynolds number influence:** the effect of Re_D on the flow and acoustic fields is evaluated comparing the results of $Re_D = 1500$ with the results of $Re_D = 5000$ at $M = 0.1$;

2. **Passive noise control techniques:** a reduction of the aeroacoustic noise radiated by the baseline cavity at $Re_D = 5000$ and $M = 0.1$ is intended by means of seven different passive noise control techniques based on the modification of the length of the cavity, the radius of the leading edge, the radius of the trailing edge, the radius of the right bottom edge and the distance in the y-axis between the leading and trailing edge.

In the context of the automotive industry, for the Mach number considered, $M = 0.1$, and the speed of sound at standard sea-level conditions, $a_0 = 340m/s$, the car velocity would correspond to $U_\infty \approx 120Km/h$. This value is around the usual speed of vehicles during their design development process. Therefore, the geometrical parameters of the cavities being considered in this study for $Re_D = 1500$ and $Re_D = 5000$ would be $D = 0.7mm$ and $D = 2.2mm$ respectively. These dimensions correspond to usual gaps found in different external parts of cars, e.g, side mirrors, roofs or doors.

3.2. Case Description

The present work considers very wide open cavities in presence of an upstream laminar flow, as sketched in Figure 3.1. The flow conditions of all the cases studied together with the CFD and CAA methods used to solve the physics of each case are listed in Table 3.1.

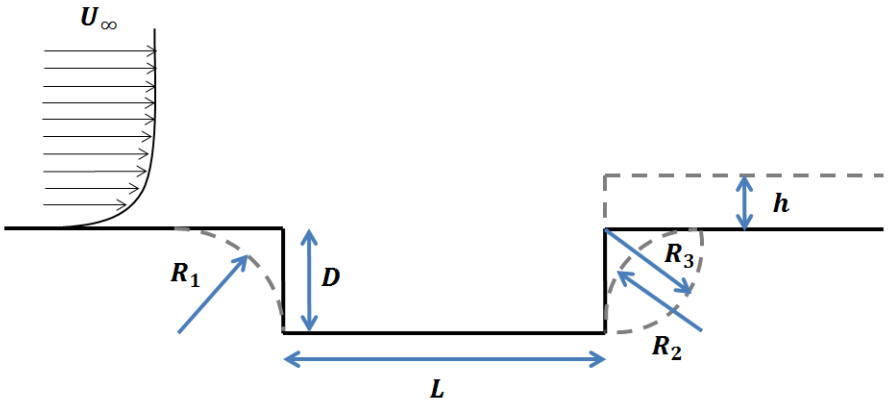

Figure 3.1: Geometry of the cavity and parameters of modification.

Case	Re_D	M	L/θ	Mode	CFD	CAA
2D-WM	1500	0.15	79	WM	2-dimensional incompressible DNS	Curle
3D-SL	1500	0.15	72	SL	3-dimensional incompressible DNS	Curle
3D-WM	1500	0.15	101	WM	3-dimensional incompressible DNS	Curle
1500	1500	0.10	101	WM	3-dimensional incompressible DNS	Curle
1500-C	1500	0.10	101	WM	3-dimensional compressible DNS	DS
5000	5000	0.10	172	WM	3-dimensional incompressible LES	Curle

Table 3.1: Flow conditions and computational methods for the cases under study.

Along all the chapter, the baseline case is a rectangular cavity with $L/D = 4$. The cavity noise control study is only made for $Re_D = 5000$. The geometrical parameters under consideration are the length of the cavity, L, the radius of the leading edge, R_1, the radius of the trailing edge, R_2, the radius of the right bottom edge, R_3, and the distance in the y-axis between the leading and trailing edge, h. The list of the geometrical modifications simulated is given in Table 3.2. The modification C8 is not expected to perform better acoustically but it will arise deeper knowledge on the effect of the parameter h.

As aforementioned, the thickness of the boundary layer arriving at the leading edge of the cavity can substantially change the behaviour of the flow in the cavity. Colonius et al. [38] established the transition between shear layer (SL) and wake mode (WM) for $Re_\theta = 58.6$ at $L/\theta \approx 75$. In the present work, for the WM cases a non-dimensional uniform free-stream velocity, $U_\infty = 1$, is imposed at the inlet boundary which is located $8D$ units before the cavity leading edge. For the SL case, the Blasius solution for a flat plate [1] developed during $x = 4D$ at the inlet boundary is imposed. Under these conditions, the boundary layer profile is developed along the inlet wall and arrives to the leading edge with the values of L/θ listed in Table 3.1, defining the oscillating mode for each case.

No-slip boundary conditions are applied at solid boundaries. At the outflow and top boundaries, zero normal derivatives for the velocity and p are considered. However, in order to damp the two-dimensional vortical structures at the outlet of the domain for the case 2D-WM, a buffer zone is imposed for the last 10 mesh elements. Finally, to account for the infinity of the cavity in the spanwise direction, periodic boundary conditions have been imposed at the front and back boundary surfaces.

Case	L/D	h/D	R_1/D	R_2/D	R_3/D	Geometry
C1	4	0	0	0	0	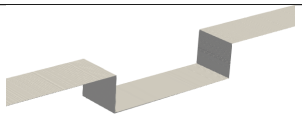
C2	2	0	0	0	0	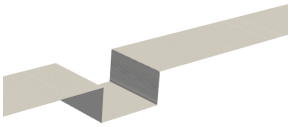
C3	4	0	1	0	0	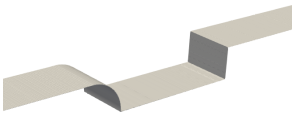
C4	4	0	0	1	0	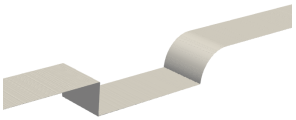
C5	4	0	0	0.5	0	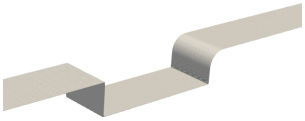
C6	4	0	0	0	1	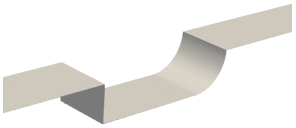
C7	4	-0.5	0	0	0	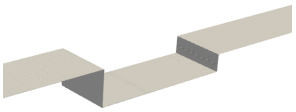
C8	4	0.5	0	0	0	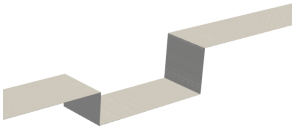

Table 3.2: Geometrical parameters of the cases studied. The parameters L, h, R_1, R_2 and R_3 are defined in Figure 3.1.

3.3. Computational Methods

3.3.1. CFD Code

The CFD code used to solve the incompressible Navier-Stokes equations is Alya, developed at Barcelona Supercomputing Center [59]. In the Alya code, the convective term is discretised using a non-dissipative Galerkin Finite Element Method (FEM) scheme recently proposed by Charnyi et al. in [60], which conserves linear/angular momentum and kinetic energy at a discrete level. Neither an upwinding scheme nor equivalent momentum stabilisation is used. In order to use equal-order elements, numerical dissipation is introduced only for the pressure stabilisation via a fractional

step scheme [61], which is similar to approaches for pressure-velocity coupling in the codes based on collocated finite volume methods for unstructured meshes [62]. This approach was shown to be significantly less dissipative compared to traditional stabilised FEM approach [63]. Temporal discretization is performed through a conservative explicit third-order Runge-Kutta scheme [64].

The NOISEtte code [65] has been used for the compressible simulation at $Re_D = 1500$. It is based on the finite-volume EBR (Edge-Based Reconstruction) schemes [66] for unstructured hybrid meshes. This schemes provide higher accuracy than most Godunov-type second order schemes at a low computing cost. On translationally-invariant (structured) mesh zones the EBR schemes coincide with high-order (up to sixth) finite-difference schemes. An implicit second order scheme with Newton linearization is used for the time integration.

Due to the low Reynolds number, no turbulence model has been used for the simulations at $Re_D = 1500$, while large eddy simulations are performed at $Re_D = 5000$. The subgrid-scale viscosity model proposed by Vreman [67] is used to close the formulation.

3.3.2. CAA Code

The acoustic pressure is calculated as a post-process of the data obtained in the incompressible simulation. In particular, the hydrodynamic pressure on the solid walls is stored for every time step. This leads to a large amount of data which is reduced by a routine written in C language to store the data in binary format. The reduction of disk space usage achieved is 71%.

The binary files are then read by the main routine `curle_integral` which calculates the acoustic pressure given by Equation 2.13. This program is also written in C language and is prepared to be run in parallel. In addition to the binary files with the hydrodynamic pressure data, this program requires the speed of sound considered in the problem, the time interval of interest for the acoustic pressure calculation, a text file with the coordinates of the source points on the walls and a text file with the coordinates of the observers or 'listeners'.

For each observer and acoustic time, the contribution to the total acoustic pressure of each extruded plane of the CFD computational domain is computed. To account for the infinity of the wide cavity, the surface integral is extended along the spanwise direction assuming that the pressure for all the points located at $(x, y, z + nW), n \in \mathbb{Z}$, is the same as at (x, y, z). Finally, regarding the evaluation of each term of the integral

at the retarded time $\tilde{t}$, a linear temporal interpolation is used.

3.3.3. Computational Domain

Figure 3.2 shows the extension of the aerodynamic and aeroacoustic resolved domains. The dimensions of the aerodynamic domain are $32D$ in the x-direction, $8D$ in the y-direction and $3D$ for $Re_D = 1500$ and $2D$ for $Re_D = 5000$ in the z-direction. The upstream boundary is located $8D$ units ahead of the leading edge of the cavity. The dimensions of the aeroacoustic domains are $12D$ in the x-direction and $8D$ in the y-direction for the near field and $48D$ in the x-direction and $25D$ in the y-direction for the far field.

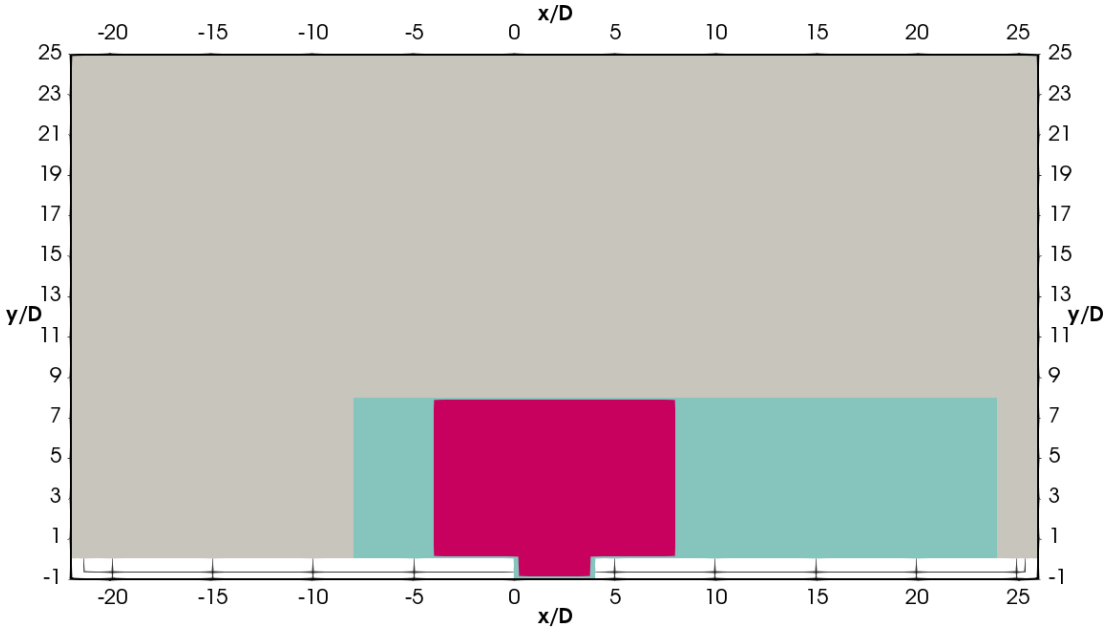

Figure 3.2: Aerodynamic (cyan), aeroacoustic in the near field (pink) and aerocoustic in the far field (grey) domains.

In order to check the appropriateness of the computational domain in the spanwise direction, spanwise two-point correlation at different locations are evaluated. The resulting autocorrelation for the velocity at a point located in the cavity, $(x/D, y/D) = (3, -0.5)$, has been represented in Figure 3.3 a-b). Its definition is:

$$R_{ii} = \frac{<u_i'(x_i,t)u_i'(x_i+\delta,t)>}{<u_i'u_i'>}, \tag{3.1}$$

where $<*>$ denotes the time average, $u_i' = u_i - \overline{u_i}$ is the velocity fluctuation and δ

is the distance in the spanwise direction. As an additional check, the autocorrelation coefficient of the pressure fluctuation for three points located on the wall at $(x/D,y/D) = (3,-1)$, $(x/D,y/D) = (4,0)$ and $(x/D,y/D) = (5,0)$ is also calculated. The results are shown in Figure 3.3 c-d).

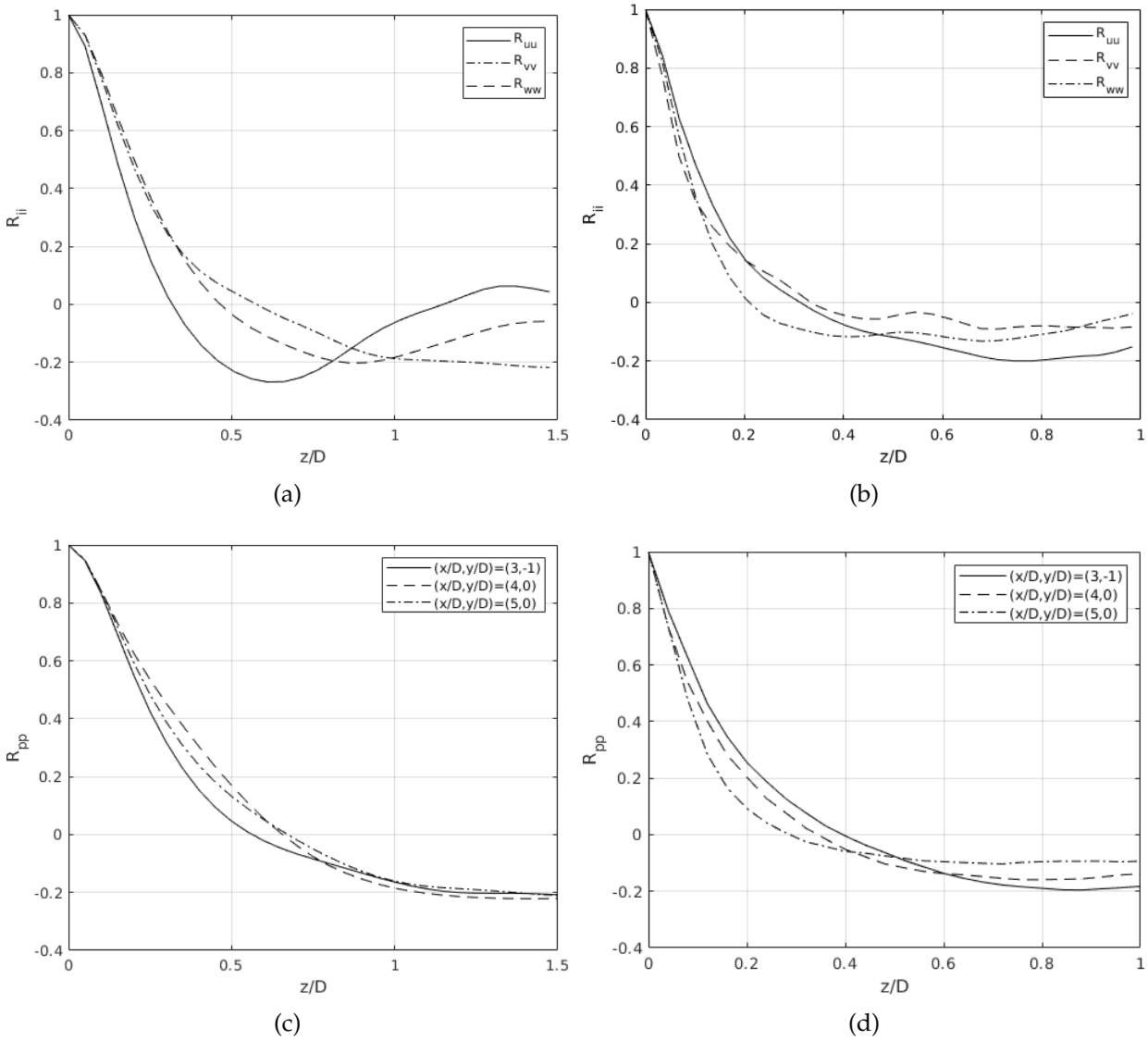

Figure 3.3: Autocorrelation coefficient along the z-axis. a-b) Velocity fluctuations for a probe located at $(x/D,y/D) = (3,-0.5)$ for $Re_D = 1500$ and $Re_D = 5000$, repectively; c-d) pressure fluctuations for probes located at $(x/D,y/D) = (3,-1)$, $(x/D,y/D) = (4,0)$ and $(x/D,y/D) = (5,0)$ for $Re_D = 1500$ and $Re_D = 5000$, repectively.

As can be seen from the figures, the autocorrelation do not completely vanish to zero at half of the spanwise size; this strictly means that the domain cannot accommodate all the largest structures. Thus, a computation with a larger spanwise size would

be required. However, given the computational resources available, a larger domain is not possible. Thus, these computations are a trade off between computational resources available and domain size. Also notice that this only affects to the largest scales; as discussed in Frohlich et al. [68] in the presence of a large range of scales it would not affect substantially the primary flow properties. Therefore, without loss of generality this assumption on the spanwise size does not affect the discussion of the results. In addition, it should be remarked that for the case 3D-SL there is a high correlation between points separated by 1 length unit, as will be appreciated in the instantaneous isocontours of Q in Section 3.4.1.

Finally, to verify that the surface of integration in Curle's integral is wide enough, different limits of integration have been compared. Figure 3.4 shows the OASPL values at $Re_D = 5000$ obtained for the observers located at distance $22D$ from the trailing edge when the surface of integration in the spanwise direction is limited between $z/D = \{\pm 10, \pm 20, \pm 30, \pm 40, \pm 50, \pm 60, \pm 70\}$. As it can be seen, the differences are negligible beyond ± 50. Thus, the surface of integration has been limited in the spanwise direction from $z/D = -50$ to $z/D = 50$ and in the streamwise direction from $x = -6D$ to $x = 23D$. The calculation of the integral is made every $\Delta t = 0.1TU$ for a total time range $T = 100TU$. Detailed maps of the acoustic field in a grid around the cavity at plane $z/D = 0$ have been obtained.

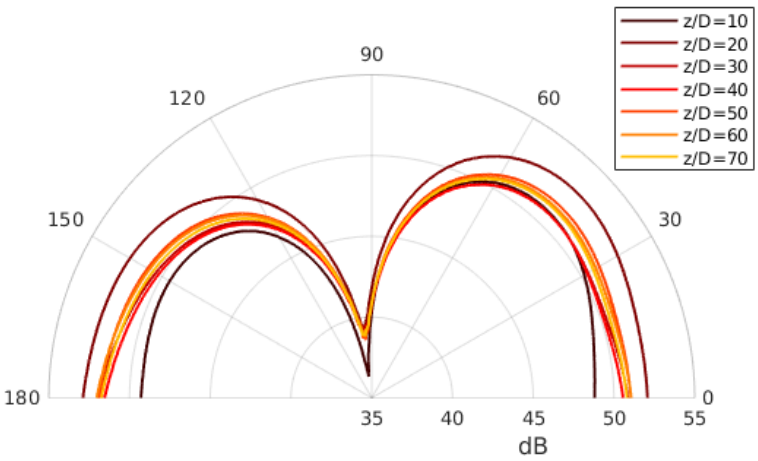

Figure 3.4: OASPL directivity for $Re_D = 5000$ with different integration regions with z/D limits: $\{\pm 10, \pm 20, \pm 30, \pm 40, \pm 50, \pm 60, \pm 70\}$.

3.3.4. Computational Grid

Non-structured grids have been used for the $x-y$ planes. Special care has been taken to well resolve the boundary layer around the cavity, the area where the wall pressure is significantly contributing to the acoustic signal. The nodes are clustered near the walls, within the cavity and in the wake region (see Figure 3.5). The three-dimensional mesh has been created by extruding a two-dimensional mesh.

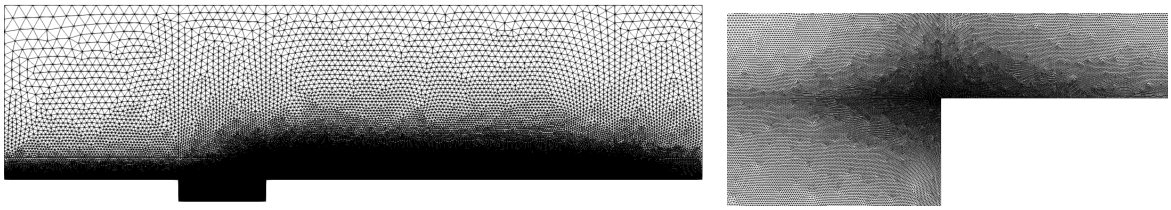

(a) (b)

Figure 3.5: Elements distribution in the $x-y$ plane. a) Complete aerodynamic domain; b) zoom in the leading edge of the cavity.

Mesh	Nodes ($\times 10^6$)	$\Delta y_n / D_{s^*=6D}$	$\Delta z / D$	W / D
Mesh 1 1500	3.9	0.0040	0.05	3
Mesh 2 1500	4.9	0.0035	0.05	3
Mesh 3 1500	14.8	0.0025	0.05	3
Mesh 1 5000	4.9	0.0035	0.05	3
Mesh 2 5000	14.8	0.0025	0.05	3
Mesh 3 5000	8.2	0.0025	0.05	2
Mesh 4 5000	18.8	0.0020	0.04	2
Mesh 5 5000	39.6	0.0015	0.04	2

Table 3.3: Meshes used in the present work for $Re_D = 1500$ and $Re_D = 5000$.

A grid convergence study has been carried out in order to ensure the accuracy of the acoustic results. The mesh parameters used are presented in Table 3.3. Figure 3.6 shows the time averaged drag coefficient C_D and the main Strouhal number St_L obtained for the meshes considered. Despite the large increase in mesh resolution between the two finest meshes for both Reynolds numbers, the results are within 4% difference. Moreover, to confirm that the pressure distribution along the wall is converged, its time-averaged value, $<p>$, has been represented in Figure 3.7 for the two finest meshes. Notice that to have statistically representative average variables,

the operator <∗> is defined as the average not only in time but also in the spanwise direction. The discontinuous vertical lines define the corners of the cavity. As can be seen, the distributions are very close ensuring enough accuracy in the sound level prediction.

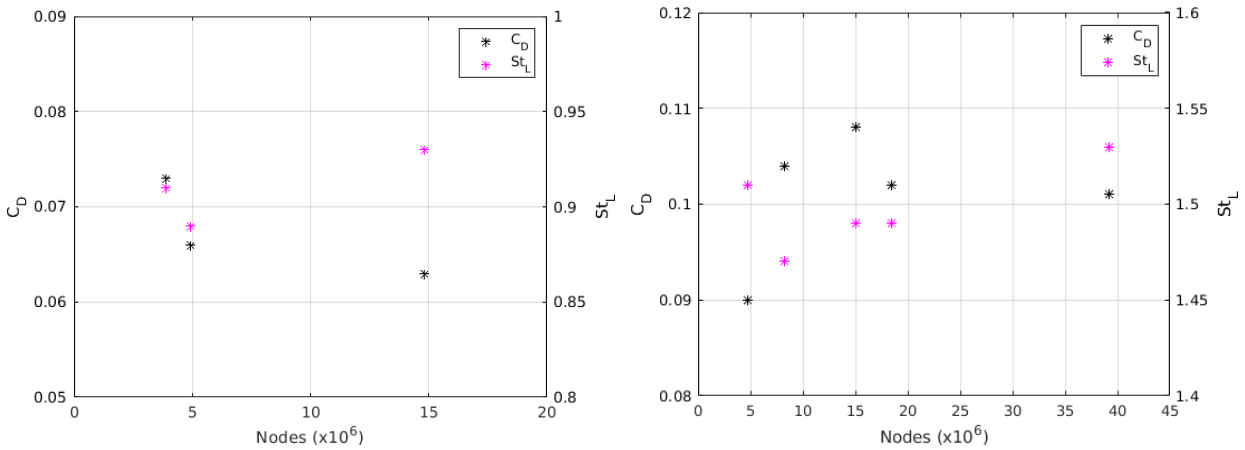

Figure 3.6: Time averaged C_D and main St_L convergence. a) $Re_D = 1500$; b) $Re_D = 5000$.

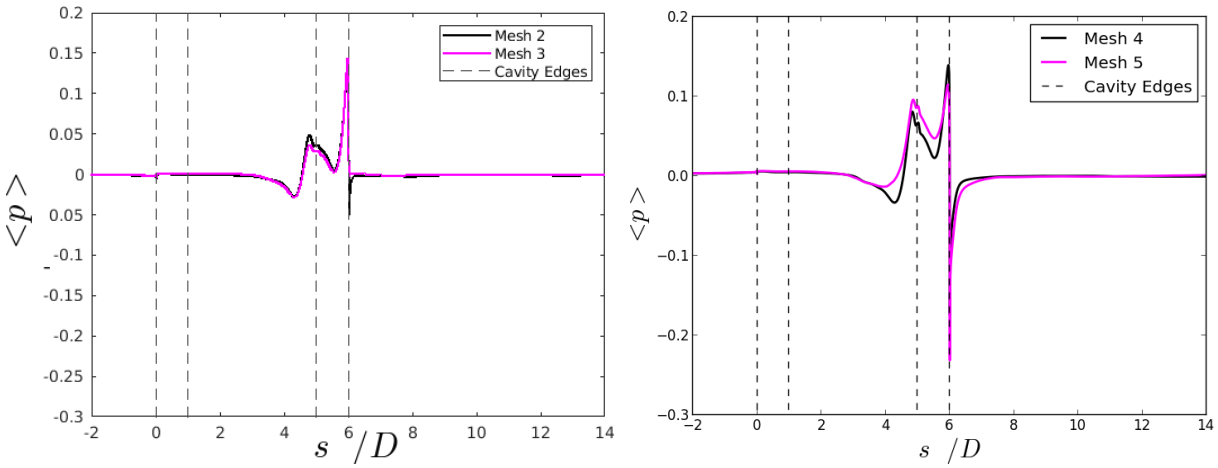

Figure 3.7: <p> value along the wall. The discontinuous vertical lines correspond to the edges of the cavity. a) $Re_D = 1500$; b) $Re_D = 5000$.

The dimensionless wall-normal distance, y^+, the streamwise wall spacing, Δx^+, and the spanwise wall spacing, Δz^+, obtained from the statistical post-processing of the results as a function of s are shown in Figure 3.8. The fluctuations appearing

at laminar locations (s/D<0) for y^+ are not considered relevant since the boundary layer is not turbulent yet. In addition, as it will further be seen, this region is not of particular interest since the wall pressure fluctuations are not relevant. In the area of main interest for acoustic generation, y^+<1.5, Δx^+<2.5 and Δz^+<30. As discussed by Piomelli and Chasnov in [69] the grid requirements to represent accurately the near-wall structures for a LES simulation are y^+<2, Δx^+<150 and Δz^+<40. Therefore, the values obtained for the finest meshes of each case are considered suitable for this study.

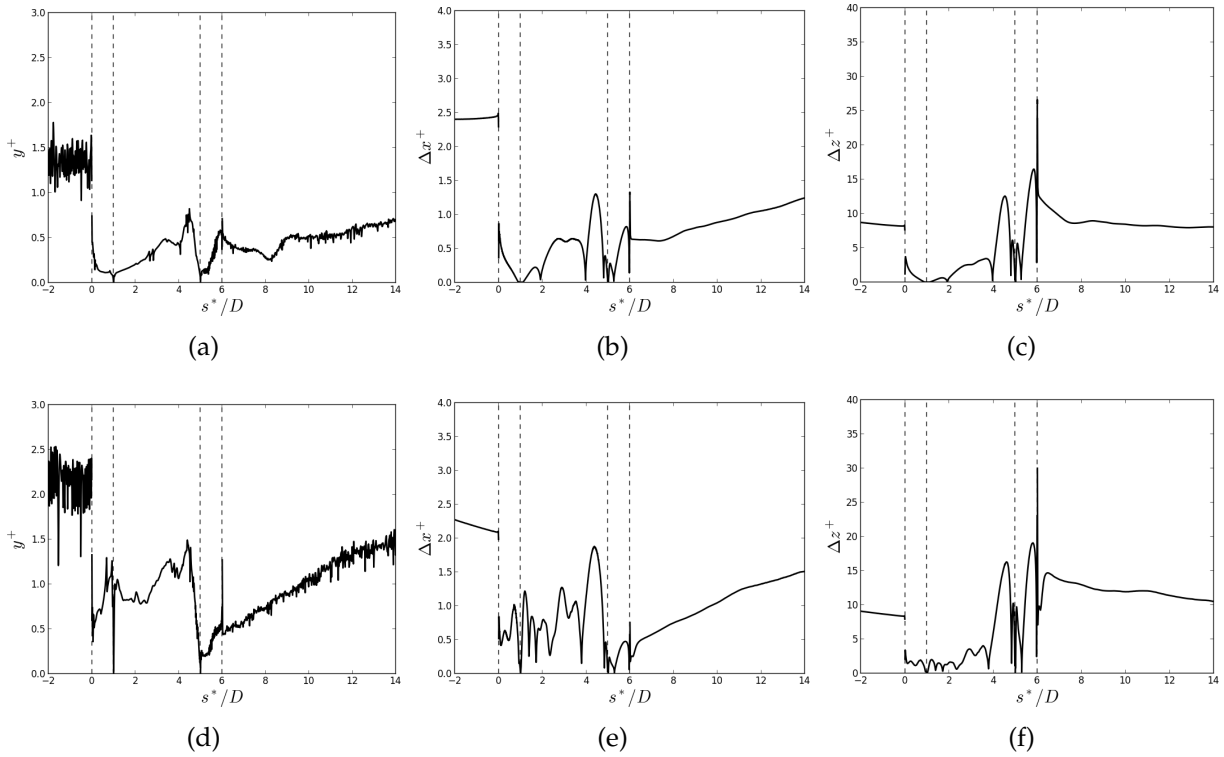

Figure 3.8: Near wall grid resolution. The discontinuous vertical lines correspond to the edges of the cavity. a-c) y^+, Δx^+ and Δz^+ for $Re_D = 1500$; d-f) y^+, Δx^+ and Δz^+ for $Re_D = 5000$.

Finally, Figure 3.9 shows the acoustic directivity for the observers located at distance $22D$ from the trailing edge obtained with the two finest meshes. On average, the difference in OASPL is $2.9dB$ for $Re_D = 1500$ and $0.6dB$ for $Re_D = 5000$ at certain locations although the overall agreement between the results is considered satisfactory.

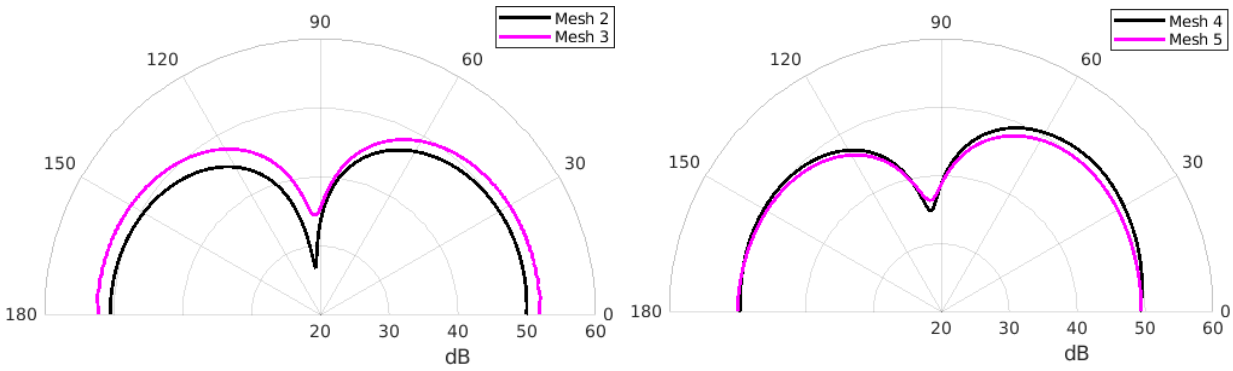

(a) (b)

Figure 3.9: OASPL directivity. a) $Re_D = 1500$; b) $Re_D = 5000$.

3.4. Results

3.4.1. Flow Field Results

Dimensional Behaviour of the Flow, $Re_D = 1500$.

In this section, the flow field results obtained for $Re_D = 1500$ are discussed. Figure 3.10 shows the instantaneous flow structures by means of $\mathcal{Q}$-isosurfaces ($\mathcal{Q} = 0.1$) coloured by non-dimensional pressure for a time corresponding to a drag peak. As expected from [35], for Reynolds numbers above 1200 the flow shows developed three-dimensional structures. The high velocity near the wall at the leading edge of the cavity makes the vortex shed from the leading edge sufficiently energetic to enhance the vorticity and eventually breaking up into smaller vortices before impinging the trailing edge. After this collision, the fluid is redirected to two different locations. A closer look to the frontal view of Figure 3.10 reveals that part of the fluid is pulled down to the right bottom corner of the cavity, while the rest of the fluid is expelled to the downstream wall, developing a boundary layer with complex structures such as quasi-streamwise and hairpin vortices.

Figure 3.11 shows the mean streamlines obtained by spanwise-averaging and time-averaging of the velocity field inside the cavity. From Figure 3.11 it is seen that the part of the fluid entering inside the cavity follows a recirculatory motion which nearly occupies the right third of the cavity.

The evolution of the time averaged pressure $<p>$ along s is shown in Figure 3.12. The pressure is null up to $s \approx 3.7$, just before the bottom right corner of the cavity. Then, two peaks located at $s \approx 4.8$ and $s \approx 6$ appear as a consequence of the two different flow dynamics phenomena previously described. The first peak corresponds

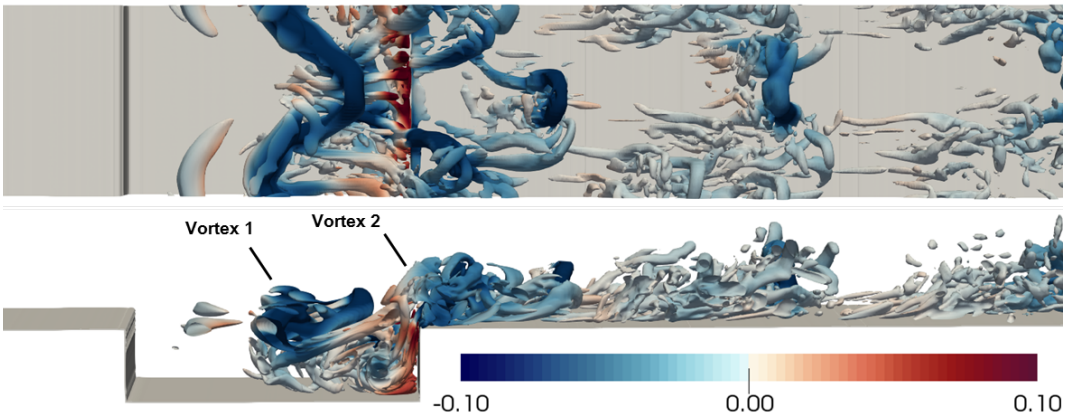

Figure 3.10: Isosurface of $\mathcal{Q} = 0.1$ coloured by pressure for $Re_D = 1500$. Zero pressure corresponds to the pressure in the non-disturbed part of the domain. Top: zenital view. Bottom: frontal view.

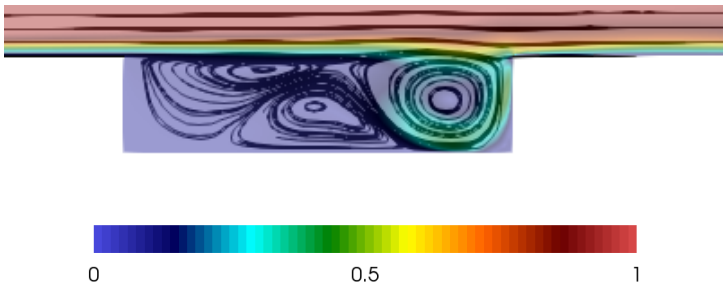

Figure 3.11: Mean streamlines coloured by velocity at $Re_D = 1500$.

to the primary recirculation confined in the bottom of the cavity. The second peak is associated to to the impingement of the shear layer on the trailing edge. Immediately after the trailing edge position, the pressure experiences a large gradient, abruptly decreasing from <p> = 0.12 to <p>=-0.06. This singularity is due to the violent ejection of the shedding vortices impinging the trailing edge to the downstream wall.

As discussed in the Introduction (Section 3.1), many works have considered this problem using a two-dimensional simulation model to describe the flow. If a two-dimensional model is assumed, the results are very different and the fluid dynamics matches the description given in [23, 39]. The vortex detached from the leading edge of the cavity starts to pull fluid from the cavity generating a new growing vortex at the bottom left corner, which moves downstream until the trailing edge, where it is forced out by the one generated at the next period. Then, the vortical structures formed in the cavity edge travel downstream almost unaltered and attached to the wall of the domain as can be seen in the instantaneous pressure map of Figure 3.13 b). Figure 3.14 a) compares <p> for 2D-WM and 3D-WM. For 2D-WM the mean pressure distribution is completely different. The pressure rises steeply until the end of the

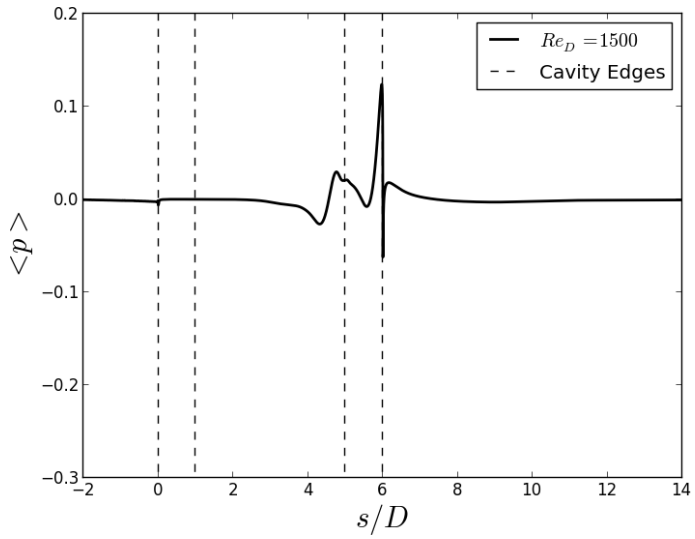

Figure 3.12: Spanwise and time averaged pressure <p> along the wall for $Re_D = 1500$.

cavity, reaching a maximum in the bottom right corner of <p> = 0.25, followed by a minimum value at the trailing edge of <p> = -0.20. As a consequence, wall pressure dependant variables as the drag coefficient or the acoustic pressure are artificially much higher. The differences in the acoustic results will be seen in Section 3.4.2, as for the drag coefficient, $C_D = 0.403$ for 2D-WM (in agreement with other works addressing the problem with the same numerical approach [21, 23]) while $C_D = 0.066$ for 3D-WM.

Oscillation Mode, $Re_D = 1500$

As aforementioned, Colonius et al. [38], described two different oscillation modes for the cavity. In order to determine if the oscillations of the SL mode are sustained without the acoustic feedback mechanism, absent in the incompressible Navier-Stokes equations, a simulation of the cavity in SL mode has been studied. Figure 3.13 a) displays the instantaneous pressure map for 3D-SL and Figure 3.13 c) for 3D-WM. It can be seen that the results between SL and WM oscillation modes are significantly different: for the SL mode there is a weak recirculation at the right bottom corner of the cavity with a much lower maximum on the trailing edge, <p>=0.05, generated by the impingement of the vortex created in the shear layer. This mode is very similar in two-dimensional and three-dimensional simulations as only a very small three-dimensional structure of one length unit appears inside the cavity as can be seen in Figure 3.15.

The drag evolution has also been represented in Figure 3.16. The drag force is very weak in SL, as expected from the small pressure values already shown in Figure

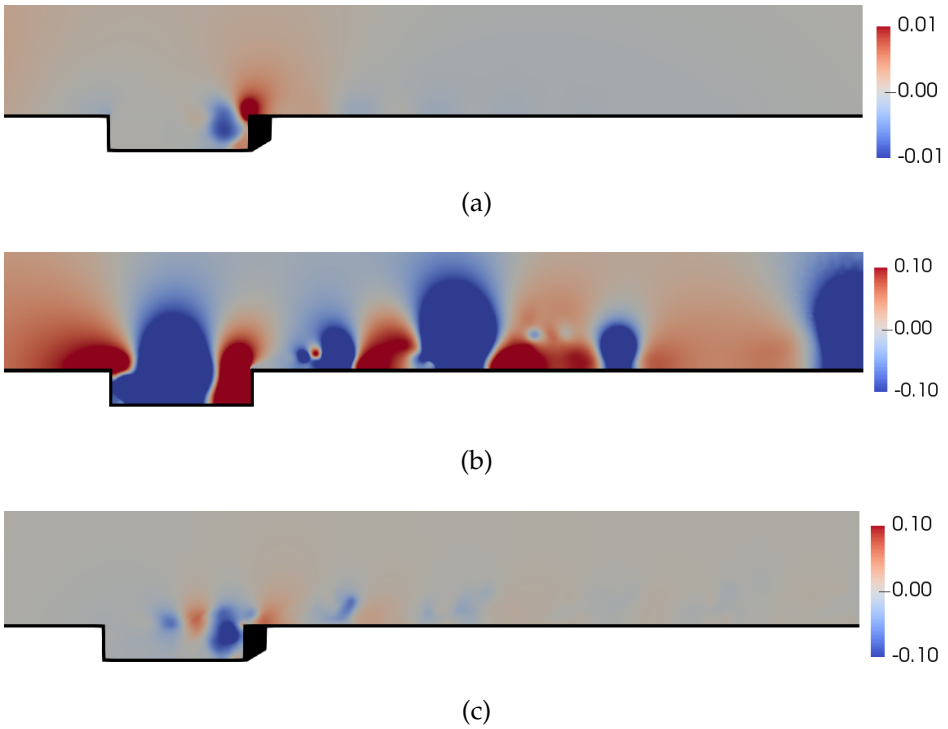

Figure 3.13: Instantaneous pressure map. Zero pressure corresponds to the pressure in the non-disturbed part of the domain. a) 3D-SL; b) 2D-WM; c) 3D-WM.

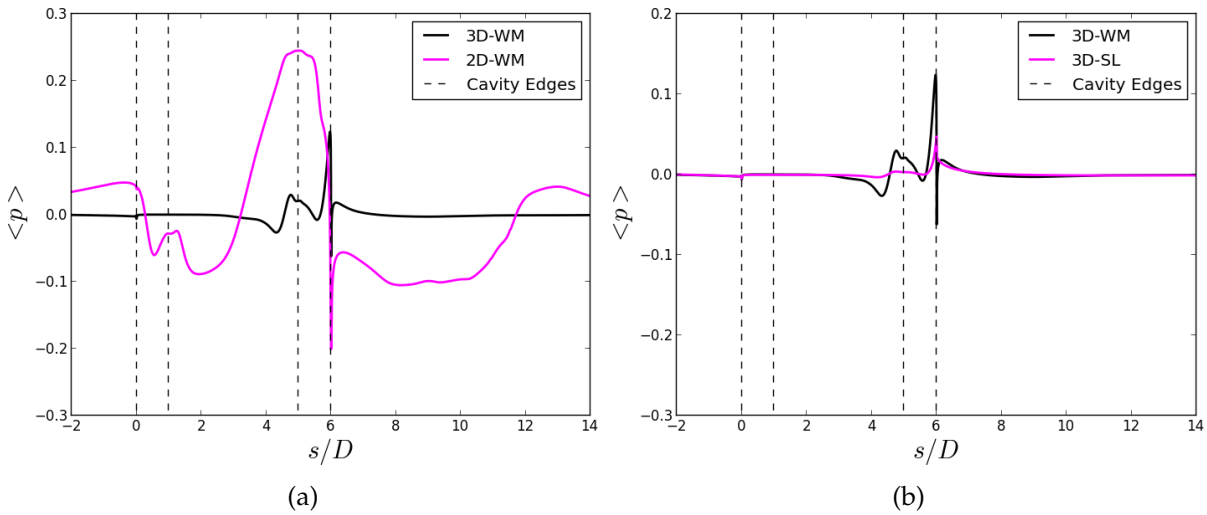

Figure 3.14: Spanwise and time averaged pressure <p> along the wall for $Re_D = 1500$. a) 2D-WM and 3D-WM; b) 3D-SL and 3D-WM.

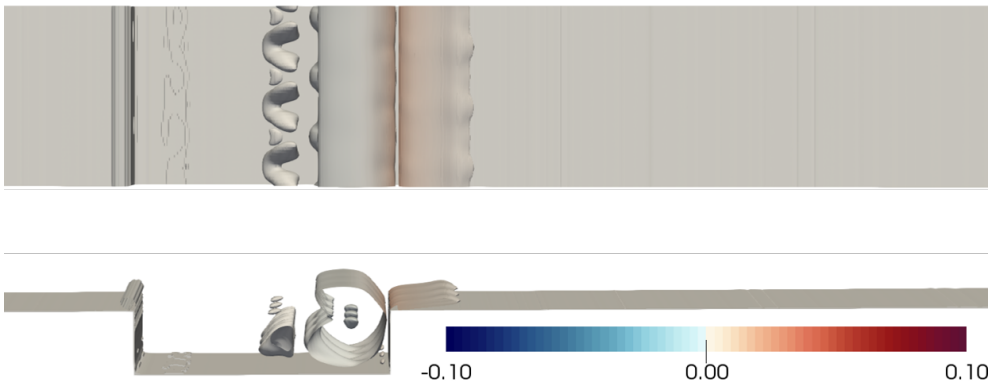

Figure 3.15: Isosurface of $\mathcal{Q} = 0.1$ coloured by pressure for $Re_D = 1500$ and SL mode. Zero pressure corresponds to the pressure in the non-disturbed part of the domain. Top: zenital view. Bottom: frontal view.

3.14 b). Although a precise determination of the transition point between SL and WM is out of the scope of this thesis, runs where the boundary layer is developed during 10D ($L/\theta = 76$), 11D ($L/\theta = 74$) and 12D ($L/\theta = 72$) before the leading edge of the cavity have been compared in Figure 3.16 b). In the Figure, the cases are referred as 3D-SL-10, 3D-SL-11 and 3D-SL-12, respectively. The results obtained in 3D-SL-11 and 3D-SL-12 exhibit the decay of the oscillations while 3D-SL-10, which roughly corresponds to the transition between SL and WM, does not. On the other hand, results obtained with a compressible model show self-sustained oscillations for these parameters, confirming the importance of the acoustic waves in the SL mode and not in the WM.

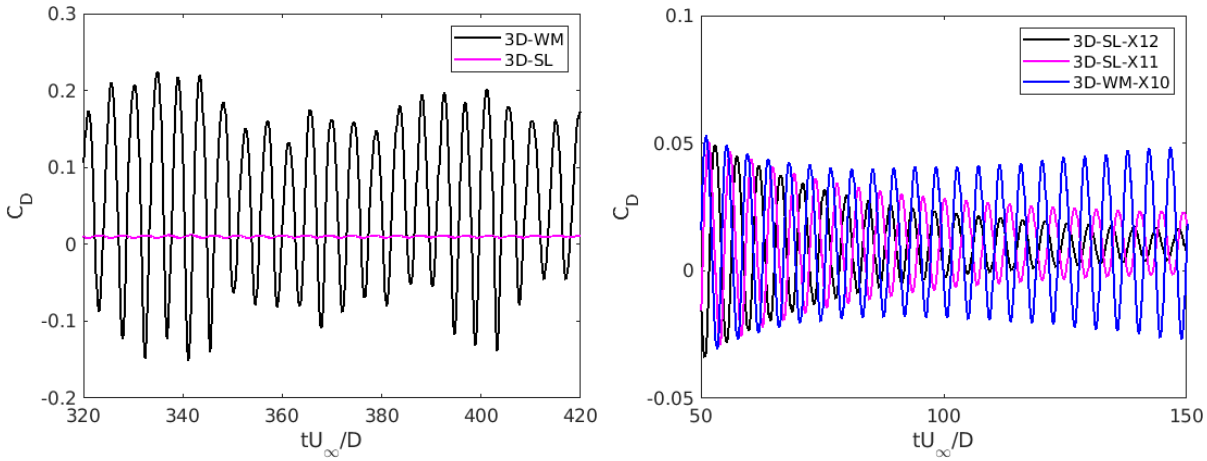

(a) (b)

Figure 3.16: C_D time evolution. a) 3D-SL and 3D-WM; b) 3D-SL-12, 3D-SL-11 and 3D-WM-10.

Reynolds Number Influence, $Re_D = 1500$ and $Re_D = 5000$

In this section, the flow field results obtained for $Re_D = 5000$ are discussed and compared with the previously shown for $Re_D = 1500$. Figure 3.17 shows the instantaneous flow structures by means of $\mathcal{Q}$-isosurfaces. For $Re_D = 5000$ the vortical structures represented are smaller and more abundant than at $Re_D = 1500$. At $Re_D = 5000$ the large spanwise vortex that has rolled up in the leading edge breaks into smaller scale vortices farther upstream than at $Re_D = 1500$ and the ejection of the fluid to the downstream wall is more violent. In addition, while two shedding vortices lie inside the shear layer for $Re_D = 1500$, at $Re_D = 5000$ three vortices are recognised. As a consequence, the higher frequency of vortex detachment from the leading edge changes the dominant St_L, as will be seen below.

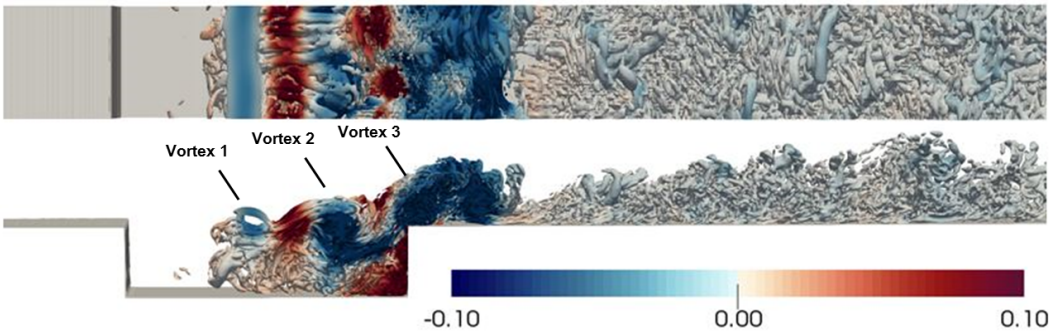

Figure 3.17: Isosurface of $\mathcal{Q} = 0.1$ coloured by pressure for $Re_D = 5000$. Zero pressure corresponds to the pressure in the non-disturbed part of the domain. Top: zenital view. Bottom: frontal view.

Figure 3.18 shows the mean streamlines. In this case the part of the fluid entering inside the cavity follows a larger and faster recirculatory motion with respect to $Re_D = 1500$ which nearly occupies the right half of the cavity.

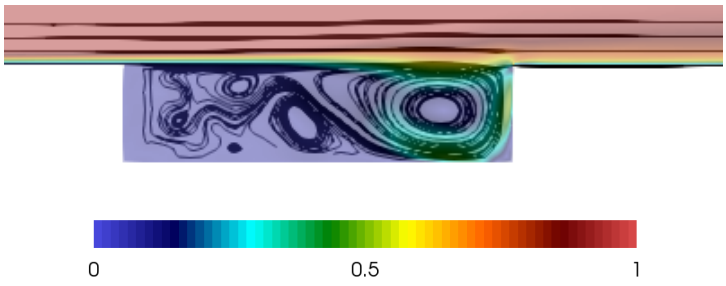

Figure 3.18: Mean streamlines coloured by velocity at $Re_D = 5000$.

Figure 3.19 shows the instantaneous pressure distributions at the same instant as in Figures 3.10 and 3.17 for $Re_D = 1500$ and $Re_D = 5000$, respectively. While at $Re_D = 5000$ the instantaneous flow footprint on the downstream wall is weaker than

at $Re_D = 1500$, in the right and bottom wall of the cavity it is higher. This is more clearly appreciated in Figure 3.20 which shows <p> along s for both cases. The evolution of <p> between both Reynolds numbers follow a similar shape, except around two regions: the right bottom corner of the cavity and after the trailing edge. Due to the more intense recirculation inside the cavity at $Re_D = 5000$, the first peak of pressure is four times higher than at $Re_D = 1500$. As a consequence, the drag coefficient increases from $C_D = 0.063$ to $C_D = 0.101$. The different behaviour after the trailing edge position is associated to the more abrupt ejection of the flow to the downstream wall and subsequent reattachment which generates a region of negative wall pressure along the detachment area for $Re_D = 5000$. This fact is confirmed in Figure 3.21, which shows the shape factor along the downstream wall. For $Re_D = 5000$, the evolution of the shape factor shows a peak, typical of a reattachment flow motion. It should also be remarked that while for $Re_D = 5000$ a turbulent boundary layer is developed (the theoretical shape factor of such is reached), for $Re_D = 1500$ the shape factor tends to $H = 1.8$.

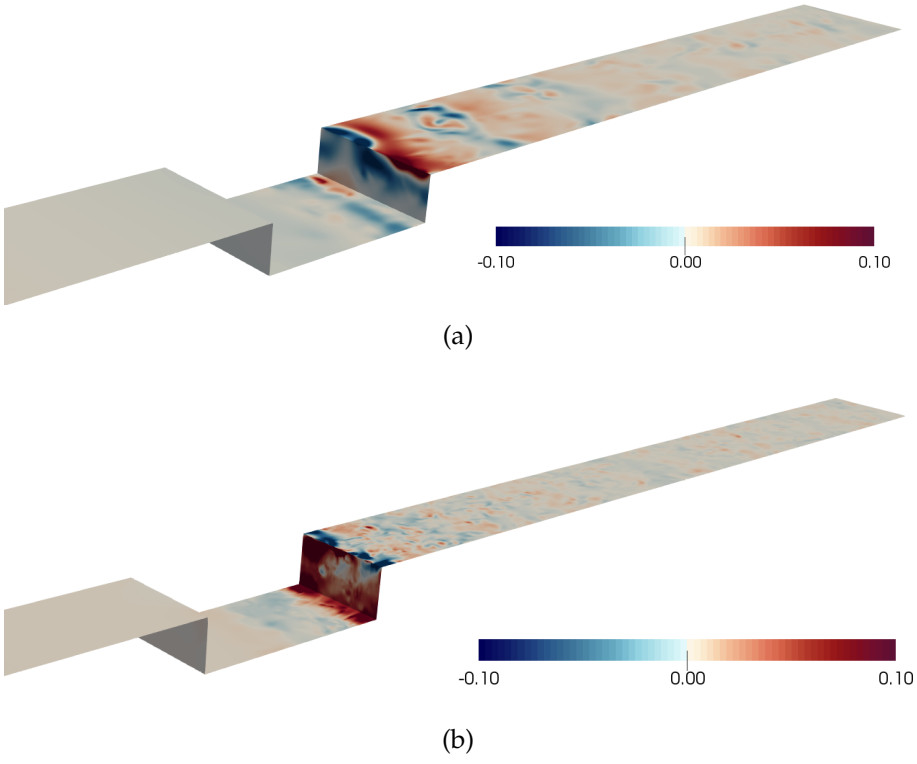

Figure 3.19: Instantaneous pressure map. Zero pressure corresponds to the pressure in the non-disturbed part of the domain. a) $Re_D = 1500$; b) $Re_D = 5000$.

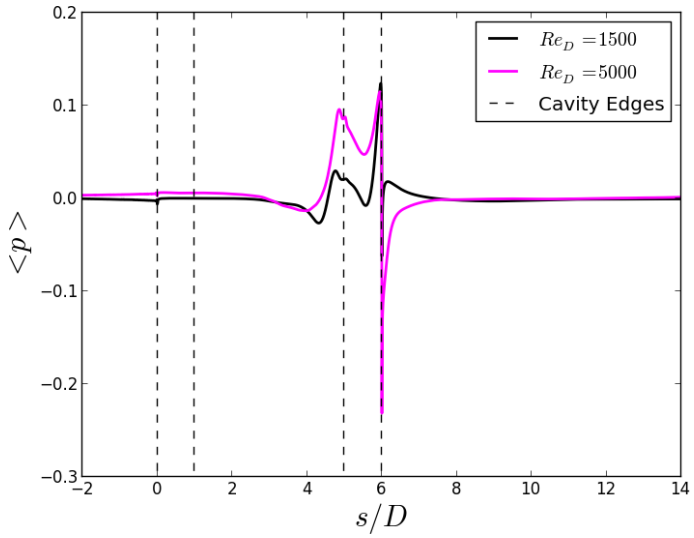

Figure 3.20: Spanwise and time averaged pressure <p> along the wall for $Re_D = 1500$ and $Re_D = 5000$.

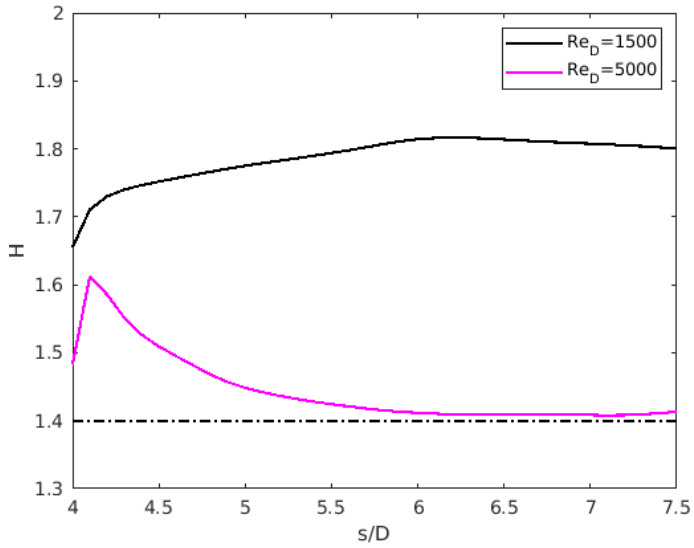

Figure 3.21: Shape factor along the downstream wall for $Re_D = 1500$ and $Re_D = 5000$. The theoretical value for a turbulent boundary layer is 1.4 [1].

Passive Noise Control Techniques, $Re_D = 5000$

An investigation on passive noise control techniques have also been carried out along this thesis for $Re_D = 5000$. In this section, the influence of each of the modifications proposed for the parameters L, R_1, R_2, R_3 and h is analysed and compared with the results of the baseline case, which hereafter will be referred as C1. The aim is to investigate the underlying mechanism of passive flow control and its connection with acoustics, which will be presented in Section 3.4.2.

Figure 3.22 shows the instantaneous flow structures by means of Q-isosurfaces for cavities C1 to C8. When the trailing edge is rounded, the shedding vortices arriving to the trailing edge slide from the rear wall of the cavity to the downstream wall and the development of the turbulent boundary layer starts before than for C1. This fact is confirmed in Figure 3.23 which shows the boundary layer shape factor H along the downstream wall. For the sake of a clearer representation, the variable s has been shifted in such a way that the trailing edge of each configuration is located at the position of the trailing edge for the baseline case, $s/D = 6$. Hereafter, this new variable is denoted as s^* and is defined as $s^* = s + (6 - s_{Ci}^{TE})$, where s_{Ci}^{TE} stands for the original position of the trailing edge for each configuration C_i, $i = 1...8$. In the Figure, the theoretical value for a turbulent boundary layer is progressively reached as the boundary layer develops for all the cavities, but the shape factor for C4 and C5 does not show the peak present at the trailing edge for C1. As a consequence, the fluid moves forward more smoothly than in the baseline case, avoiding the violent ejection from the cavity and the singularity in pressure produced at the trailing edge.

Regarding the height of the cavity, Figure 3.22 g) shows that for C7 the shear layer avoids the collision with the trailing edge and is directed to the exit wall, generating a high overload on this surface. On the contrary, the shear layer of C8 fully impacts the rear wall of the cavity and intensifies the ejection of the fluid to the downstream wall, agreeing with the results of Figure 3.23 b), where the magnitude of the peak of the shape factor for C8 is nearly four times higher than for C1. For C7, the evolution of H shows a monotonous decreasing behaviour from $s^*/D = 6$ since the boundary layer does not experience a detachment and subsequent reattachment to the wall.

Figure 3.24 shows the mean streamlines for all the cavities. The recirculation in the right half of the cavity increases its size for cavities C2, C4, C5 and C6, nearly filling the whole gap and reducing its velocity magnitude near the wall, which, as it will be seen below, generates a less intense pressure on its walls. The results of Hao et al. [58] showed that when the incoming boundary layer is turbulent the recirculation inside

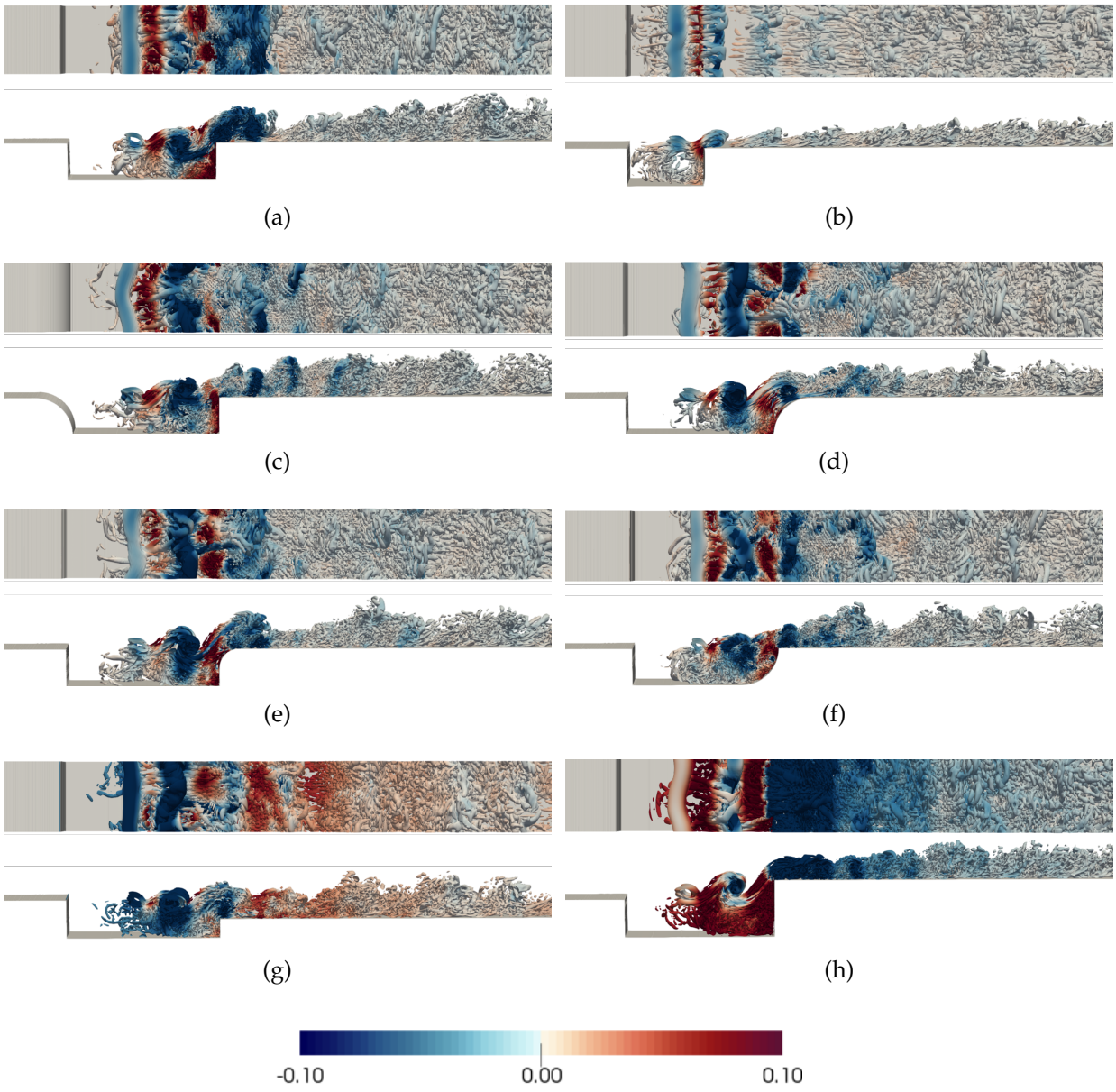

Figure 3.22: Isosurface of $\mathcal{Q} = 0.1$ coloured by non-dimensional pressure. Top: zenital view. Bottom: frontal view. a) C1; b) C2; c) C3; d) C4; e) C5; f) C6; g) C7; f) C8.

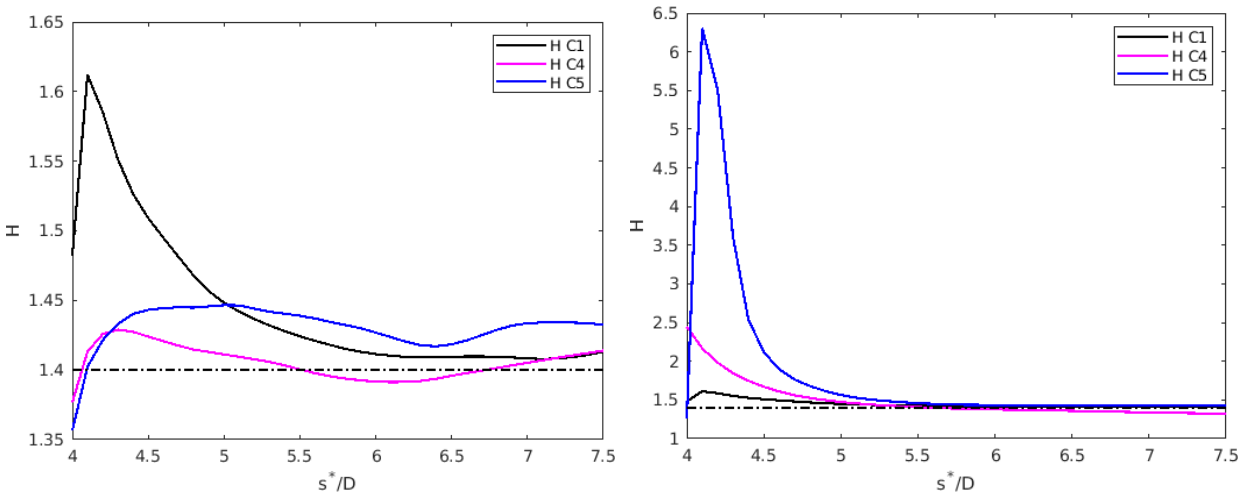

Figure 3.23: Shape factor along the downstream wall. The theoretical value for a turbulent boundary layer is 1.4 [1]. a) C1, C4 and C5; b) C1, C7 and C8.

the cavity already fills the whole gap for the baseline geometry and the effect of the trailing edge height was only noticeable when the cavity was long enough, $L/D = 8$. The results of the time averaged pressure for the rest of the cavities reveal that the modification of the length of the cavity, cavity C2, and the bottom right corner, cavity C6, significantly reduce the first peak of pressure. Despite none of the variations reduce the magnitude of the second peak of pressure, there is a relevant change in the pressure gradient after the trailing edge for cavities C2, C4, C5 and C7 (see Figure 3.25 a), c) and e)) due to a smoother interaction of the shear layer with the trailing edge. On the contrary, the results of $<p>$ for cavity C8 show a drastic increase of the pressure over the rear wall of the cavity which magnifies the abrupt decrease of pressure at the trailing edge.

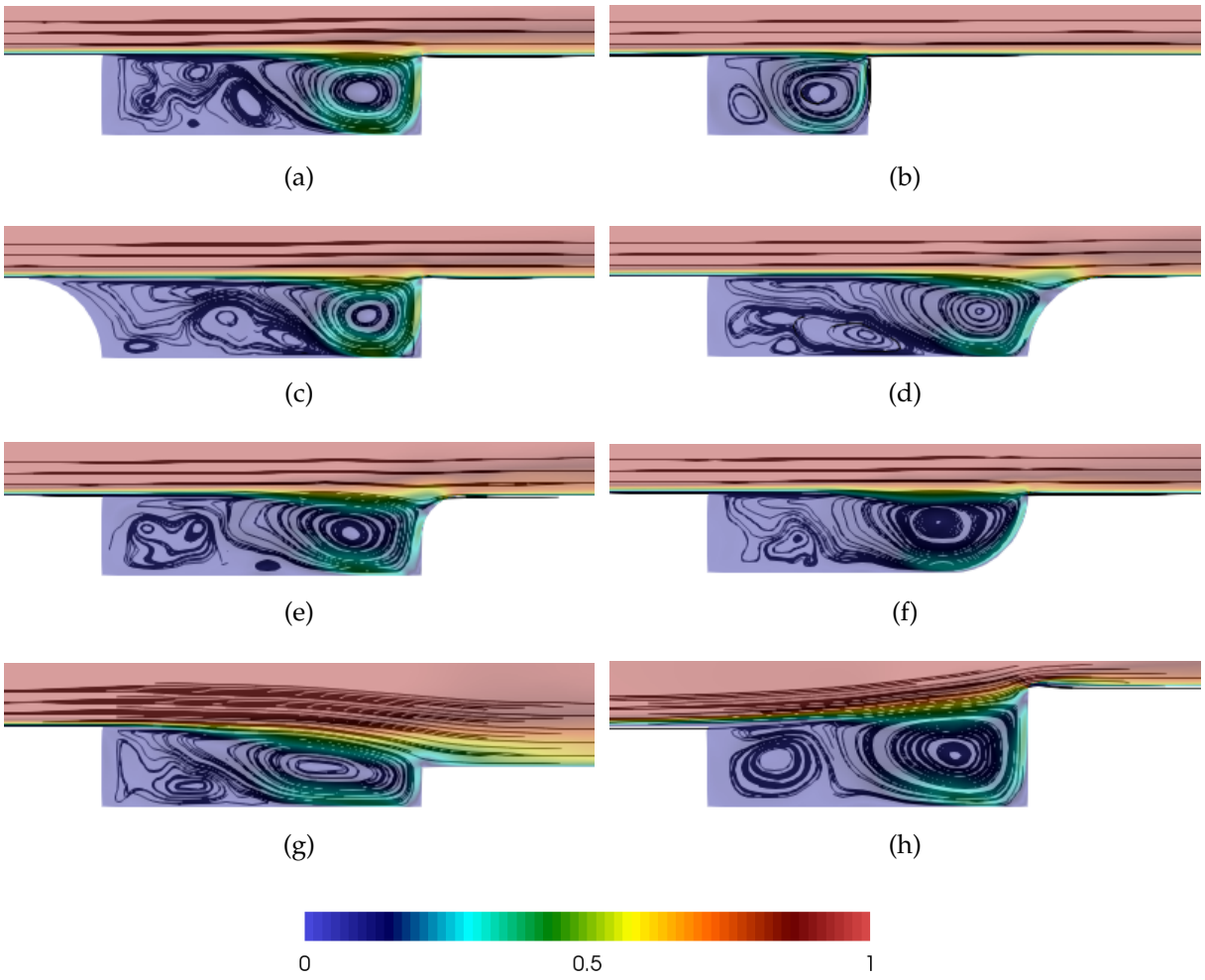

Figure 3.24: Mean streamlines for cavities C1 to C8 coloured by velocity. a) C1; b) C2; c) C3; d) C4; e) C5; f) C6; g) C7; f) C8.

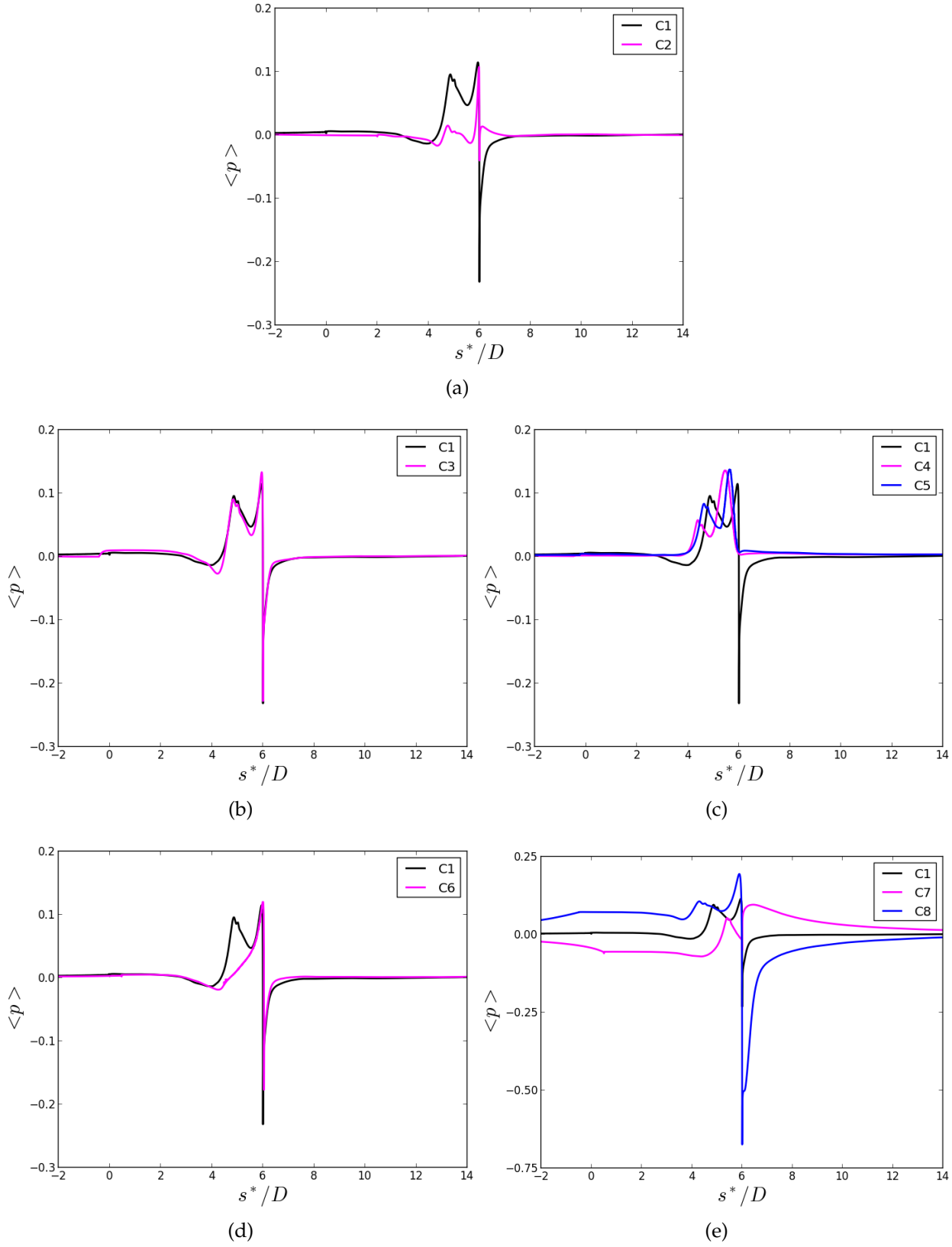

Figure 3.25: Spanwise and time averaged pressure <p> along the wall. Comparison with the baseline cavity C1. a) C1 and C2; b) C1 and C3; c) C1, C4 and C5; d) C1 and C6; e) C1, C7 and C8.

3.4.2. Acoustic Field Results

Dimensional Behaviour of the Flow, $Re_D = 1500$

In this section, the acoustic results obtained for $Re_D = 1500$ are discussed and the suitability of Curle's analogy for noise prediction is analysed. Figure 3.26 shows the OASPL distribution on the far field map defined in Figure 3.2. The acoustic intensity distribution shows two different lobes (typical of a dipole source) arising from the trailing edge of the cavity, where the OASPL reaches values around 65dB. As the observer moves further away from the trailing edge, both lobes progressively decrease their intensity but with different gradients. The directivity pattern displayed in Figure 3.27 for the observers located at $22D$ from the trailing edge shows that the two main directions of radiation are 30° (downwards positions) and 150° (upwards positions), while the minimum direction is around 100° (above the trailing edge). The described dipole behaviour is in good agreement with the far field experimental results of Koschatzky et al. [70] for an open cavity with aspect ratio $L/D = 2$ and $Re_D = 1.5 \times 10^4$ at $M = 0.05$ combining Curle's analogy with flow field results obtained from PIV measurements.

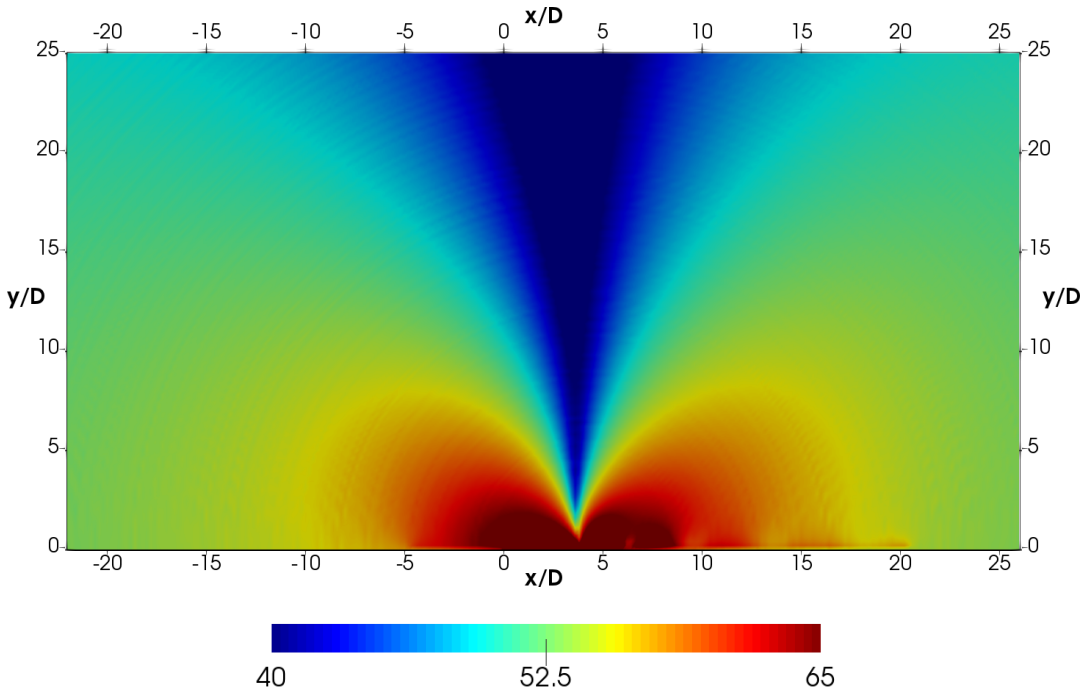

Figure 3.26: OASPL in the far field for $Re_D = 1500$.

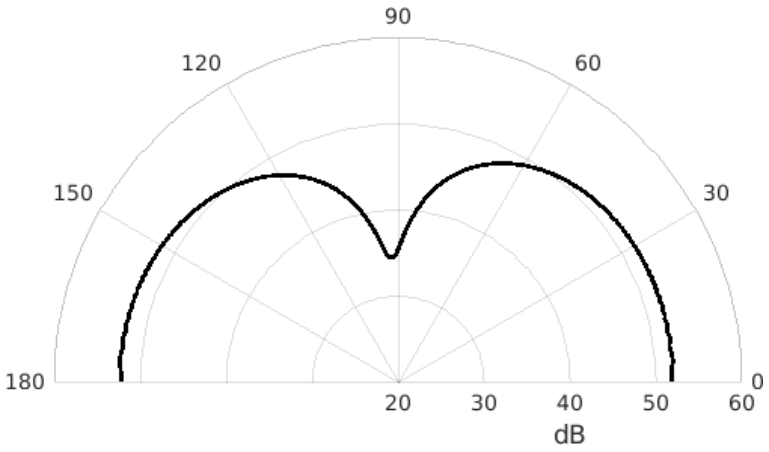

Figure 3.27: OASPL directivity for $Re_D = 1500$. The observers are located at distance $22D$ from trailing edge of the cavity.

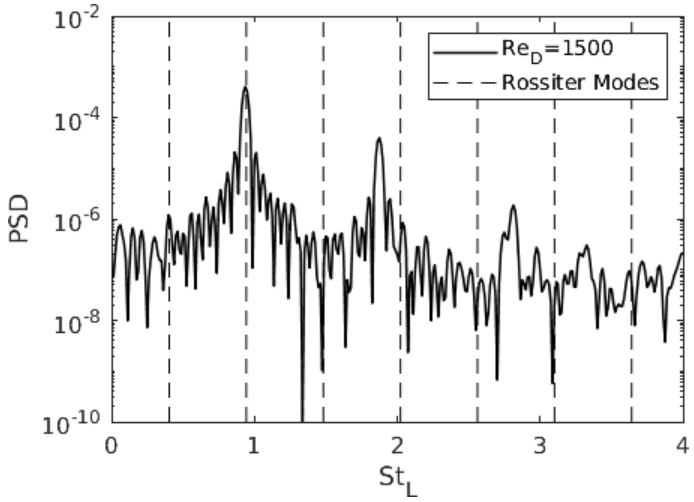

Figure 3.28: Frequency spectrum of the observer located at $(x/D, y/D, z/D) = (-3, 5.5, 0)$ for $Re_D = 1500$.

Acoustic pressure fluctuations for cavity flows have been experimentally shown to oscillate at certain frequencies known as Rossiter modes [71]. The empirical formula to predict the n-th Rossiter mode is:

$$St_L = \frac{n - \gamma}{\left(\frac{1}{\kappa} + M\right)}, \tag{3.2}$$

where the phase delay is $\gamma = 0.25$ and the average convective speed of disturbance in the shear layer is $\kappa = 0.57$. Using Equation 3.2, the predicted second and third frequency stage for $M = 0.1$ are $St_L = 0.9$ and $St_L = 1.5$. The frequency spectrum for an observer located in the far field is shown in Figure 3.28. The PSD values have been calculated using the Lomb-Scargle algorithm [72, 73]. As can be seen, the dominant

St_L coincides with the second stage of Rossiter. So far, it is important to verify that these results satisfy the Hemholtz criteria (Equation 2.14), so scattering phenomena such as reflections are not affecting Curle's analogy results. In this case, the Hemholtz number is $He = 0.1$, hence below 1.

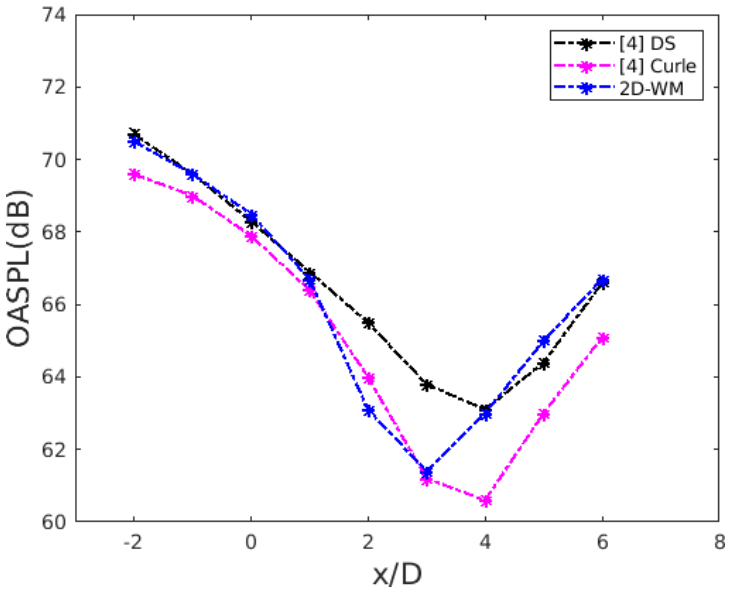

Figure 3.29: $OASPL$ for observers located at $y/D = 7.18$ and $x/D \in \{-2,-1,0,1,2,3,4,5,6\}$ for 2D-WM and reference [2].

As aforementioned, many studies have been devoted to this configuration considering a two-dimensional flow solution to describe the physics of the problem [2, 21, 22]. Under the same assumption, the present results have been compared with the literature for $M = 0.15$. The results shown in Figure 3.29 display the OASPL obtained by Davidson and Ask in [2] for the wake mode of the cavity when $L/\theta \approx 95$ at the leading edge. The results are considered to be in good agreement with theirs and the differences are attributed either to a different boundary layer development at the inlet of the cavity (in the present results $L/\theta \approx 79$) or to a different integration region for the Curle integral.

Nevertheless, as it was seen in Section 3.4.1, the flow field results considering a three-dimensional model were significantly different than those obtained with a two-dimensional simulation and, as a consequence, so should be the acoustic results. Indeed, Figure 3.30-b) shows the OASPL for the map described by the observers in the near field of Figure 3.2 for 2D-WM and Figure 3.30-c) for 3D-WM (in both cases the Mach number considered is $M = 0.15$). Although the dipolic behaviour is appreciated in both 2D-WM and 3D-WM, the results for 2D-WM have a signal level

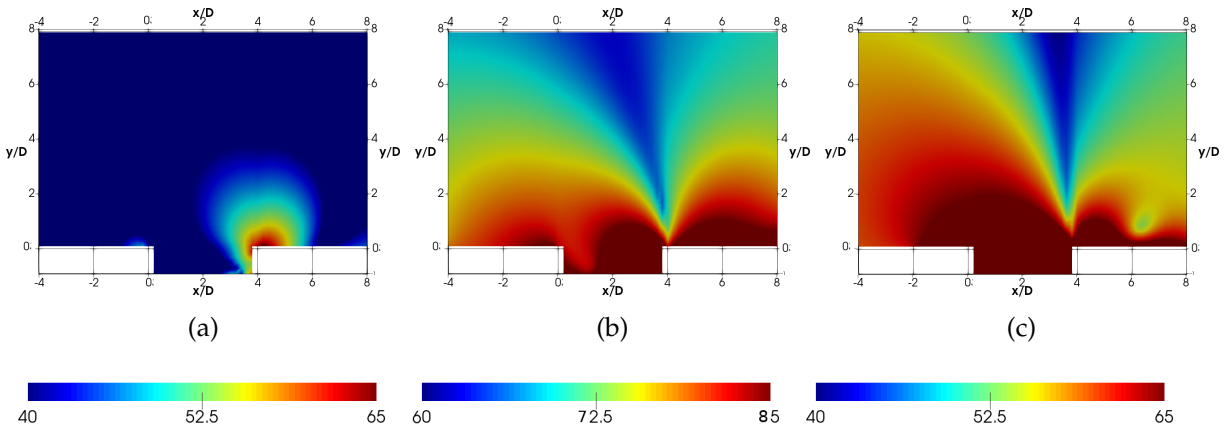

Figure 3.30: OASPL map in the near field. a) 3D-SL; b) 2D-WM; c) 3D-WM.

much higher (about 20dB) than the results for 3D-WM. Hence, when the cavity is oscillating in WM, the simulation should take into account the full three-dimensional Navier-Stokes equations in order to correctly capture the behaviour of the flow.

Oscillation Mode, $Re_D = 1500$

Figure 3.30-a) shows the OASPL in the near field for the case 3D-SL. As previously discussed, the flow field results obtained with the incompressible model used in this work is not suitable to predict the noise generated by the cavity in the SL mode due to the omission of the acoustic feedback. Nevertheless, it is worth noting that considering the time of integration corresponding to the interval in which the oscillations were sustained, the OASPL differs from the 3D-WM in both origin and directivity of noise. Therefore, a full compressible model has to be used to describe the physics of the SL mode.

Compressibility Effects, $Re_D = 1500$

Figure 3.31 shows the frequency spectrum obtained with DS and Curle's formulation at two observers located in the near field, the first located at $(x/D, y/D) = (-3, 5.5)$ and the second at $(x/D, y/D) = (5, 5.5)$. While Curle method can not be expected to describe accurately the near acoustic field, it predicts quite well the frequency spectra for both observers. The main difference occurs for the spectra of the downstream observer (located above the turbulent area), where more energy is contained in the lower part of the spectrum for DS. This slight difference can not be due to scattering effects such as reflections (not considered in Curle's analogy) because for the range of frequencies considered in this work the cavity satisfies the Hemholtz criteria. Instead, it seems to be related with volumetric sources acting as quadrupoles,

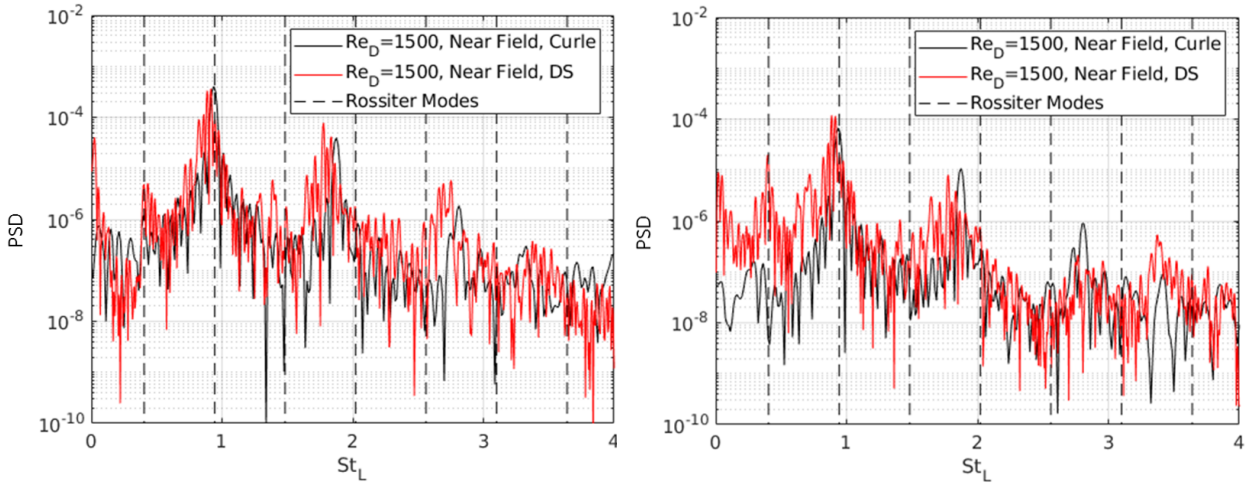

Figure 3.31: Frequency spectra of an observer for 1500-I and 1500-C. Left: $(x/D, y/D) = (-3, 5.5)$. Right: $(x/D, y/D) = (5, 5.5)$.

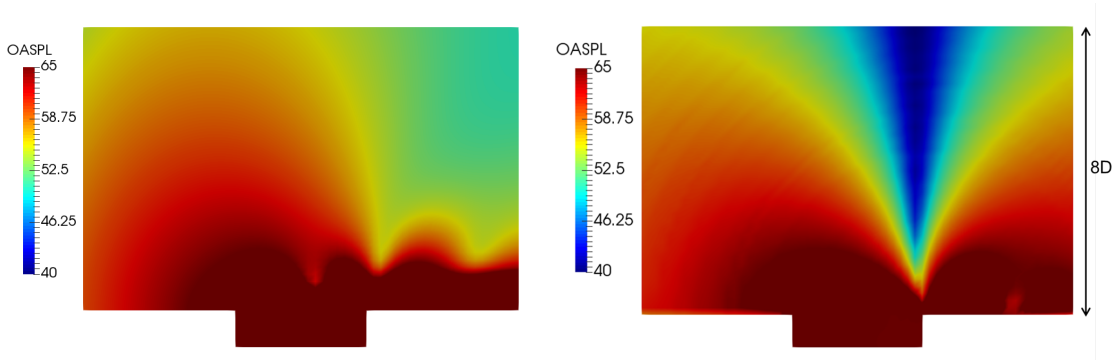

Figure 3.32: OASPL in the near field. Left: DS. Right: Curle.

which would be difficult to evaluate in a three-dimensional configuration.

Figure 3.32 shows the OASPL map in the near field using DS (left) and Curle (right). While upstream values are reasonably well captured even near the wall (where the dipole behaviour is dominant), the areas downstream and in the cavity are not, due to the presence of quadrupoles and turbulent fluctuations in this area (see Fig.3.10). As a remark, Figure 3.32 (left) includes the total acoustic fluctuating pressure (dipoles and quadrupoles) and the turbulent fluctuating pressure.

The BISPL (Band Integrated Sound Pressure Level) for the near and far field domains are shown in the figures of Table 3.4. The integrated frequency bands are defined around the three main St_L shown in Figure 3.31: $0.7<St_L<1.1$, $1.6<St_L<2.0$ and $2.6<St_L<3$. In the near field (top row), the band $0.7<St_L<1.1$ is the most energetic followed by the band $1.6<St_L<2.0$. However, the frequency bands $1.6<St_L<2.0$ and $2.6<St_L<3$ are mostly relevant in the turbulent area and thus associated with hydro-

	$0.7<St_L<1.1$	$1.6<St_L<2.0$	$2.6<St_L<3.0$
Near Field (DS)	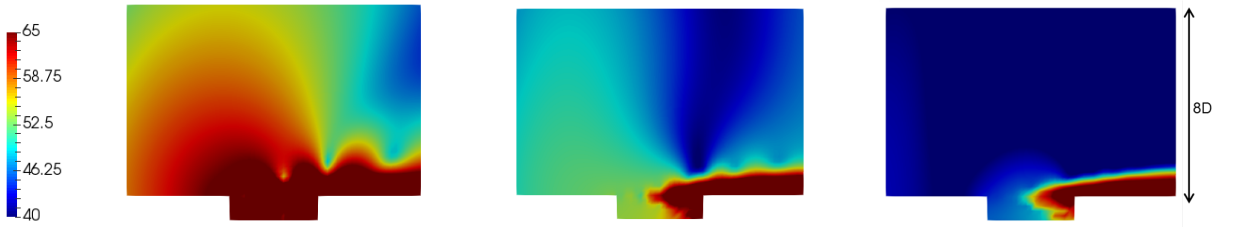		
Far Field (Curle)	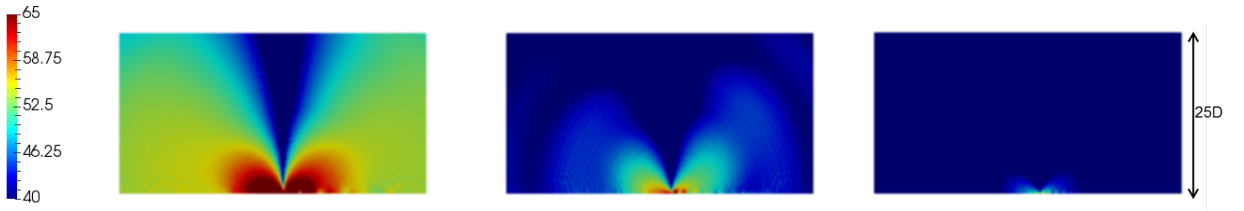		

Table 3.4: BISPL in the near and far field for $0.7<St_L<1.1$, $1.6<St_L<2.0$ and $2.6<St_L<3$ at $Re_D = 1500$.

dynamic pressure disturbances. This would explain why these two bands are much less important in the far field (bottom row), whereas the first band is very intense even far from the cavity. It should also be remarked that as a consequence of the high pressure disturbances on the right cavity wall, the lowest frequency band has a dipole behaviour with minimum directivity above the trailing edge.

Reynolds Number Influence, $Re_D = 1500$ and $Re_D = 5000$

Figure 3.33 shows the OASPL distribution on the far field for $Re_D = 5000$. In this case, the OASPL distribution shows a similar dipolic behaviour as for $Re_D = 1500$: two different lobes arising from the trailing edge of the cavity which progressively decrease as the observer moves away from the cavity. However, the acoustic intensity for $Re_D = 5000$ is slightly lower than for $Re_D = 1500$. This is more clearly appreciated in Figure 3.34 which compares the directivity pattern for $Re_D = 5000$ and $Re_D = 1500$ for the observers located at distance $22D$ from the trailing edge of the cavity. For $Re_D = 5000$, the region with less radiation (from $\alpha \approx 80°$ to $\alpha \approx 110°$) the acoustic intensity is slightly higher than for $Re_D = 1500$. This is due to the larger pressure fluctuations on the bottom cavity wall and downstream wall which radiate in the y-direction. On the other hand, the noise radiated closest to the upstream and downstream wall (from $\alpha \approx 0°$ to $\alpha \approx 30°$ and $\alpha \approx 150°$ to $\alpha \approx 180°$) the OASPL values are lower for $Re_D = 5000$ than for $Re_D = 1500$ due to larger pressure fluctuations on the right wall of the cavity.

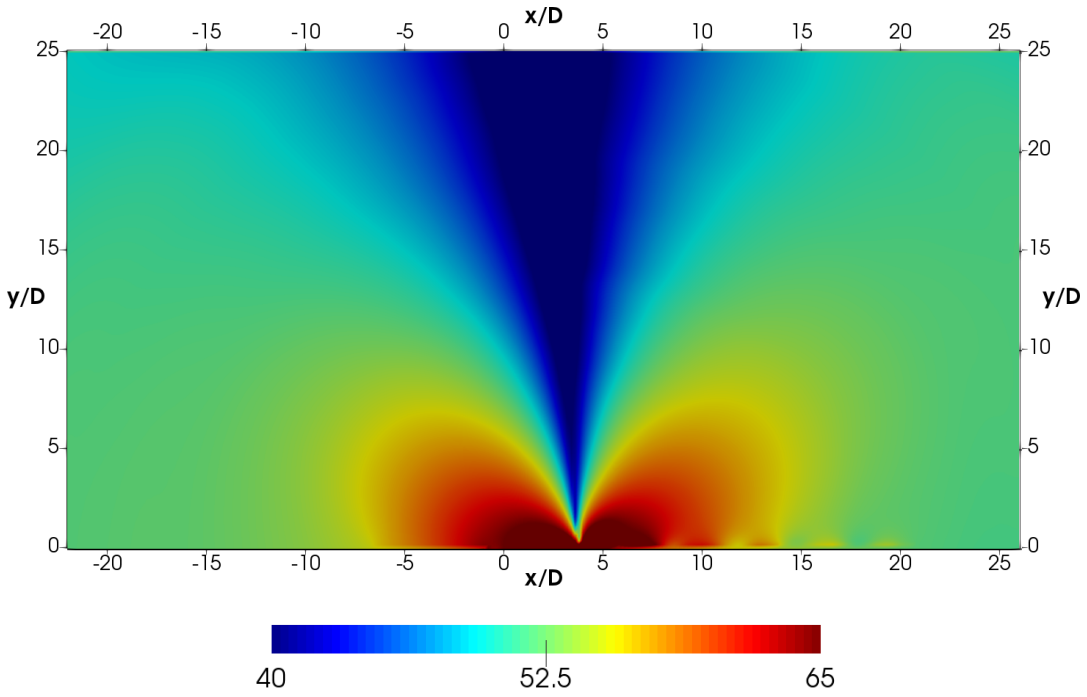

Figure 3.33: OASPL in the far field for $Re_D = 5000$.

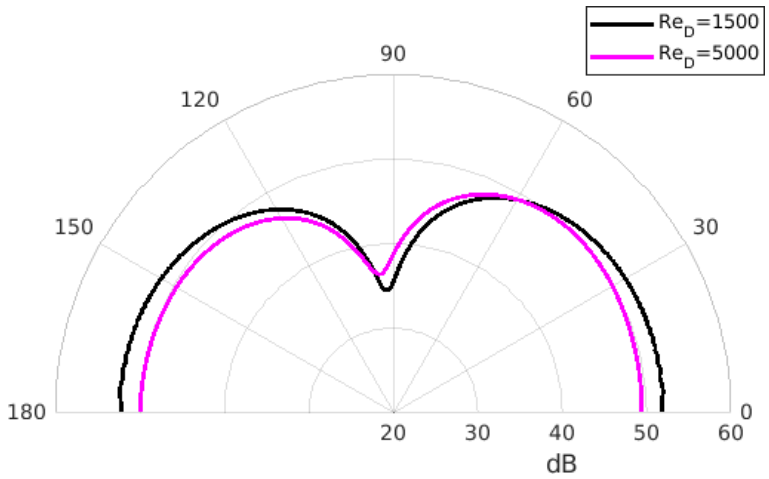

Figure 3.34: OASPL directivity for $Re_D = 1500$ and $Re_D = 5000$. The observers are located at distance $22D$ from trailing edge of the cavity.

The comparison of the frequency spectrum for the observer located at $(x/D, y/D, z/D) = (-3, 5.5, 0)$ between both Reynolds numbers is shown in Figure 3.35. The dominant St_L has transitioned from the second stage of Rossiter, $St_L = 0.9$, to the third, $St_L = 1.5$, as predicted when discussing the different number of shedding vortices inside the shear layer (see Figures 3.10 and 3.17). Additionally, the Hemholtz criteria should also be verified for the third Rossiter mode. In this case, $He = 0.2$<1, thus Equation 2.14 is also satisfied.

Finally, in terms of the Strouhal number, the dimensional frequency for the context of our application is calculated as

$$f = \frac{St_L U_\infty}{4D} \tag{3.3}$$

Using the last expression, the results for $Re_D = 1500$ yield a dominant frequency of $f = 11.8kHz$ while for $Re_D = 5000$, $f = 6.0kHz$. Even if the cavities are very small, both frequencies are in the range of the human audible spectrum [74]. Therefore, geometrical optimisations of the cavity in order to control the radiated noise would be helpful in order to design silent and comfortable vehicles that avoid or at least minimise unwanted phenomena such as whistles. In the next section, the influence of the defined geometrical parameters of Figure 3.1 in the noise radiated by an open cavity is discussed.

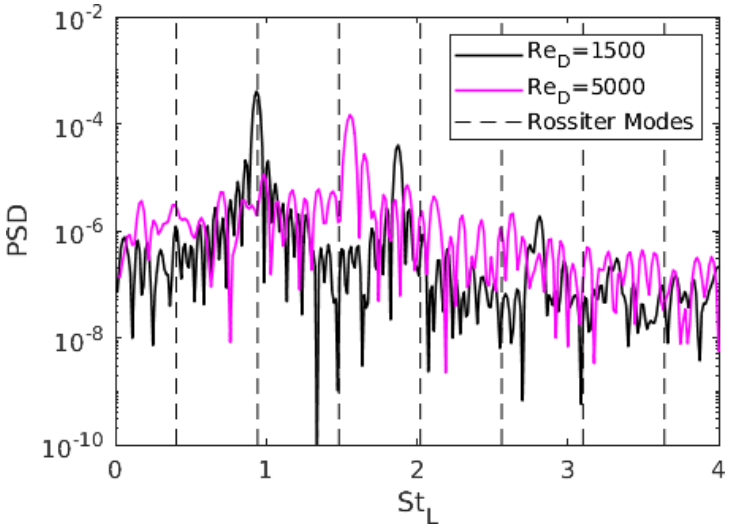

Figure 3.35: Frequency spectrum of the observer located at $(x/D, y/D, z/D) = (-3, 5.5, 0)$ for $Re_D = 5000$.

Passive Noise Control Techniques, $Re_D = 5000$

Aside from the influence of different radiating directions due to the change of the wall normal vector, the two main contributors to Curle's integral are p and $\dot{p}$ along the wall, both inspected along this section. The root mean square of pressure and its time derivative, $<p_{rms}>$ and $<\dot{p}_{rms}>$ respectively, are shown in Figure 3.36. To quantify the performance of each modification, the integrated values of $<p_{rms}>$ and $<\dot{p}_{rms}>$ are evaluated as:

$$\phi^I = \int_{s^*=-4}^{s^*=20} \phi \, ds^*, \text{ , i=2..9,} \tag{3.4}$$

where ϕ is used to denote a generic variable.

The increments of $<p_{rms}>^I$ and $<\dot{p}_{rms}>^I$ with respect to the baseline case expressed in percentage are summarised in Table 3.5. The major reduction in $<p_{rms}>^I$ is achieved by cavities C2, C4 and C5, which reduce its value by nearly 40%. Cavity C6 also reduces the value of $<p_{rms}>^I$ by 20%. On the contrary, cavities C7 and C8 significantly increase the magnitude of $<p_{rms}>^I$ by 100% and 200%, respectively. This is in qualitative agreement with the results of [58], where the streamwise distribution of $<p_{rms}>$ shows a peak of similar magnitude for the baseline cavity and a cavity with a shorter trailing edge height, though higher values along the downstream wall. The results of [58] for a cavity with a larger trailing edge also show an increase in both the magnitude of the peak and along the downstream wall.

	C1	C2	C3	C4	C5	C6	C7	C8
$\Delta <p_{rms}>^I$ (%)	-	-44	+7	-43	-38	-19	+105	+198
$\Delta<\dot{p}_{rms}>^I$ (%)	-	-37	-2	-28	-5	-13	-6	+50
ΔOASPL (dB)	-	-2	+3	-9	-5	-2	-5	+5
St_L	1.5	1.0	1.3	1.4	1.5	1.5	0.9/1.5	1.5

Table 3.5: Increment of $<p_{rms}>^I$, $<\dot{p}_{rms}>^I$ and OASPL with respect to C1 for cavities C2 to C8 and main St_L for cavities C1 to C8.

Nevertheless, the order of magnitude of $<p_{rms}>$ for the baseline case is approximately three times lower than $<\dot{p}_{rms}>$. Moreover, in virtue of Equation 2.11, the contribution to the acoustic pressure of the term p decays with r^2 and the term $\dot{p}$ with r. Therefore, an efficient noise control mechanism should be able to reduce $<\dot{p}_{rms}>$. Such decrease can be achieved by suppressing the abrupt pressure gradient produced

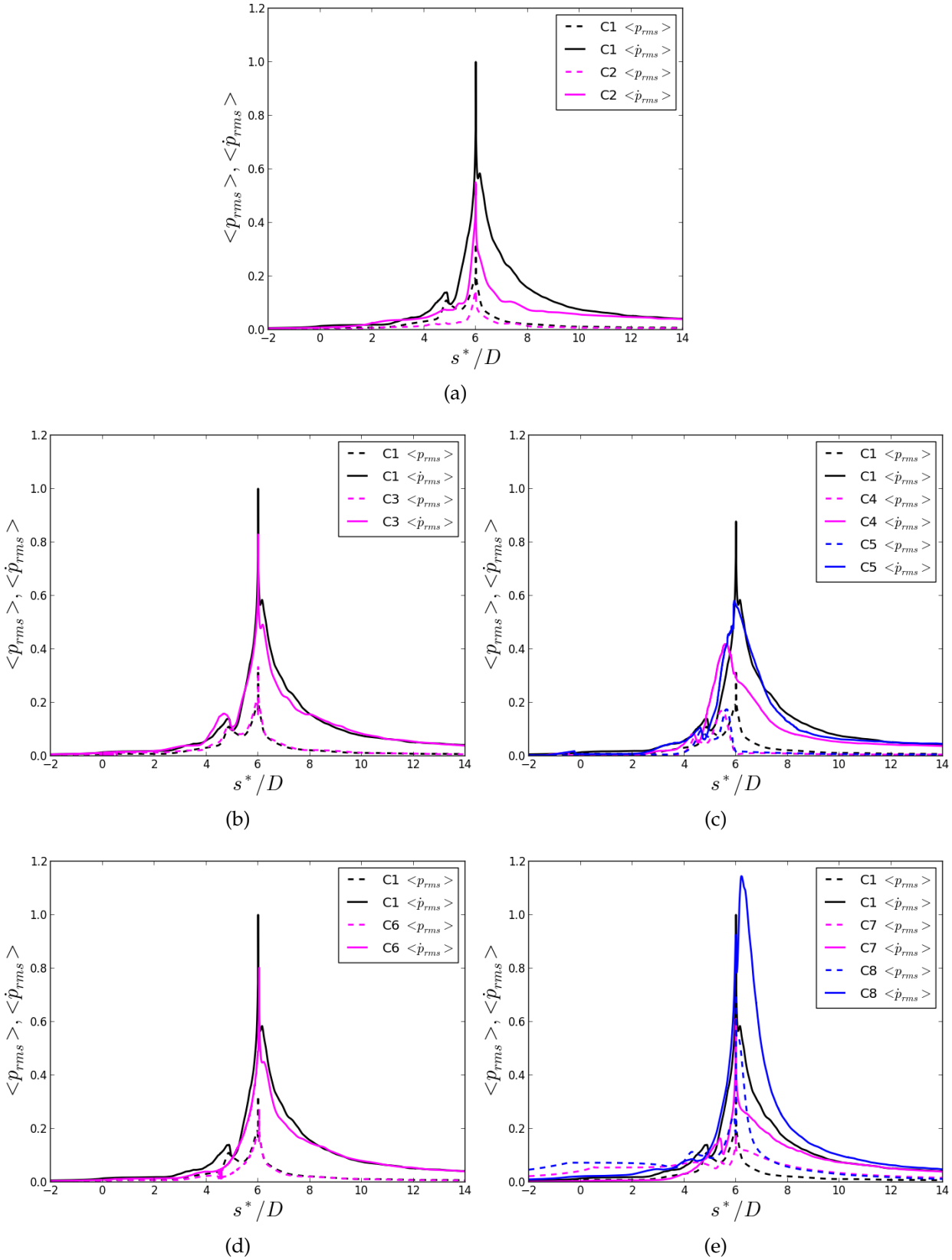

Figure 3.36: Spanwise and time averaged p_{rms} and $\dot{p}_{rms}$ along the wall. Comparison with the baseline cavity C1. a) C1 and C2; b) C1 and C3; c) C1, C4 and C5; d) C1 and C6; e) C1, C7 and C8.

by the singularity at the trailing edge. To this goal, the modifications C2, C4 and C7 are the most suitable since they reduce the term $<\dot{p}_{rms}>^I$ by 37%, 28% and 26%, respectively. On the contrary, the modification C8 is the most inefficient increasing this term by 50%, confirming the intuitive predictions.

Figure 3.37 displays the OASPL maps for cavities C1 to C8. As expected from the reductions in $<p_{rms}>$ and $<\dot{p}_{rms}>$, the modified cavities C2, C4, C5, C6 and C7 radiate less noise to the far field than cavities C1, C3 and C8. Figure 3.38 shows the OASPL for the observers located at distance $22D$ from the point $(x,y,z) = (4D,0,0)$. The average reduction achieved by each modification with respect to the baseline case for the observers defined in the directivity map of Figure 3.38 is collected in Table 3.5. On one hand, rounding the trailing edge with the maximum radius, C4, and shortening the rear wall of the cavity, C7, are the most effective modifications since their reductions are up to 9dB and 5dB, respectively. On the other hand, rounding the leading edge or enlarging the rear wall of the cavity result in more radiated noise to the far field with an averaged increase of 3dB and 5dB each. Therefore, neither C3 nor C8 would be suitable passive noise control techniques to reduce the acoustic intensity.

Finally, the influence of each modification on the acoustic frequency is addressed. Figure 3.39 shows the non-dimensional Power Spectral Density (PSD) value of the acoustic signal for an observer located at $(x,y,z) = (-3D,5.5D,0D)$. For the sake of a clearer representation the frequency spectrum of each modification has been shifted so the main frequencies of each modification can clearly be identified. For all the cavities, the main St_L has been calculated considering $L = 4D$ except for C2 where $L = 2D$ has been used.

A change of the dominant Rossiter mode is attributed to different impingement frequencies of the shedding vortices at the trailing edge, which dominates the acoustic spectrum of the noise radiated. This is the case of C2, which changes the main St_L to the second Rossiter mode due to the shorter distance travelled by the shedding vortices. The modification C7 also modifies the spectral composition, combining with similar energy the second and the third Rossiter mode. As explained in [58], the minimisation of the interaction of the shear layer with the trailing edge for C7 reveals that the cavity can also emit noise with frequencies typically associated to a backward step problem. When the trailing edge is taller than the leading edge, as in C8, the noise is again dominated by the noise originated at the trailing edge. The rest of the modifications do not significantly change the spectrum, hence only modifications C2 and C7 would be useful for passive control of the acoustic frequency.

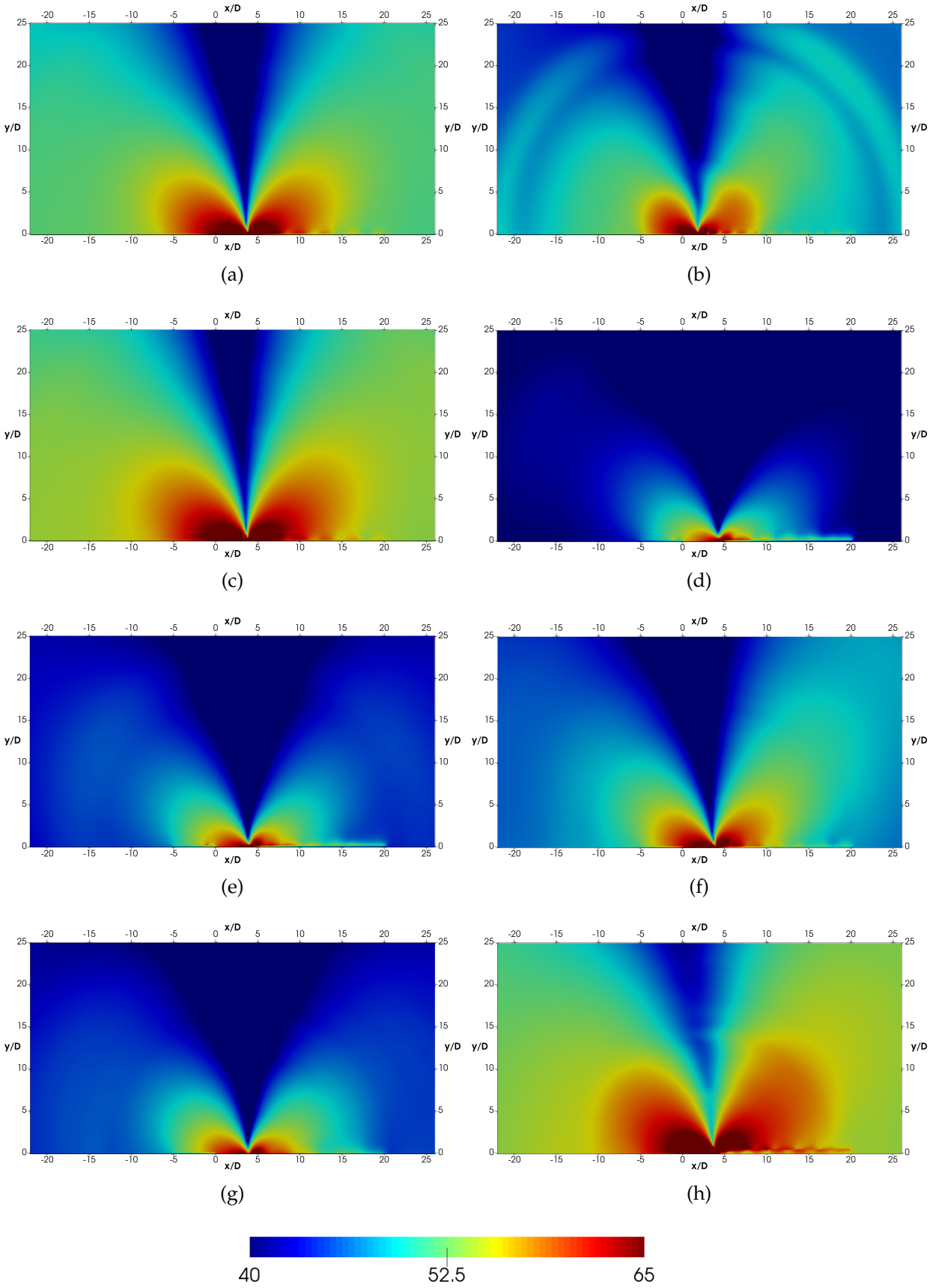

Figure 3.37: OASPL map. a) C1; b) C2; c) C3; d) C4; e) C5; f) C6; g) C7; f) C8.

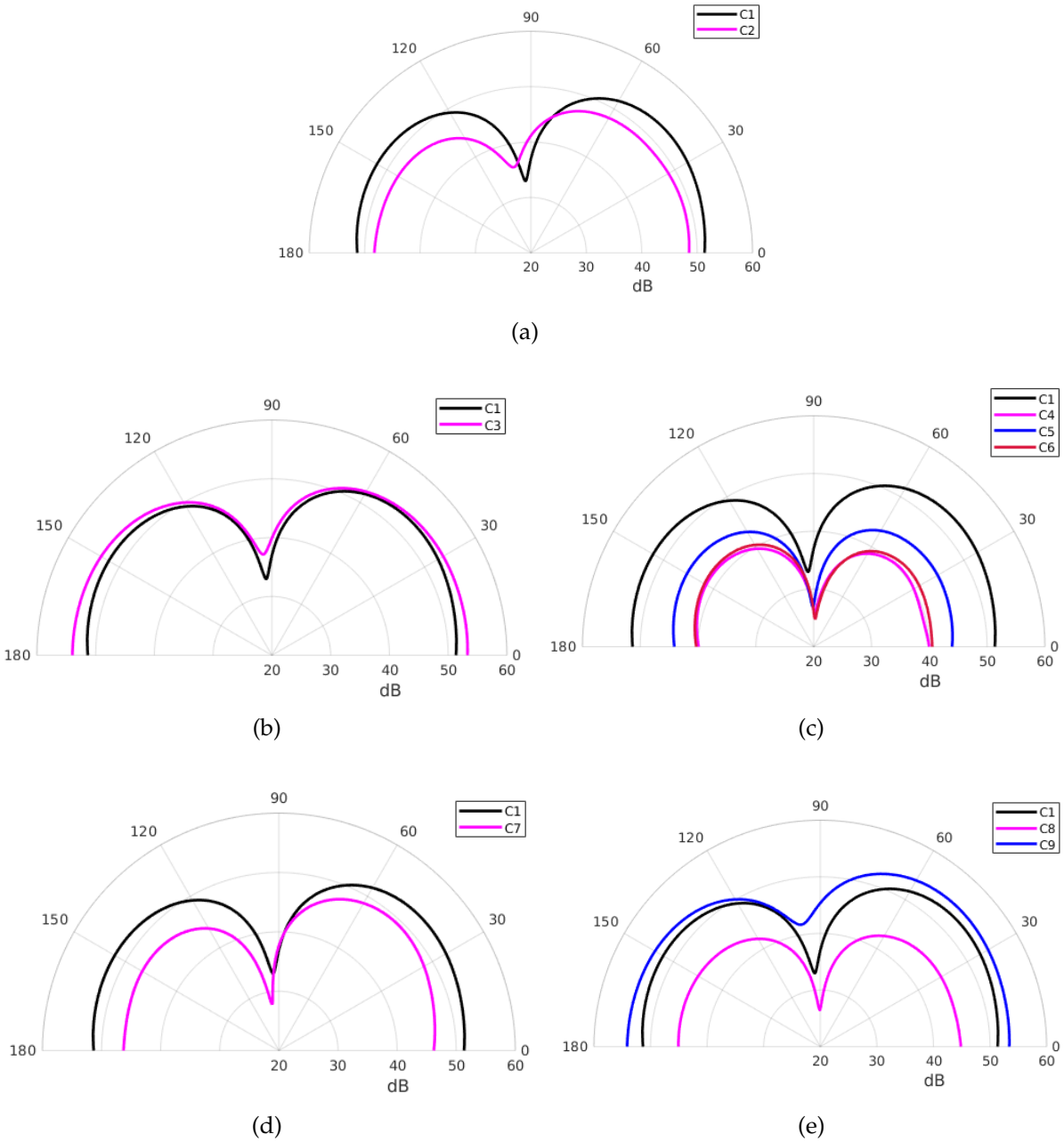

Figure 3.38: OASPL directivity. Comparison with the baseline cavity C1: a) C1 and C2; b) C1 and C3; c) C1, C4 and C5; d) C1 and C6; e) C1, C7 and C8.

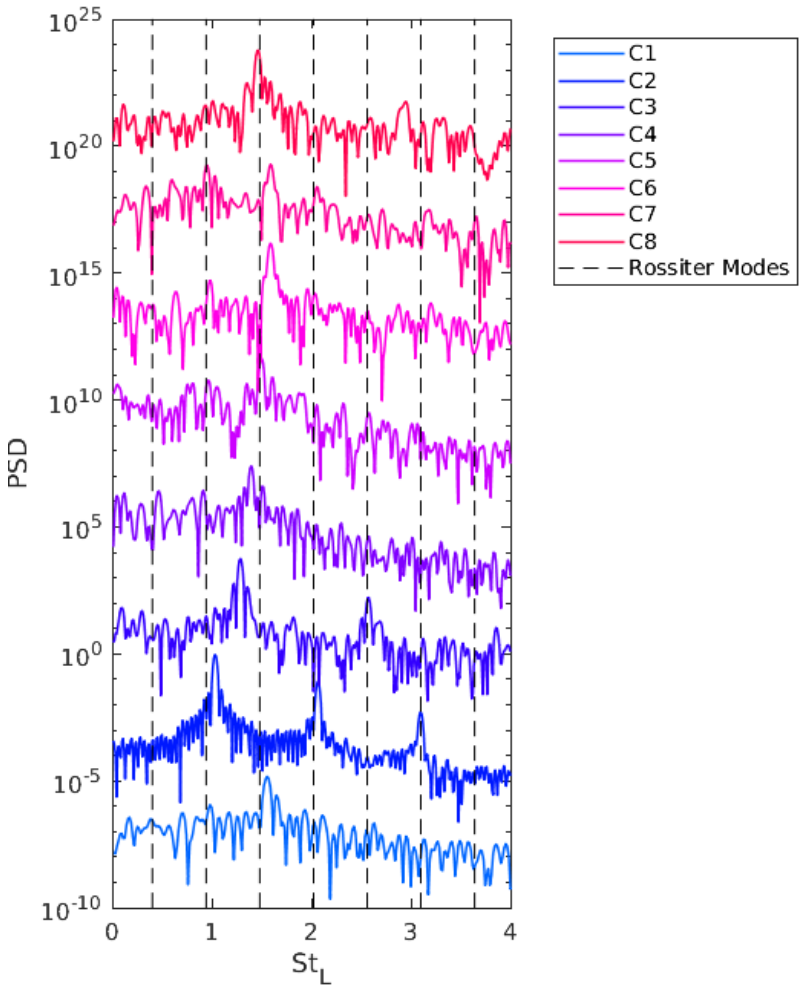

Figure 3.39: Frequency spectrum for an observer at $(x/D, y/D, z/D) = (-3, 5.5, 0)$ for cavities C1 to C8. Rossiter modes are also included.

3.5. Conclusions on Cavity Noise

In order to fully understand Curle's formulation, numerical simulations of sound radiated by a three-dimensional very wide open cavity with aspect ratio $L/D = 4$ at Reynolds number based on the cavity depth of $Re_D = 1500$ and $Re_D = 5000$ for Mach number $M = 0.1$ have been performed. Due to the low Reynolds number, no turbulence model has been used for the simulations at $Re_D = 1500$, while LES formulation has been considered for the incompressible simulation at $Re_D = 5000$ together with the subgrid-scale viscosity model proposed by Vreman [67].

A brief discussion at $M = 0.15$ about the two oscillation modes originally described by Gharib and Roshko [37], shear layer mode and wake mode, and the dimensional behaviour of the flow have also been given. The onset of one mode or the

other depends on the boundary layer thickness arriving at the inlet of the domain. For these parameters the transition occurs at $\frac{L}{\theta} \approx 75$ [38]. To trigger them, values of $\frac{L}{\theta} \approx 72$ for SL and $\frac{L}{\theta} \approx 101$ for WM have been simulated at the leading edge position. The results obtained show that the SL mode and the WM flow results are significantly different. The shear layer mode displays a two-dimensional behaviour while the wake mode shows three-dimensional structures as expected for a Reynolds number above $Re_D \approx 1200$. The vortex stretching mechanism, responsible for the enhancement of vorticity and the transport of energy towards the smaller scales, is not present in the two-dimensional wake mode results and therefore the vortices appearing in the two-dimensional simulation do not vanish. As a consequence, the pressure value over the wall changes completely, as well as the drag and other flow parameters. In agreement with [39], the absence of acoustic feedback in an incompressible flow model, results in decaying oscillations for the SL mode, that are not realistic. However, the incompressible flow model predicts realistic sustained oscillations for the WM. Respect to the acoustic results, the two-dimensional simulations for the WM are in fair agreement with previous studies which also consider a two-dimensional model. However, the solution of the same configuration considering a three-dimensional model are about an order of magnitude different. Thus, a two-dimensional simulation would predict a nonphysical high radiation.

For $Re_D = 5000$, the time averaged C_D is nearly 60% higher than at $Re_D = 1500$ due to the increase in pressure over the solid surfaces of the cavity, particularly around the right bottom corner of the cavity. The vortical structures identified at $Re_D = 5000$ are smaller inside the cavity and along the downstream wall. It has also been found that three shedding vortices lie inside the shear layer at $Re_D = 5000$ while only two at $Re_D = 1500$. For both Reynolds numbers, the St_L agrees with published experimental data [71]. In particular, at $Re_D = 1500$ it coincides with the second Rossiter mode and at $Re_D = 5000$ with the third. For both Reynolds numbers, the acoustic directivity pattern corresponds to a dipole with maximum radiation at $\alpha \approx 150^\circ$ and $\alpha \approx 50^\circ$. These results are in agreement with experimental works also based on Curle's analogy combined with PIV measurements [70]. Although the PSD values predicted by Curle are not in perfect agreement with DS in the closest area to the wake region in the near field, the frequency spectrum is in good agreement even if quadrupole sources are neglected.

Overall, the results presented in this study show that the acoustic behaviour of cavities can produce conspicuous acoustic phenomena in vehicle designs, such as whistles. For this reason, it has been investigated different passive noise control tech-

niques at $Re_D = 5000$ and $M = 0.1$, which can greatly influence the acoustic behaviour of cavities and avoid undesired acoustic problems if suitable modifications are applied in early stages of the design. To this aim, the far field noise of different geometry modifications such as the length of the cavity, the radius of the leading edge, the radius of the trailing edge, the radius of the right bottom edge and the distance in the y-axis between the leading and trailing edge have been considered.

With respect to the flow field results of the baseline case, it has been seen that the recirculation confined around the right bottom corner of the cavity generates large pressure values in this area and that the abrupt ejection of fluid to the downstream wall is the responsible of the intense pressure fluctuations on this wall. On one hand, the most effective geometrical modifications to reduce the pressure inside the cavity is to shorten the length of the cavity or to round the right bottom edge. On the other hand, to reduce the fluctuation of pressure after the trailing edge the most effective modification is to round the trailing edge, avoiding the abrupt ejection of fluid to the downstream wall.

Regarding the acoustic results, it has been shown that the order of magnitude of $<p_{rms}>$ for the baseline case is approximately 3 times lower than $<\dot{p}_{rms}>$. Moreover, as the term $<p_{rms}>$ decays with r^2 and the term $<\dot{p}_{rms}>$ with r, the noise control mechanism that reduces $<\dot{p}_{rms}>$ the most performs better acoustically. Indeed, rounding the trailing edge reduces the integral value of the term $<\dot{p}_{rms}>$ up to 50%, achieving a decrease of about 9dB in OASPL. On the contrary, a higher trailing edge increases the integral value of the term $<\dot{p}_{rms}>$ by 315%, increasing the OASPL up to 5dB. While none of the configurations studied significantly change the dipolic directivity pattern of acoustic radiation, some of them modify the main frequency. In particular, when shortening the length of the cavity or when reducing the height of the trailing edge, the Rossiter mode shifts from the third to the second mode.

4

Computational Aeroacoustics in the Automotive Industry

4.1. Industrial Context

The acoustic field inside a car cabin for low driving speeds is dominated by the engine or tire noise. However, for moderate high velocities (usually above 80 km/h), the noise generated by the interaction of the air with the external shape of the vehicle becomes more relevant. Such noise is generally considered unpleasant and it raises one of the most common complaints for customers. Moreover, vehicle manufacturers aim not only to improve and validate their products but also to leverage current technological advances to speed up their development processes. For this reason, Computational Aeroacoustics has become a very appealing area of research since it allows to predict the noise generated by air flow excited systems in early stages of the design process.

Physically, the aeroacoustic noise in a car is mainly produced by the strong pressure fluctuations arising from the interaction of the flow with the side mirror, the A-pillar or the cavities existing between different components of the vehicle (see Figures 4.1 and 4.2). At each point of the flow field domain, the pressure is composed by the hydrodynamic pressure (i.e., the incompressible part of the flow field) and the acoustic pressure (i.e., the acoustic field caused by the compressible part of the flow field). For typical car speeds, the Mach number is so low that the fluctuations of the compressible part of the flow are much smaller than those of the incompressible part

but their characteristic lengths and convection velocities have a higher correlation with the bending waves of the windows of the vehicle. As a consequence, it is usually accepted that the major part of the interior noise in the car cabin is generated by the compressible part of the external flow field arriving to the transmission surfaces. In other words, unless the car is not sufficiently watertight, the acoustic waves generated in these parts are transmitted to the interior through the vibration of the side window and windshield. Therefore, in order to minimise the transmitted noise and obtain the targeted acoustic comfort, engineers can reinforce the isolating properties of the transmission surfaces, which usually increases the cost of the product, or can optimise the shape of the radiating parts, recommended in early stages of the design process.

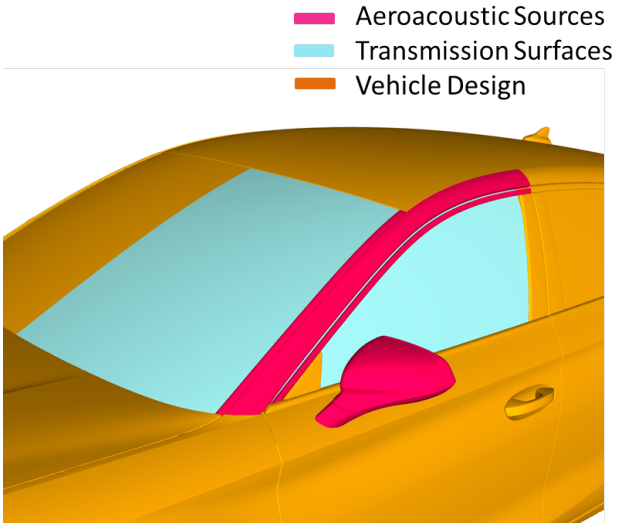

Figure 4.1: Aeroacoustic sources and transmission surfaces in a vehicle. Source: SEAT.

Regarding the second option, different designs are usually tested experimentally in a wind tunnel under different air flow velocities and angles of incidence using a prototype car at real scale as shown in Figure 4.3. Two type of characterisations of the vehicle are typically made in a wind tunnel testing. The first one consists on the detection of external acoustic sources by means of an array of microphones, as the one shown in Figure 4.4 a), located at a fixed distance from the car. The acoustic signal measured at each microphone of the array is post-processed with a technique known as beamforming, which projects over the external shape of the vehicle the localised sound sources as in Figure 4.5 a). In the recent years, techniques based on beamforming analysis combined with an acoustic numerical measurement have also been used for the localisation of sound sources. Although this method is out of the

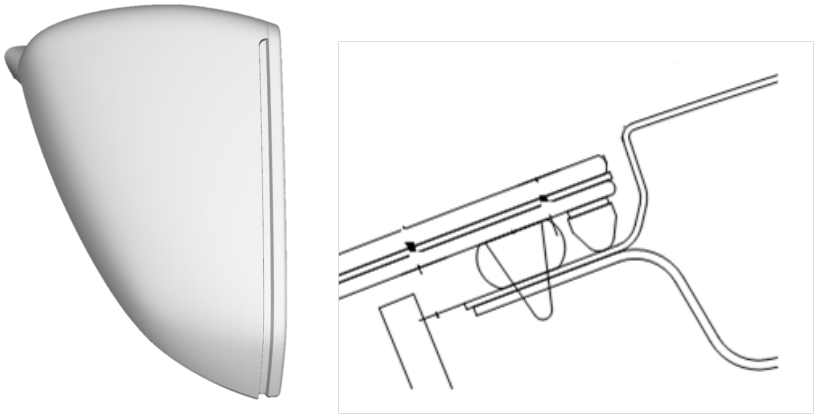

(a) (b)

Figure 4.2: Examples of cavities in a vehicle. a) Top casing of a side mirror; b) gap between the windshield and the ceiling of a car. Source: SEAT.

scope of this thesis, the reader can find more details about this type of analysis in [75]. The second type of characterisation consists on the measure of the internal noise at a standard driver's ear position. To this aim, a dummy body with a microphone located at each ear, also known as acoustic head, is used. The acoustic head is placed inside the car as shown in Figure 4.4 b). The recorded signal is post-processed, for instance using a one-third octave band spectrum as in Figure 4.5 b), and compared between different states in order to identify the most suitable configuration.

Figure 4.3: Wind tunnel facilities. Source: AUDI.

(a) (b)

Figure 4.4: Measuring instruments. a) Microphones array; b) acoustic head. Source: AUDI.

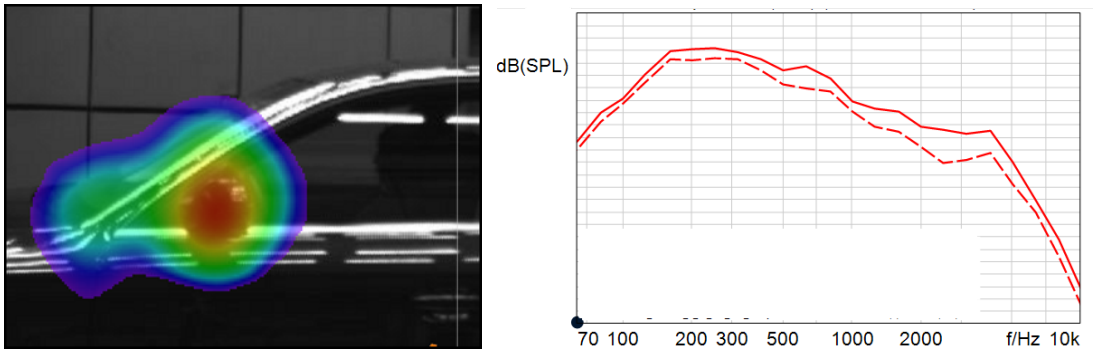

(a) (b)

Figure 4.5: Examples of measured results. a) Beamforming; b) 1/3 octave spectrum. Source: SEAT.

Nevertheless, there is a major drawback in the described process. Acoustic engineers need real-scale prototypes or production vehicles to measure. As a consequence, the time to modify the design of a new model is very tight and sometimes experimental conclusions arrive at a late phase of the vehicle development process, often implying other expensive solutions. For this reason, automotive industry sees in CAA a solution to gain insight on the aeroacoustic behaviour of the design during the early stages of the project, saving time and resources. Moreover, geometrical changes in virtual models are easier to be implemented allowing more complete and efficient parametric studies.

However, CAA simulations have also some limitations compared to experimentation. In particular, the computation of the transmitted sound to the interior of the vehicle or the acoustic response under non-stationary incident flows are still great challenges for numerical researchers. Thus, wind tunnel experiments or on-road mea-

surements remain still necessary in order to have the complete acoustic characterisation of a vehicle.

In the remaining of this chapter, some examples of the new CAA applications implemented within the development process of the automotive company SEAT within the course of this thesis are presented.

4.2. Side Mirror and A-pillar Noise Radiation Simulation

This section presents an application of a CAA methodology to a real industrial case. In particular, the acoustic radiation of the side mirror and the A-pillar of a car model provided by the company SEAT towards the side window and windshield of the car is calculated. In order to preserve the confidentiality of the results, the scales of the maps shown in the remaining of the chapter as well as the numerical details of the CFD and CAA simulations will be omitted.

Figure 4.6 shows the mean velocity on a section across the A-pillar and the side mirror. The air arriving to the A-pillar and the side mirror is detached from the car surface generating strong pressure fluctuations on the body, that according to Curle's analogy generate acoustic waves propagating throughout the domain. Figure 4.7 shows the root mean square of the pressure and pressure fluctuation on the side mirror and A-pillar surfaces. It should be remarked that the $<\dot{p}_{rms}>$ term is approximately 10^7 times higher than $<p_{rms}>$, so as happened with the cavity case the analysis and reduction of the pressure fluctuation term will be more effective for aeroacoustic noise control. As seen from the Figures, the bottom part of the A-pillar and the base of the side mirror are the most critical parts for noise generation. The air flowing through the bonnet of the car impacts on the windshield and escapes the water box through the bottom part of the A-pillar generating high pressure fluctuations on this region. The interaction of the detached air with the base of the side mirror as well as the interaction of the wake with its internal face also induces high pressure fluctuations on these parts.

The acoustic waves generated by the side mirror and the A-pillar travel to the side window and windshield where, by vibroacoustic excitation of the glass, are propagated to the interior. Figure 4.8 shows the 1000 Hz and the 4000 Hz 1/3 octaves radiated by the side mirror to the side window and Figure 4.9 the same 1/3 octaves radiated by the A-pillar to the side window and windshield. In this case, the noise radiated by the side mirror dominates the excitation of the side window for nearly

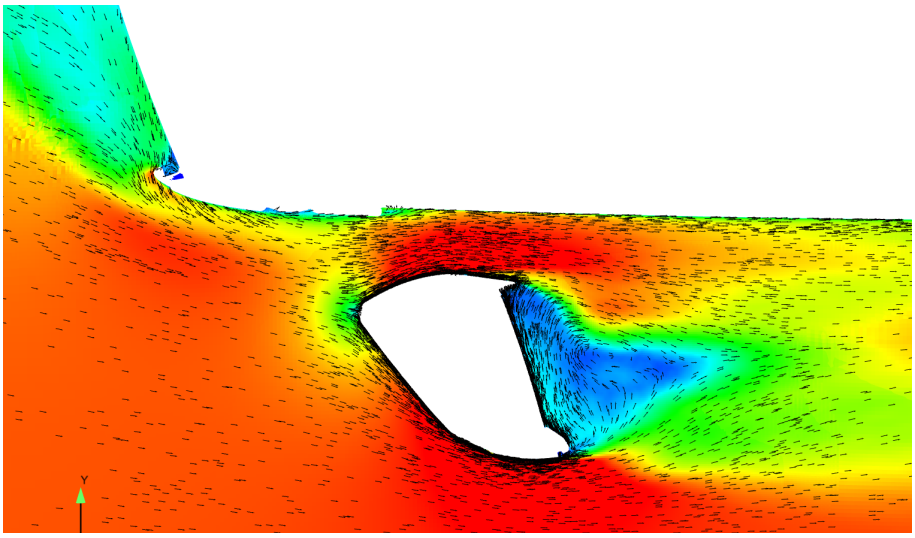

Figure 4.6: Mean velocity on a section across the A-pillar and the side mirror. Source: SEAT.

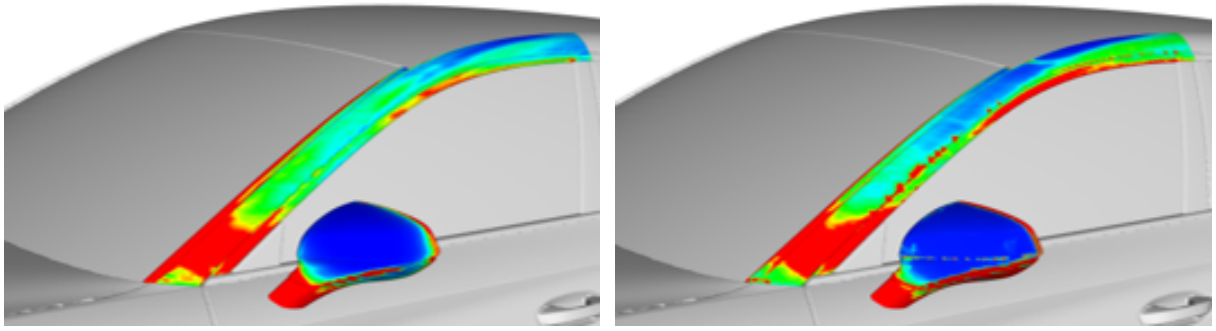

(a) (b)

Figure 4.7: a) <p_{rms}>; b) <$\dot{p}_{rms}$>. Source: SEAT.

the whole frequency spectrum while the noise radiated by the A-pillar travels mainly to the windshield and it is important for low to medium frequencies.

Based on this methodology, the automotive industry can compute and compare the acoustic radiation of different geometrical configurations and decide which one is more suitable for aeroacoustic performance. The assumption is that the greater the SPL distribution on the outside part of the window, the louder will be the noise inside the car. This hypothesis has long been used in wind tunnel testing when working with clay models, where internal noise can not be measured. It is important to emphasise that for early stages of the design process the industry is not as interested as the academia in the absolute accuracy of the noise measures but rather on the comparison of the noise generated by different configurations and on the clear physical understanding of the origin of such differences so as to discard designs with low

performance straight from the drawing table.

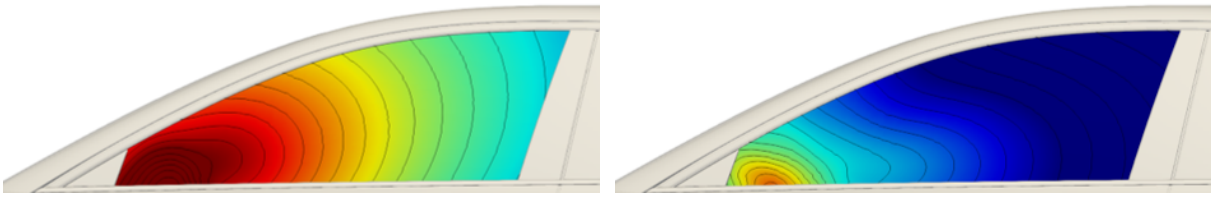

(a) (b)

Figure 4.8: Side mirror acoustic radiation to the side window. a) 1000 Hz; b) 4000 Hz. Source: SEAT.

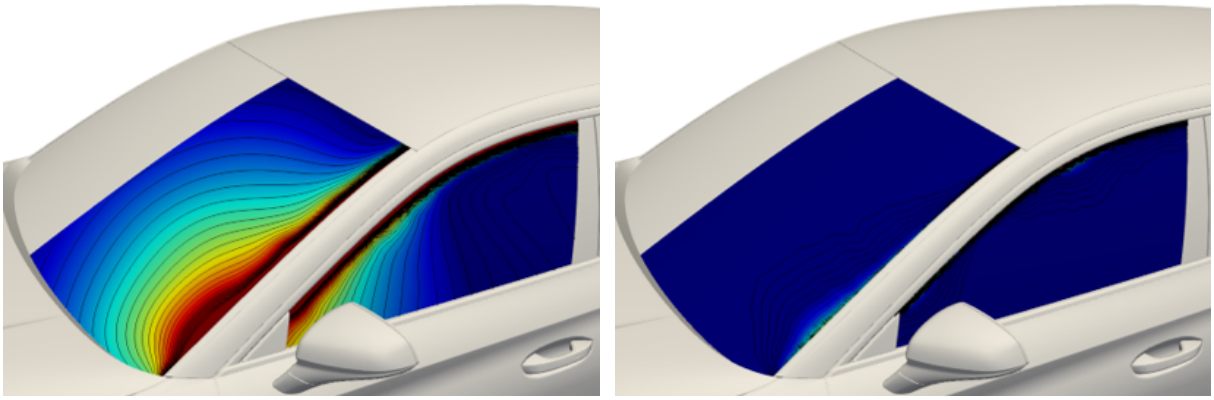

(a) (b)

Figure 4.9: A-pillar acoustic radiation the the side window and windshield. a) 1000 Hz; b) 4000 Hz. Source: SEAT.

5

Conclusions & Future Work

This chapter recapitulates the main conclusions of this research and highlights some open points that can draw the path for new research topics.

5.1. Conclusions

Firstly, an extensive review of the most popular computational aeroacoustic methods has been presented. While resolving the compressible Navier-Stokes equations (DS) would be the most direct way to compute sound, it has been concluded that hybrid methods are more suitable for industrial applications. In particular, Curle's analogy has been considered to be the most effective approach for the cases of study within this thesis. Curle's integral is computationally more affordable than other CAA methods and allows to obtain information about the contribution to the total acoustic pressure from each part of the surface.

In order to fully understand Curle's formulation, numerical simulations of wide open cavities with no interaction between the flow and the side walls at low subsonic speeds have been performed. Among all the different components of a vehicle, this geometry has been chosen due to its common presence in any type of vehicle design. This configuration is known to be the cause of conspicuous acoustic problems such as whistles due to the well defined tonal noise known in the literature as Rossiter modes.

The study has started focusing on the methodological aspects of the case. To this aim, a cost-effective Reynolds number has been considered, $Re_D = 1500$, for a base-

line cavity with aspect ratio $L/D = 4$. Under these conditions, it has been verified that the model of the problem should take into account the three-dimensional behaviour of the flow in order to correctly describe the flow pattern and acoustic performance. It has also been shown that for the SL mode the acoustic feedback mechanism is essential to model the real physics of the case. In other words, if the cavity oscillations correspond to the SL mode the compressible Navier-Stokes equations should be resolved. On the other hand, when the cavity is oscillating in WM, the acoustic results obtained with DS and Curle's analogy are in very good agreement except in the nearest area to the wake region where quadrupole sources are present.

After the advantages and limitations of the proposed method have been defined, the investigation has focused on a more realistic case for the industrial application contemplated. To this aim, the Reynolds number is increased up to $Re_D = 5000$ and different passive noise control techniques to minimise the noise emitted by the cavity have been evaluated. In particular, the noise control mechanisms are based on the modification of the length of the cavity, the radius of the leading edge, the radius of the trailing edge, the radius of the right bottom edge and the distance in the y-axis between the leading and trailing edge. The results have shown that the modifications on the trailing edge are the most effective to control the flow. They allow to reduce the pressure fluctuations produced by the recirculation confined inside the cavity and the abrupt ejection of the flow at the trailing edge. As a consequence, the overall sound pressure level can be decreased up to 9dB.

Finally, as the summit and most practical application of the content of this thesis, a review of the current aeroacoustic evaluation process implemented within the automotive industry has been explained. Nowadays, experimental techniques based on internal and external noise measurements have been presented. Although wind tunnel experiments or on-road measurements remain still necessary to have a precise picture of the passenger's acoustic comfort, the use of CAA during early stages of the design represent a cutting edge technology to compare different geometrical configurations and decide which one is more suitable for aeroacoustic performance. As an illustration of how the industry can take advantage of CAA, the results of the application of the presented methodology to a real industrial case have been presented. In particular, the acoustic radiation of the side mirror and the A-pillar to the external part of the windshield and side window have been computed. In the case presented the noise radiated by the side mirror dominates the excitation of the side window for nearly the whole frequency spectrum while the noise radiated by the A-pillar travels mainly to the windshield and it is important for low to medium frequencies.

5.2. Future Work

This section presents three open topics that the author believes are worth of further investigation and for which this thesis could be used as a starting point.

5.2.1. Volume Sources Influence

As explained in Chapter 2, one of the key points of interest of Curle's formulation is the omission of the volume integral for low Mach numbers. This assumption is based on the M^2 relation between the acoustic power generated between surface and volume sources:

$$\frac{P_{quad}}{P_{dip}} \approx M^2.$$

Nevertheless, in order to better evaluate the implications of the volume sources neglect, a comparison with the results obtained from a different approach which accounts for volume sources (e.g. Fwocs-Williams Hawkings) would be worth comparing.

5.2.2. Computational Beamforming

Acoustic beamforming is a signal processing technique used for sound sources localisation based on the direction of arrival and the time difference in which the sound reaches each microphone of the array. Aeroacoustic engineers in the automotive sector use this method in wind tunnel testing to detect the main sources of noise emitted by the external surfaces of the car helping them to develop optimum sound designs. While this method has been traditionally applied experimentally, the same approach can be used by means of a simulated acoustic signal calculated with a computational aeroacoustic formulation such as the one proposed within this thesis.

5.2.3. Interior Noise Transmission

Despite the good qualitative correlation obtained between the internal noise and the external noise arriving to the transmission surfaces of the car, it would be highly useful to extend the current industrial methodology to include a vibroacoustic simulation that accounts for the interaction of the vibration of the side window or windshield with the external noise. Thereby, the influence in the attenuation or amplification of

certain frequencies of the spectrum could be evaluated.

6

Publications

This chapter contains a relation of the authored accepted and under review publications derived of this research:

Journal Papers

- Martin, R., Soria, M., Lehmkuhl, O., Gorobets, A., & Duben, A. (2019). *Noise radiated by an open cavity at low Mach number: Effect of the cavity oscillation mode*. International Journal of Aeroacoustics, 18(6-7), 647-668.

- Martin, R., Soria, M., Lehmkuhl, A., Duben, A., & Gorobets, A. (2020). *Numerical Simulation of Noise Radiated by an Open Cavity at Mach 0.1 and Reynolds Numbers 1500 and 5000*. Manuscript submitted for publication.

- Martin, R., Soria, M., Rodriguez, I., & Lehmkuhl, O. (2020). *On the Flow and Passive Noise Control of an Open Cavity at Re=5000*. Manuscript submitted for publication.

Conference Papers

- Martín Navarrete, R., Soria Guerrero, M., Lehmkuhl, O., Gorobets, A., Cante Terán, J. C., & Vidal Pairot, P.. *Noise Radiated by an Open Cavity at Low Mach Number* in 10th International Conference on Computational Fluid Dynamics (ICCFD), Barcelona, 2018.

- Martín Navarrete, R., Soria Guerrero, M., Lehmkuhl, O., Gorobets, A., & Duben, A.. *Noise Radiated by an Open Cavity at Low Mach Number* in 5th International Workshop on Computational Experiments in Aaeroacoustics (CEAA), Kaliningrad, 2018.

- Martin, R., Soria Guerrero, M., Lehmkuhl, O., Gorobets, A., Duben, A., & Cante, J. C. (2019). *Noise Radiated by an Open Cavity at M= 0.1 and Re= 5000*. In 25th AIAA/CEAS Aeroacoustics Conference, Delft, 2019.

A

Lighthill's Analogy

In this appendix the analytical solution of a general inhomogeneous wave equation stated as in Proposition 1 is derived. Indeed, let ψ be the solution of the inhomogeneous wave equation:

$$\nabla^2\psi - \frac{1}{v^2}\frac{\partial^2\psi}{\partial t^2} = -g(x,y,z,t), \tag{A.1}$$

ans ϕ the solution of the homogeneous wave equation:

$$\nabla^2\phi - \frac{1}{v^2}\frac{\partial^2\phi}{\partial t^2} = 0. \tag{A.2}$$

Then, integrating over the domain V the equation: $\phi \cdot$ eq.A.1$-\psi \cdot$ eq.A.2:

$$\int_V \phi\nabla^2\psi - \psi\nabla^2\phi = \int_V (-\phi g + \frac{1}{v^2}\phi\frac{\partial^2\psi}{\partial t^2} - \frac{1}{v^2}\psi\frac{\partial^2\phi}{\partial t^2}). \tag{A.3}$$

The purpose is now to expand the equation above in order to solve it for ψ. To this aim, ϕ is considered in the form of the spherically symmetric solution of the homogeneous wave equation:

$$\phi(r,t) = \frac{1}{r}f\left(t + \frac{r}{v}\right),$$

where r is the distance between an observational point $(x',y',z') \in V$ of the magnitude ψ and the point (x,y,z), i.e,

$$r = \sqrt{(x-x')^2 + (y-y')^2 + (z-z')^2},$$

and f is an arbitrary function satisfying the homogeneous wave equation which will be conveniently chosen below.

Let us first develop the right-hand side of Equation A.3:

$$-\int_V \phi g + \frac{1}{v^2}\int_V \left(\phi\frac{\partial^2\psi}{\partial t^2} - \psi\frac{\partial^2\phi}{\partial t^2}\right) = -\int_V \phi g + \frac{1}{v^2}\frac{\partial}{\partial t}\int_V \left(\phi\frac{\partial\psi}{\partial t} - \psi\frac{\partial\phi}{\partial t}\right)$$

since

$$\frac{\partial}{\partial t}\left(\phi\frac{\partial\psi}{\partial t} - \psi\frac{\partial\phi}{\partial t}\right) = \frac{\partial\phi}{\partial t}\frac{\partial\psi}{\partial t} + \phi\frac{\partial^2\psi}{\partial t^2} - \frac{\partial\psi}{\partial t}\frac{\partial\phi}{\partial t} - \psi\frac{\partial^2\phi}{\partial t^2} = \phi\frac{\partial^2\psi}{\partial t^2} - \psi\frac{\partial^2\phi}{\partial t^2}$$

and V is not dependant on time. Integrating over the whole time,

$$-\int_{-\infty}^{\infty}\int_V \phi g + \frac{1}{v^2}\left(\int_V \left(\phi\frac{\partial\psi}{\partial t} - \psi\frac{\partial\phi}{\partial t}\right)\right)\Big|_{t=-\infty}^{t=\infty}. \tag{A.4}$$

As mentioned above $f\left(t+\frac{r}{v}\right)$ should be chosen conveniently. In particular, it is defined in such a way that the last term of the previous expression vanishes. The so-called *impulse function* satisfies this requirement and it is defined as:

$$f\left(t+\frac{r}{v}\right) = \frac{1}{\sqrt{2\pi}}\frac{e^{-\frac{(t+\frac{r}{v})^2}{2\delta^2}}}{\delta},$$

where δ is nearly zero but never reaches this value. May the reader notice that with this definition of $f\left(t+\frac{r}{v}\right)$, ϕ satisfies the homogeneous wave equation as requested. One important property of the impulse function is that this function vanishes everywhere except around an infinitesimal interval around $\frac{r}{v}$. Using this property, $\phi(x,y,z,\pm\infty) = 0$ and $\frac{\partial\phi}{\partial t}|_{t=\pm\infty} = \frac{(t+\frac{r}{v})}{\delta^2}f|_{t=\pm\infty} = 0$. Therefore, as intended, the second term in Equation A.4 vanishes.

Another important property of the impulse function is $F(-t') = \int_{-\infty}^{\infty} f(t+t')F(t)dt$. Using this property the first term of Equation A.4 becomes:

$$-\int_{-\infty}^{\infty}\int_V \phi g = -\int_V\int_{-\infty}^{\infty}\frac{g(x,y,z,t)}{r}f\left(t+\frac{r}{v}\right) = -\int_V \frac{g(x,y,z,-\frac{r}{v})}{r}.$$

Let us now develop the left-hand side of Equation A.3 using the property $\nabla^2(ab) = a\nabla(b) + b\nabla(a)$ (with $a_1 = \phi$, $b_1 = \nabla\psi$) and $a_2 = \psi$, $b_2 = \nabla\phi$) and the divergence theorem,

$$\begin{aligned}\int_V (\phi\nabla^2\psi - \psi\nabla^2\phi)dV &= \int_V (\nabla(\phi\nabla\psi) - \nabla\phi\nabla\psi - \nabla(\psi\nabla\phi) + \nabla\phi\nabla\psi)dV \\ &= \int_V (\nabla(\phi\nabla\psi) - \nabla(\psi\nabla\phi))dV \\ &= \int_V (\nabla(\phi\nabla\psi - \psi\nabla\phi))dV \\ &= \int_S \left(\phi\frac{\partial\psi}{\partial n} - \psi\frac{\partial\phi}{\partial n}\right) dS.\end{aligned}$$

As ϕ has a singularity in $r = 0$, a small sphere of radius r_2 that bounds the observation point (x', y', z') with surface S_2 is considered, so V is externally bounded by S_1 and internally by S_2 (see Figure A.1). Therefore,

$$\int_S \left(\phi\frac{\partial\psi}{\partial n} - \psi\frac{\partial\phi}{\partial n}\right) dS = \int_{S_1} \left(\phi\frac{\partial\psi}{\partial n} - \psi\frac{\partial\phi}{\partial n}\right) dS_1 + \int_{S_2} \left(\phi\frac{\partial\psi}{\partial n} - \psi\frac{\partial\phi}{\partial n}\right) dS_2.$$

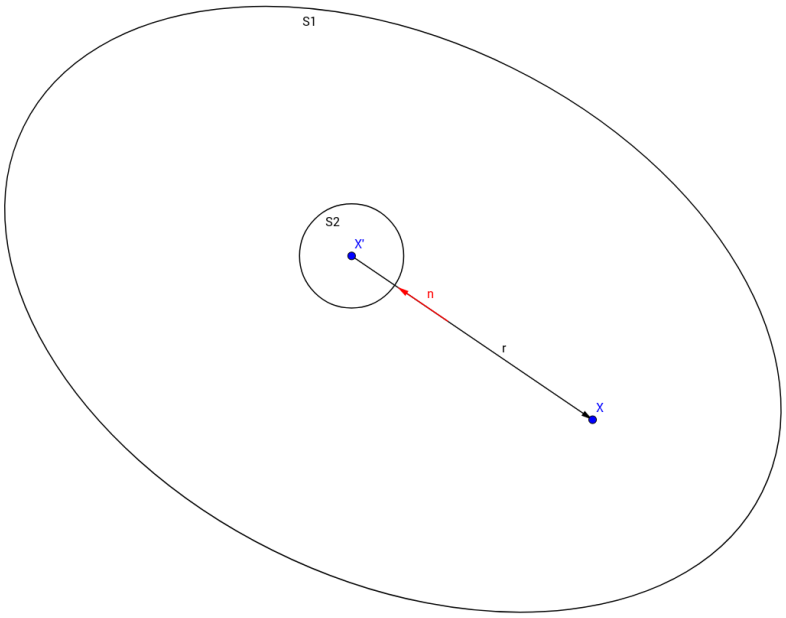

Figure A.1: Domain definition for Lighthill's solution proof.

Over the surface S_2, the normal vector points inwards ($\frac{\partial}{\partial n} = -\frac{\partial}{\partial r}$) and the second term of the right-hand side of the last expression becomes:

$$\begin{aligned}
\int_{S_2}\left(\phi\frac{\partial\psi}{\partial n}-\psi\frac{\partial\phi}{\partial n}\right)dS_2 &= -\int_{S_2}\left(\phi\frac{\partial\psi}{\partial r}-\psi\frac{\partial\phi}{\partial r}\right)|_{r=r_2}dS_2 \\
&= -\int_{S_2}\frac{1}{r_2}f\left(t+\frac{r_2}{v}\right)\frac{\partial\psi}{\partial r}|_{r=r_2}dS_2 \\
&+ \int_{S_2}\psi\,\frac{\partial\left(\frac{1}{r}f\left(t+\frac{r}{v}\right)\right)}{\partial r}|_{r=r_2}dS_2 \\
&= -\frac{1}{r_2}f\left(t+\frac{r_2}{v}\right)\int_{S_2}\frac{\partial\psi}{\partial r}|_{r=r_2}dS_2 \\
&+ \left(-\frac{f(t+\frac{r_2}{v})}{r_2^2}+\frac{1}{r_2}\,\frac{\partial f(t+\frac{r}{v})}{\partial r}|_{r=r_2}\right)\int_{S_2}\psi|_{r=r_2}dS_2 \\
&= -f\left(t+\frac{r_2}{v}\right)r_2\int_{S_2}\frac{\partial\psi}{\partial r}|_{r=r_2}\sin\theta d\theta d\gamma \\
&+ \left(-f\left(t+\frac{r_2}{v}\right)+r_2\frac{\partial f(t+\frac{r}{v})}{\partial r}|_{r=r_2}\right)\int_{S_2}\psi|_{r=r_2}\sin\theta d\theta d\gamma.
\end{aligned}$$

Making the sphere surrounded by S_2 infinitesimally small, i.e, $r_2 \to 0$,

$$\int_{S_2}\left(\phi\frac{\partial\psi}{\partial n}-\psi\frac{\partial\phi}{\partial n}\right)dS_2 = -4\pi f(t)\psi(x',y',z',t). \tag{A.5}$$

Integrating A.5 over the whole time and using again the properties of f:

$$\int_{-\infty}^{\infty}-4\pi f(t)\psi(x',y',z',t)dt = -4\pi\psi(x',y',z',0).$$

Summing up, each part of Equation A.3 has been transformed to:

$$\int_V \phi\nabla^2\psi-\psi\nabla^2\phi = -4\pi\psi(x',y',z',0)+\int_S\int_{-\infty}^{\infty}\left(\phi\frac{\partial\psi}{\partial n}-\psi\frac{\partial\phi}{\partial n}\right)dtdS,$$

$$\int_V(-\phi g+\frac{1}{v^2}\phi\frac{\partial^2\psi}{\partial t^2}-\frac{1}{v^2}\psi\frac{\partial^2\phi}{\partial t^2}) = -\int_V\frac{g(x,y,z,-\frac{r}{v})}{r}dV$$

Substituting these results into Equation A.3 and isolating $\psi(x',y',z',0)$:

$$\begin{aligned}
\psi(x',y',z',0) &= \frac{1}{4\pi}\int_V\frac{g(x,y,z,-\frac{r}{v})}{r}dV \\
&+ \frac{1}{4\pi}\int_S\int_{-\infty}^{\infty}\left(\frac{1}{r}f\left(t+\frac{r}{v}\right)\frac{\partial\psi}{\partial n}-\psi\frac{\partial(\frac{1}{r}f\left(t+\frac{r}{v}\right))}{\partial n}\right)dtdS.
\end{aligned} \tag{A.6}$$

Equation A.6 can further be simplified developing the last term of the last integral in the right hand side. Firstly,

$$\begin{aligned}\psi\frac{\partial(\frac{1}{r}f\,(t+\frac{r}{v}))}{\partial n} &= -\frac{\psi f(t+\frac{r}{v})}{r^2}\frac{\partial r}{\partial n}+\psi\frac{1}{r}\frac{\partial(f(t+\frac{r}{v}))}{\partial n}\\ &= -\frac{\psi f(t+\frac{r}{v})}{r^2}\frac{\partial r}{\partial n}+\psi\frac{1}{r}\frac{\partial f(u)}{\partial u}\frac{\partial u}{\partial n}\\ &= -\frac{\psi f(t+\frac{r}{v})}{r^2}\frac{\partial r}{\partial n}+\psi\frac{1}{r}\frac{\partial f(t+\frac{r}{v})}{\partial t}\frac{\partial u}{\partial r}\frac{\partial r}{\partial n}\\ &= -\frac{\psi f(t+\frac{r}{v})}{r^2}\frac{\partial r}{\partial n}+\psi\frac{1}{rv}\frac{\partial f(t+\frac{r}{v})}{\partial t}\frac{\partial r}{\partial n},\end{aligned}$$

where it has been used that if $u=t+\frac{r}{v}$, $\frac{\partial f(u)}{\partial u}=\frac{\partial f(t+\frac{r}{v})}{\partial t}\frac{\partial t}{\partial u}=\frac{\partial f(t+\frac{r}{v})}{\partial t}$. Replacing last expression in A.6 and integrating now over the whole time:

$$\begin{aligned}\int_{-\infty}^{\infty}\left(\frac{1}{r}f\left(t+\frac{r}{v}\right)\frac{\partial\psi}{\partial n}-\psi\frac{\partial(\frac{1}{r}f\,(t+\frac{r}{v}))}{\partial n}\right)dt=\\ \int_{-\infty}^{\infty}\left(\frac{1}{r}f\left(t+\frac{r}{v}\right)\frac{\partial\psi}{\partial n}+\frac{\psi f(t+\frac{r}{v})}{r^2}\frac{\partial r}{\partial n}-\psi\frac{1}{rv}\frac{\partial f(t+\frac{r}{v})}{\partial t}\frac{\partial r}{\partial n}\right)dt.\end{aligned}\tag{A.7}$$

Integrating the last part of Equation A.7 and using that f is only non-zero around r/v:

$$\begin{aligned}\int_{-\infty}^{\infty}\psi\frac{1}{rv}\frac{\partial f(t+\frac{r}{v})}{\partial t}\frac{\partial r}{\partial n}dt=\frac{1}{rv}\frac{\partial r}{\partial n}\int_{-\infty}^{\infty}\psi\frac{\partial f(t+\frac{r}{v})}{\partial t}dt\\ =\frac{1}{rv}\frac{\partial r}{\partial n}\left(\psi f\left(t+\frac{r}{v}\right)|_{-\infty}^{\infty}-\int_{-\infty}^{\infty}f\left(t+\frac{r}{v}\right)\frac{\partial\psi}{\partial t}dt\right)=-\frac{1}{rv}\frac{\partial r}{\partial n}\int_{-\infty}^{\infty}f(t+\frac{r}{v})\frac{\partial\psi}{\partial t}dt.\end{aligned}$$

Considering again that $F(-t')=\int_{-\infty}^{\infty}f(t+t')F(t)dt$, Equation A.7 becomes:

$$\begin{aligned}\int_{-\infty}^{\infty}\left(\frac{1}{r}f\left(t+\frac{r}{v}\right)\frac{\partial\psi}{\partial n}+\frac{\psi f(t+\frac{r}{v})}{r^2}\frac{\partial r}{\partial n}-\frac{1}{rv}\frac{\partial r}{\partial n}f(t+\frac{r}{v})\frac{\partial\psi}{\partial t}dt\right)dt=\\ \frac{1}{r}\frac{\partial\psi}{\partial n}|_{t=-r/v}+\psi|_{t=-r/v}\frac{1}{r^2}\frac{\partial r}{\partial n}+\frac{1}{rv}\frac{\partial r}{\partial n}\frac{\partial\psi}{\partial t}|_{t=-r/v}.\end{aligned}$$

Therefore, the solution of the inhomogeneous wave equation given by Equation A.6 becomes

$$\begin{aligned}\psi(x',y',z',0) &= \frac{1}{4\pi}\int_V\frac{g(x,y,z,-\frac{r}{v})}{r}dV\\ &+ \frac{1}{4\pi}\int_S\left(\frac{1}{r}\frac{\partial\psi}{\partial n}|_{t=-r/v}+\frac{\psi|_{t=-r/v}}{r^2}\frac{\partial r}{\partial n}+\frac{1}{rv}\frac{\partial r}{\partial n}\frac{\partial\psi}{\partial t}|_{t=-r/v}\right)dS.\end{aligned}$$

Finally, as the reference time can be arbitrarily chosen, last expression can be rewritten as:

$$\boxed{\psi(x',y',z',t) = \frac{1}{4\pi}\int_V \frac{1}{r}[g]dV + \frac{1}{4\pi}\int_S \left(\frac{1}{r}\left[\frac{\partial\psi}{\partial n}\right] + \frac{[\psi]}{r^2}\frac{\partial r}{\partial n} + \frac{1}{vr}\frac{\partial r}{\partial n}\left[\frac{\partial\psi}{\partial t}\right]\right)dS,}$$

where $[*]$ means the evaluation of the function at the retarded time $\tau = t - \frac{r}{v}$.

B

Curle's Analogy

In this Appendix, it is deduced the original modfication proposed by Curle for Lighthill's solution when the boundary of the domain includes a solid surface. To this aim, the mathematical manipulation of Equation 2.9 makes use of the following properties:

1. The chain rule.

2. T_{ij} and $\frac{\partial T_{ij}}{\partial y_i}$ are independent of the observer's position, i.e, their derivatives with respect to x_i are 0.

3. $\frac{\partial r}{\partial x_i} = -\frac{\partial r}{\partial y_i}$.

4. Divergence theorem.

On one hand, the volume integral of Equation 2.9 can be developed as follows:

$$
\begin{aligned}
& \int_V \frac{1}{r}\left[\frac{\partial^2 T_{ij}}{\partial y_i \partial y_j}\right] dV \\
= & \int_V \left[\frac{\partial}{\partial y_i}\left(\frac{\partial T_{ij}}{\partial y_j}\frac{1}{r}\right)\right] dV - \int_V \frac{\partial\left(\frac{1}{r}\right)}{\partial y_i}\left[\frac{\partial T_{ij}}{\partial y_j}\right] dV \\
= & \int_V \left[\frac{\partial}{\partial y_i}\left(\frac{\partial T_{ij}}{\partial y_j}\frac{1}{r}\right)\right] dV + \int_V \frac{\partial}{\partial x_i}\left(\frac{1}{r}\right)\left[\frac{\partial T_{ij}}{\partial y_j}\right] dV \\
= & \int_V \left[\frac{\partial}{\partial y_i}\left(\frac{\partial T_{ij}}{\partial y_j}\frac{1}{r}\right)\right] dV + \int_V \frac{\partial}{\partial x_i}\left(\frac{1}{r}\left[\frac{\partial T_{ij}}{\partial y_j}\right]\right) dV \\
= & \int_V \left[\frac{\partial}{\partial y_i}\left(\frac{\partial T_{ij}}{\partial y_j}\frac{1}{r}\right)\right] dV + \frac{\partial}{\partial x_i}\int_V \left(\frac{1}{r}\left[\frac{\partial T_{ij}}{\partial y_j}\right]\right) dV \\
= & \int_V \left[\frac{\partial}{\partial y_i}\left(\frac{\partial T_{ij}}{\partial y_j}\frac{1}{r}\right)\right] dV + \frac{\partial}{\partial x_i}\left(\int_V \left(\left[\frac{\partial (T_{ij}/r)}{\partial y_j}\right] dV - \frac{\partial (1/r)}{\partial y_j}[T_{ij}]\right)\right) dV \\
= & \int_V \left[\frac{\partial}{\partial y_i}\left(\frac{\partial T_{ij}}{\partial y_j}\frac{1}{r}\right)\right] dV + \frac{\partial}{\partial x_i}\int_V \left[\frac{\partial (T_{ij}/r)}{\partial y_j}\right] dV + \frac{\partial}{\partial x_i}\int_V \frac{\partial (1/r)}{\partial x_j}[T_{ij}] dV \\
= & \int_V \left[\frac{\partial}{\partial y_i}\left(\frac{\partial T_{ij}}{\partial y_j}\frac{1}{r}\right)\right] dV + \frac{\partial}{\partial x_i}\int_V \left[\frac{\partial (T_{ij}/r)}{\partial y_j}\right] dV + \frac{\partial}{\partial x_i}\int_V \frac{\partial ([T_{ij}]/r)}{\partial x_j} dV \\
= & \int_V \left[\frac{\partial}{\partial y_i}\left(\frac{\partial T_{ij}}{\partial y_j}\frac{1}{r}\right)\right] dV + \frac{\partial}{\partial x_i}\int_V \left[\frac{\partial (T_{ij}/r)}{\partial y_j}\right] dV + \frac{\partial^2}{\partial x_i \partial x_j}\int_V \frac{[T_{ij}]}{r} dV \\
= & \int_S n_i \left[\frac{\partial T_{ij}}{\partial y_j}\right]\frac{1}{r} dS + \frac{\partial}{\partial x_i}\int_S n_j \frac{[T_{ij}]}{r} dS + \frac{\partial^2}{\partial x_i \partial x_j}\int_V \frac{[T_{ij}]}{r} dV.
\end{aligned}
$$

On the other hand, the surface integral is developed as:

$$
\begin{aligned}
& \int_S \left(\frac{1}{r}\left[\frac{\partial \rho}{\partial n}\right] + \frac{[\rho]}{r^2}\frac{\partial r}{\partial n} + \frac{1}{a_0 r}\frac{\partial r}{\partial n}\left[\frac{\partial \rho}{\partial t}\right]\right) dS \\
= & \int_S n_i \left(\frac{1}{r}\left[\frac{\partial \rho}{\partial y_i}\right] + \frac{[\rho]}{r^2}\frac{\partial r}{\partial y_i} + \frac{1}{a_0 r}\frac{\partial r}{\partial y_i}\left[\frac{\partial \rho}{\partial t}\right]\right) dS \\
= & \int_S n_i \frac{1}{r}\left[\frac{\partial (\rho \delta_{ij})}{\partial y_j}\right] dS - \int_S n_i \left(\frac{[\rho]}{r^2}\frac{\partial r}{\partial x_i} + \frac{1}{a_0 r}\frac{\partial r}{\partial x_i}\left[\frac{\partial \rho}{\partial t}\right]\right) dS \\
= & \int_S n_i \frac{1}{r}\left[\frac{\partial (\rho \delta_{ij})}{\partial y_j}\right] dS + \int_S n_j \left(\frac{\partial}{\partial x_i}\left(\frac{1}{r}\left[\rho \delta_{ij}\right]\right)\right) dS.
\end{aligned}
$$

The last identity comes from the use of:

$$
\frac{\partial}{\partial x_i}\left(\frac{1}{r}F(t - \frac{r}{a_0})\right) = -\left(\frac{1}{r^2}F + \frac{1}{a_0 r}F'\right)\frac{\partial r}{\partial x_i}.
$$

Replacing the expressions for the volume and surface integral deduced above and using the momentum equation, Equation 2.9 becomes

$$\begin{aligned}
\rho - \rho_0 &= \frac{1}{4\pi a_0^2}\frac{\partial^2}{\partial x_i \partial x_j}\int_V \frac{[T_{ij}]}{r}dV + \frac{1}{4\pi a_0^2}\int_S n_i \frac{1}{r}\frac{\partial}{\partial y_j}[(\rho v_i v_j + p_{ij} - \tau_{ij})]dS \\
&+ \frac{1}{4\pi a_0^2}\frac{\partial}{\partial x_i}\int_S n_j \frac{1}{r}[(\rho v_i v_j + p_{ij} - \tau_{ij})]dS \\
&= \frac{1}{4\pi a_0^2}\frac{\partial^2}{\partial x_i \partial x_j}\int_V \frac{[T_{ij}]}{r}dV - \frac{1}{4\pi a_0^2}\int_S n_i \frac{1}{r}\frac{\partial \rho v_i}{\partial t}dS \\
&+ \frac{1}{4\pi a_0^2}\frac{\partial}{\partial x_i}\int_S n_j \frac{1}{r}[p_{ij} - \tau_{ij}]dS.
\end{aligned}$$

Finally, considering that the surface is impermeable, i.e, $n_i v_i = 0$:

$$\boxed{\rho(\mathbf{x}) - \rho_0 = \frac{1}{4\pi a_0^2}\frac{\partial^2}{\partial x_i x_j}\int_V \frac{[T_{ij}]}{r}dV + \frac{1}{4\pi a_0^2}\frac{\partial}{\partial x_i}\int_S \frac{n_j}{r}[p_{ij} - \tau_{ij}]dS.} \tag{B.1}$$

Last equation is known as the Curle's solution for the Lighthill's system affected by a solid boundary.

B.1. Curle's Solution Modification

The simplification of Equation B.1 makes use of the following properties:

1. The fluid is isentropic, i.e,

$$\rho - \rho_0 = (p - p_0)/a_0^2. \tag{B.2}$$

2. Being $r = |\mathbf{x} - \mathbf{y}|$,

$$\frac{\partial r}{\partial x_i} = \frac{x_i - y_i}{r} := l_i.$$

$\mathbf{l} = (l_1, l_2, l_3)$ is a unitary vector pointing from the source point to the observational point. Its spatial derivative is calculated as:

$$\frac{\partial l_j}{\partial x_i} = \frac{\partial((x_j - y_j)/r)}{\partial x_i} = \frac{1}{r}\frac{\partial(x_j - y_j)}{\partial x_i} - \frac{1}{r^2}\frac{\partial r}{\partial x_i}(x_j - y_j) = \frac{1}{r}(\delta_{ij} - l_i l_j). \tag{B.3}$$

3. Being q a generic function of $\tau = t - \frac{r}{v}$,

$$\frac{\partial q(\tau)}{\partial x_i} = \frac{\partial q}{\partial \tau}\frac{\partial \tau}{\partial x_i} = \frac{\partial q}{\partial \tau}\frac{\partial \tau}{\partial r}\frac{\partial r}{\partial x_i} = \frac{-1}{a_0} l_i \frac{\partial q}{\partial \tau}.$$

4. $\frac{\partial r}{\partial \tau} = -a_0$;

5. Viscous terms are negligible, $\tau_{ij} = 0$.

Using the expression B.2, Equation B.1 becomes

$$p(\mathbf{x}) - p_0 = \frac{1}{4\pi}\frac{\partial^2}{\partial x_i x_j}\int_V \frac{[T_{ij}]}{r} dV + \frac{1}{4\pi}\frac{\partial}{\partial x_i}\int_S \frac{n_j}{r}[p_{ij}] dS.$$

Using the rest of the properties mentioned above, last expression can be developed as:

$$\begin{aligned}
& p(\mathbf{x},t) - p_0 \\
= \; & \frac{1}{4\pi}\frac{\partial}{\partial x_i}\int_V \frac{-l_j}{a_0}\left(\frac{1}{r}\frac{\partial [T_{ij}]}{\partial \tau} - \frac{1}{r^2}\frac{\partial r}{\partial \tau}[T_{ij}]\right) dV + \frac{1}{4\pi}\int_S \frac{-l_i n_j}{a_0}\left(\frac{1}{r}[\dot{p}_{ij}] - \frac{1}{r^2}[p_{ij}]\frac{\partial r}{\partial \tau}\right) dS \\
= \; & \frac{1}{4\pi}\frac{\partial}{\partial x_i}\int_V \left(\frac{-l_j}{r a_0}[\dot{T}_{ij}] - \frac{l_j}{r^2}[T_{ij}]\right) dV + \frac{1}{4\pi}\int_S -l_i n_j \left(\frac{1}{r a_0}[\dot{p}_{ij}] + \frac{1}{r^2}[p_{ij}]\right) dS \\
= \; & \frac{1}{4\pi}\int_V \left(\frac{l_i l_j}{a_0^2}\left(\frac{1}{r}[\ddot{T}_{ij}] + \frac{a_0}{r^2}[\dot{T}_{ij}]\right) + \frac{l_i l_j}{a_0}\left(\frac{1}{r^2}[\dot{T}_{ij}] + \frac{2a_0}{r^3}[T_{ij}]\right)\right. \\
- \; & \left.\frac{\partial l_j}{\partial x_i}\left(\frac{1}{r a_0}[\dot{T}_{ij}] + \frac{1}{r^2}[T_{ij}]\right)\right) dV + \frac{1}{4\pi}\int_S -l_i n_j \left(\frac{1}{r a_0}[\dot{p}_{ij}] + \frac{1}{r^2}[p_{ij}]\right) dS \\
= \; & \frac{1}{4\pi}\int_V \left(\frac{l_i l_j}{a_0^2 r}[\ddot{T}_{ij}] + 2\frac{l_i l_j}{a_0 r^2}[\dot{T}_{ij}] + \frac{2 l_i l_j}{r^3}[T_{ij}]\right. \\
- \; & \left.\frac{\partial l_j}{\partial x_i}\left(\frac{1}{r a_0}[\dot{T}_{ij}] + \frac{1}{r^2}[T_{ij}]\right)\right) dV + \frac{1}{4\pi}\int_S -l_i n_j \left(\frac{1}{r a_0}[\dot{p}_{ij}] + \frac{1}{r^2}[p_{ij}]\right) dS.
\end{aligned}$$

Finally, using the expression derived for $\frac{\partial l_j}{\partial x_i}$ in Equation B.3:

$$\boxed{\begin{aligned} p(\mathbf{x},t) - p_0 = & \frac{1}{4\pi}\int_V \left(\frac{l_i l_j}{a_0^2 r}[\ddot{T}_{ij}] + \frac{3 l_i l_j - \delta_{ij}}{a_0 r^2}[\dot{T}_{ij}] + \frac{3 l_i l_j - \delta_{ij}}{r^3}[T_{ij}]\right) dV \\ & + \frac{1}{4\pi}\int_S -l_i n_j \left(\frac{1}{r a_0}[\dot{p}_{ij}] + \frac{1}{r^2}[p_{ij}]\right) dS. \end{aligned}}$$

May the reader notice that $\dot{F}$ stands for $\frac{\partial F}{\partial \tau}$.

C

FW-H's Analogy

In this Appendix the solution to the inhomogeneous wave equation proposed by Fwocs-Williams Hawkings is derived. To this aim, the following proposition from convolution algebra [76] is used:

Proposition 2. *Given two linear operators L_1, L_2 and two continuous functions $g(\boldsymbol{x},t)$, $h(\boldsymbol{x},t)$ satisfying $L_1 g = L_2 h$, then*

$$g(\boldsymbol{x},t) = L_2 \int h(\boldsymbol{y},t) G(\boldsymbol{x}\text{-}\boldsymbol{y}, t-\tau) d\boldsymbol{y} d\tau,$$

where G satisfies $L_1 G = \delta$.

Last proposition gives the solution to Equation 2.17 with G being the Green's function:

$$G(r, t-\tau) = \frac{\delta(r - a_0(t-\tau))}{4\pi a_0 r},$$

$$\begin{aligned} \rho(\mathbf{x},t) - \rho_0 = & \frac{\partial^2}{\partial x_i \partial x_j} \int_\infty (T'_{ij} H(f))(\mathbf{y},\tau) \frac{\delta(r - a_0(t-\tau))}{4\pi a_0 r} dV d\tau \\ & - \frac{\partial}{\partial x_i} \int_\infty (F_i |\nabla f| \delta(f))(\mathbf{y},\tau) \frac{\delta(r - a_0(t-\tau))}{4\pi a_0 r} dV d\tau \\ & + \frac{\partial}{\partial t} \int_\infty (Q |\nabla f| \delta(f))(\mathbf{y},\tau) \frac{\delta(r - a_0(t-\tau))}{4\pi a_0 r} dV d\tau. \end{aligned} \tag{C.1}$$

When the surface is in motion, the source terms and the function f is better represented in a coordinate system moving with the surface: $y_i = y_i^* + v_i \tau$ and $u_i = u_i^* + v_i$.

Before continuing, it should be noted that,

$$\frac{\partial r}{\partial \tau} = \frac{\partial r}{\partial y_j}\frac{\partial y_j}{\partial \tau} = -\frac{x_j - y_j}{r}v_j = -l_j vj.$$

Thus, defining $g(\tau) = r - a_0(t-\tau)$,

$$dg = dr + a_0 d\tau = (a_0 - l_j v_j)d\tau.$$

The replacement of $d\tau$ in Equation C.1 after the aforementioned change of coordinates:

$$\begin{aligned}\rho(\mathbf{x},t) - \rho_0 = &\frac{\partial^2}{\partial x_i \partial x_j}\int_\infty \left(T'^*_{ij} H(f^*)\right)(\mathbf{y}^*,\tau)\frac{\delta(g)}{4\pi a_0 r(a_0 - l_j v_j)}dVdg \\ &-\frac{\partial}{\partial x_i}\int_\infty (F_i^*|\nabla f^*|\delta(f*))(\mathbf{y}^*,\tau)\frac{\delta(g)}{4\pi a_0 r(a_0 - ljv_j)}dVdg \\ &+\frac{\partial}{\partial t}\int_\infty (Q^*|\nabla f^*|\delta(f^*))(\mathbf{y}^*,\tau)\frac{\delta(r - a_0(t-\tau))}{4\pi a_0 r(a_0 - ljv_j)}dVdg.\end{aligned}$$

Integrating over dg:

$$\begin{aligned}\rho(\mathbf{x},t) - \rho_0 = &\frac{1}{4\pi a_0^2}\frac{\partial^2}{\partial x_i \partial x_j}\int_\infty \left[\frac{T'^*_{ij} H(f^*)}{r(1 - \frac{ljv_j}{a_0})}\right]dV \\ &-\frac{1}{4\pi a_0^2}\frac{\partial}{\partial x_i}\int_\infty \left[\frac{F_i^*}{r(1 - \frac{ljv_j}{a_0})}|\nabla f^*|\delta(f*)\right]dV \\ &+\frac{1}{4\pi a_0^2}\frac{\partial}{\partial t}\int_\infty \left[\frac{Q^*}{r(1 - \frac{ljv_j}{a_0})}|\nabla f^*|\delta(f^*)\right]dV\end{aligned} \tag{C.2}$$

where $[*]$ indicates the evaluation of the argument at the retarded time $\tau = t - r/a_0$, which is equivalent to $g(\tau) = 0$.

Finally, to simplify Equation C.2 the following theorem from algebra is used:

$$\int_\infty h(\mathbf{z})\delta(f(\mathbf{z}))dV(\mathbf{z}) = \int_S \frac{h(\hat{z})}{|\nabla f|}dS,$$

where S is the surface for which $f(\hat{z}) = 0$. Therefore, defining,

$$\begin{aligned} T'^*_{ij} &= \rho(u_i^* + v_i)(u_j^* + v_j) - \tau_{ij}^* + (p - a_0^2(\rho - \rho_\infty))\delta_{ij}, \\ F_i^* &= -(\rho(u_i^* + v_i)u_j^* + p\delta_{ij} - \tau_{ij}^*)n_j, \\ Q^* &= -(\rho_\infty v_i + \rho u_i^*)n_i, \end{aligned}$$

Equation C.2 becomes

$$\begin{aligned}\rho(\mathbf{x},t)-\rho_0 = &\frac{1}{4\pi a_0^2}\frac{\partial^2}{\partial x_i \partial x_j}\int_V \frac{[T_{ij}'^*]}{r(1-\frac{ljv_j}{a_0})}dV \\ &-\frac{1}{4\pi a_0^2}\frac{\partial}{\partial x_i}\int_S \frac{[F_i^*]}{r(1-\frac{ljv_j}{a_0})}dS \\ &+\frac{1}{4\pi a_0^2}\frac{\partial}{\partial t}\int_S \frac{[Q^*]}{r(1-\frac{ljv_j}{a_0})}dS.\end{aligned}$$

May the reader additionally notice that:

1. $\partial/\partial y_i = \partial/\partial y_i^*$, $\partial/\partial u_i = \partial/\partial u_i^*$ and $\tau_{ij} = \tau_{ij}^*$.
2. $\rho_\infty H(f) = \rho_0$.
3. The integration all over the space of a function multiplied by $H(f)$ is equivalent to integrate the function only where $H(f)$ is not null, i.e, in V.

Bibliography

[1] H. Schlichting and K. Gersten, *Boundary layer theory*. Springer, 2016.

[2] J. Ask and L. Davidson, "Sound generation and radiation of an open two–dimensional cavity," *AIAA J*, vol. 47, no. 6, pp. 1337–1349, 2009.

[3] C. Eriksson, G. Pershagen, and M. Nilsson, "Biological mechanisms related to cardiovascular and metabolic effects by environmental noise." World Health Organization, Aug 2018. [Online]. Available: http://www.euro.who.int/en/health-topics/environment-and-health/noise/publications/2018/biological-mechanisms-related-to-cardiovascular-and-metabolic-effects-by-environmental-noise

[4] M. Murayama, Y. Yokokawa, K. Yamamoto, and T. Hirai, "Computational study of low-noise fairings around tire-axle region of a two-wheel main landing gear," *Computers & Fluids*, vol. 85, pp. 114–124, 2013.

[5] R. V. de Abreu, N. Jansson, and J. Hoffman, "Computation of aeroacoustic sources for a gulfstream g550 nose landing gear model using adaptive fem," *Computers & Fluids*, vol. 124, pp. 136–146, 2016.

[6] M. Zhu, C. P. Arroyo, A. F. Pouangué, M. Sanjosé, and S. Moreau, "Isothermal and heated subsonic jet noise using large eddy simulations on unstructured grids," *Computers & Fluids*, vol. 171, pp. 166–192, 2018.

[7] M. Angelino, H. Xia, and G. J. Page, "Influence of grid resolution on the spectral characteristics of noise radiated from turbulent jets: Sound pressure fields and their decomposition," *Computers & Fluids*, vol. 196, p. 104343, 2020.

[8] H. Kim, Z. Hu, and D. Thompson, "Numerical investigation of the effect of various high-speed train roof configurations on aerodynamic noise," in *25th AIAA/CEAS Aeroacoustics Conference*, 2019, p. 2645.

[9] M. Hartmann, J. Ocker, T. Lemke, A. Mutzke, V. Schwarz, H. Tokuno, R. Toppinga, P. Unterlechner, and G. Wickern, "Wind noise caused by the side-mirror

and a-pillar of a generic vehicle model," in *18th AIAA/CEAS Aeroacoustics Conference (33rd AIAA Aeroacoustics Conference)*, 2012, p. 2205.

[10] B. Khalighi, A. Snegirev, J. Shinder, S. Lupuleac, and K.-H. Chen, "Simulations of flow and noise generated by automobile outside rear-view mirrors," *International Journal of Aeroacoustics*, vol. 11, no. 1, pp. 137–156, 2012.

[11] F. Pérot, X. Gloerfelt, C. Bailly, J.-M. Auger, and H. Giardi, "Numerical prediction of the noise radiated by a cylinder," in *9th AIAA/CEAS Aeroacoustics Conference and Exhibit 2003*, 2003, p. 3240.

[12] H.-D. Yao, L. Davidson, and L.-E. Eriksson, "Noise radiated by low-reynolds number flows past a hemisphere at ma= 0.3," *Physics of Fluids*, vol. 29, no. 7, p. 076102, 2017.

[13] L. Erbig and M. Maihöfer, "A hybrid rans/les for automotive gap noise simulations," in *25th AIAA/CEAS Aeroacoustics Conference*, 2019, p. 2445.

[14] C. Bailly and D. Juve, "Numerical solution of acoustic propagation problems using linearized euler equations," *AIAA Journal*, vol. 38, no. 1, pp. 22–29, 2000.

[15] C. Bailly and C. Bogey, "An overview of numerical methods for acoustic wave propagation," in *European Conference on Computational Fluid Dynamics, ECCOMAS CFD, P. Wesseling, E. Onate, J. Périaux (Eds)*, 2006.

[16] R. Ewert and W. Schröder, "Acoustic perturbation equations based on flow decomposition via source filtering," *Journal of Computational Physics*, vol. 188, no. 2, pp. 365–398, 2003.

[17] M. J. Lighthill, "On sound generated aerodynamically. i. general theory," in *Proceedings of the Royal Society of London A: Mathematical, Physical and Engineering Sciences 1952*, vol. 211, no. 1107. The Royal Society, 1952, pp. 564–587.

[18] N. Curle, "The influence of solid boundaries upon aerodynamic sound," in *Proceedings of the Royal Society of London A: Mathematical, Physical and Engineering Sciences 1955*, vol. 231, no. 1187. The Royal Society, 1955, pp. 505–514.

[19] J. F. Williams and D. L. Hawkings, "Sound generation by turbulence and surfaces in arbitrary motion," *Philosophical Transactions of the Royal Society of London A: Mathematical, Physical and Engineering Sciences*, vol. 264, no. 1151, pp. 321–342, 1969.

[20] X. Gloerfelt, C. Bailly, and D. Juvé, "Direct computation of the noise radiated by a subsonic cavity flow and application of integral methods," *Journal of Sound and Vibration*, vol. 266, no. 1, pp. 119–146, 2003.

[21] J. Larsson, L. Davidson, M. Olsson, and L.-E. Eriksson, "Aeroacoustic investigation of an open cavity at low mach number," *AIAA Journal*, vol. 42, no. 12, pp. 2462–2473, 2004.

[22] J. Ask and L. Davidson, "An acoustic analogy applied to the laminar upstream flow over an open 2d cavity," *Comptes Rendus Mecanique*, vol. 333, no. 9, pp. 660–665, 2005.

[23] J. Larsson, L. Davidson, M. Olsson, and L.-E. Eriksson, "Aeroacoustic investigation of an open cavity at low mach number," *AIAA Journal*, vol. 42, no. 12, pp. 2462–2473, 2004.

[24] H. M. Frank and C.-D. Munz, "Direct aeroacoustic simulation of acoustic feedback phenomena on a side-view mirror," *Journal of Sound and Vibration*, vol. 371, pp. 132–149, 2016.

[25] J. A. Stratton, *Electromagnetic theory*. New York: McGraw Hill, 1941.

[26] F. Farassat and M. Myers, "Extension of kirchhoff's formula to radiation from moving surfaces," *Journal of Sound and Vibration*, vol. 123, no. 3, pp. 451–460, 1988.

[27] G. Kirchhoff, "Zur theorie der lichtstrahlen," *Annalen der Physik*, vol. 254, no. 4, pp. 663–695, 1883.

[28] W. C. van der Velden, A. van Zuijlen, A. de Jong, and H. Bijl, "Noise estimation of beveled trailing edges using an integral and boundary element method," in *54th AIAA Aerospace Sciences Meeting*, 2016, p. 0260.

[29] S. W. Rienstra and A. Hirschberg, "An introduction to acoustics," *Report IWDE*, pp. 92–06, 2001.

[30] M. S. Howe, "Trailing edge noise at low mach numbers," *Journal of Sound and Vibration*, vol. 225, no. 2, pp. 211–238, 1999.

[31] Y. Sun, Q. Liu, L. N. Cattafesta III, L. S. Ukeiley, and K. Taira, "Effects of sidewalls and leading-edge blowing on flows over long rectangular cavities," *AIAA Journal*, vol. 57, no. 1, pp. 106–119, 2018.

[32] H. Lai and K. H. Luo, "A three-dimensional hybrid les-acoustic analogy method for predicting open-cavity noise," *Flow, turbulence and Combustion*, vol. 79, no. 1, pp. 55–82, 2007.

[33] T. Kuhn, "Zonal large eddy simulation of active open cavity noise using a high order discontinuous galerkin method," in *25th AIAA/CEAS Aeroacoustics Conference*, 2019, p. 2465.

[34] J. C. Hardin and D. S. Pope, "Sound generation by flow over a two-dimensional cavity," *AIAA Journal*, vol. 33, no. 3, pp. 407–412, 1995.

[35] G. A. Bres and T. Colonius, "Three-dimensional instabilities in compressible flow over open cavities," *Journal of Fluid Mechanics*, vol. 599, pp. 309–339, 2008.

[36] T. M. Faure, P. Adrianos, F. Lusseyran, and L. Pastur, "Visualizations of the flow inside an open cavity at medium range reynolds numbers," *Experiments in Fluids*, vol. 42, no. 2, pp. 169–184, 2007.

[37] M. Gharib and A. Roshko, "The effect of flow oscillations on cavity drag," *Journal of Fluid Mechanics*, vol. 177, pp. 501–530, 1987.

[38] T. Colonius, A. Basu, and C. Rowley, "Numerical investigation of the flow past a cavity," in *5th AIAA/CEAS Aeroacoustics Conference and Exhibit 1999*, 1999, p. 1912.

[39] C. W. Rowley, T. Colonius, and A. J. Basu, "On self-sustained oscillations in two-dimensional compressible flow over rectangular cavities," *Journal of Fluid Mechanics*, vol. 455, pp. 315–346, 2002.

[40] R. Martin, M. Soria, O. Lehmkuhl, A. Duben, and A. Gorobets, "Noise radiated by an open cavity at low mach number: Effect of the cavity oscillation mode," *International Journal of Aeroacoustics*, 2019.

[41] V. Suponitsky, E. Avital, and M. Gaster, "On three-dimensionality and control of incompressible cavity flow," *Physics of Fluids*, vol. 17, no. 10, p. 104103, 2005.

[42] V. Sarohia and P. Massier, "Control of cavity noise," *Journal of Aircraft*, vol. 14, no. 9, pp. 833–837, 1977.

[43] S. McGrath and L. Shaw, Jr, "Active control of shallow cavity acoustic resonance," in *Fluid Dynamics Conference*, 1996, p. 1949.

[44] J. Mendoza and K. Ahuja, "Cavity noise control through upstream mass injection from a coanda surface," in *Aeroacoustics Conference*, 1996, p. 1767.

[45] J. Hsu and K. Ahuja, "Cavity noise control using helmholtz resonators," in *Aeroacoustics Conference*, 1996, p. 1675.

[46] A. M. Lamp and N. Chokani, "Computation of cavity flows with suppression using jet blowing," *Journal of Aircraft*, vol. 34, no. 4, pp. 545–551, 1997.

[47] D. Fabris and D. Williams, "Experimental measurements of cavity and shear layer response to unsteady bleed forcing," in *37th Aerospace Sciences Meeting and Exhibit*, 1999, p. 605.

[48] A. J. Saddington, V. Thangamani, and K. Knowles, "Comparison of passive flow control methods for a cavity in transonic flow," *Journal of Aircraft*, vol. 53, no. 5, pp. 1439–1447, 2016.

[49] K. Knowles, B. Khanal, D. Bray, and P. Geraldes, "Passive control of cavity instabilities and noise," in *27th International congress of the aeronautical sciences*, 2010.

[50] K. Zhao, Y. Liang, T. Yue, Y. Wang, and G. J. Bennett, "Rectangular cavity flow noise suppression using chevron treatment to the front edge at subsonic speeds," in *25th AIAA/CEAS Aeroacoustics Conference*, 2019, p. 2693.

[51] M. Shaaban and A. Mohany, "Passive control of flow-excited acoustic resonance in rectangular cavities using upstream mounted blocks," *Experiments in Fluids*, vol. 56, no. 4, p. 72, 2015.

[52] S. Mancini, A. Kolb, I. Gonzalez-Martino, and D. Casalino, "Effects of wall modifications on pressure oscillations in high-subsonic and supersonic flows over rectangular cavities," in *25th AIAA/CEAS Aeroacoustics Conference*, 2019, p. 2692.

[53] J. Pereira and J. Sousa, "Influence of impingement edge geometry on cavity flow oscillations," *AIAA Journal*, vol. 32, no. 8, pp. 1737–1740, 1994.

[54] Q. Liu and F. Gómez, "Role of trailing-edge geometry in open cavity flow control," *AIAA Journal*, vol. 57, no. 2, pp. 876–878, 2018.

[55] L. L. Shaw, "Suppression of aerodynamically induced cavity pressure oscillations," *The Journal of the Acoustical Society of America*, vol. 66, no. 3, pp. 880–884, 1979.

[56] L. S. Ukeiley, M. K. Ponton, J. M. Seiner, and B. Jansen, "Suppression of pressure loads in cavity flows," *AIAA Journal*, vol. 42, no. 1, pp. 70–79, 2004.

[57] M. Stanek, J. Ross, J. Odedra, and J. Peto, "High frequency acoustic suppression-the mystery of the rod-in-crossflow revealed," in *41st Aerospace Sciences Meeting and Exhibit*, 2003, p. 7.

[58] J. Hao, M. Wang, M. Ji, and K. Wang, "Flow noise induced by small gaps in low-mach-number turbulent boundary layers," *Physics of Fluids*, vol. 25, no. 11, p. 110821, 2013.

[59] M. Vázquez, G. Houzeaux, S. Koric, A. Artigues, J. Aguado-Sierra, R. Arís, D. Mira, H. Calmet, F. Cucchietti, H. Owen *et al.*, "Alya: Multiphysics engineering simulation toward exascale," *Journal of Computational Science*, vol. 14, pp. 15–27, 2016.

[60] S. Charnyi, T. Heister, M. A. Olshanskii, and L. G. Rebholz, "On conservation laws of navier–stokes galerkin discretizations," *Journal of Computational Physics*, vol. 337, pp. 289–308, 2017.

[61] R. Codina, "Pressure stability in fractional step finite element methods for incompressible flows," *Journal of Computational Physics*, vol. 170, no. 1, pp. 112–140, 2001.

[62] L. Jofre, O. Lehmkuhl, J. Ventosa, F. X. Trias, and A. Oliva, "Conservation properties of unstructured finite-volume mesh schemes for the navier-stokes equations," *Numerical Heat Transfer, Part B: Fundamentals*, vol. 65, no. 1, pp. 53–79, 2014.

[63] O. Lehmkuhl, G. Houzeaux, H. Owen, G. Chrysokentis, and I. Rodriguez, "A low-dissipation finite element scheme for scale resolving simulations of turbulent flows," *Journal of Computational Physics*, vol. 390, pp. 51–65, 2019.

[64] F. Capuano, G. Coppola, L. Rández, and L. de Luca, "Explicit runge–kutta schemes for incompressible flow with improved energy-conservation properties," *Journal of Computational Physics*, vol. 328, pp. 86–94, 2017.

[65] A. Gorobets, "Parallel algorithm of the noisette code for cfd and caa simulations," *Lobachevskii Journal of Mathematics*, vol. 39, no. 4, pp. 524–532, 2018.

[66] P. Bakhvalov and T. Kozubskaya, "Ebr-weno scheme for solving gas dynamics problems with discontinuities on unstructured meshes," *Computers & Fluids*, vol. 157, pp. 312–324, 2017.

[67] A. Vreman, "An eddy-viscosity subgrid-scale model for turbulent shear flow: Algebraic theory and applications," *Physics of fluids*, vol. 16, no. 10, pp. 3670–3681, 2004.

[68] J. Fröhlich, C. P. Mellen, W. Rodi, L. Temmerman, and M. A. Leschziner, "Highly resolved large-eddy simulation of separated flow in a channel with streamwise periodic constrictions," *Journal of Fluid Mechanics*, vol. 526, pp. 19–66, 2005.

[69] U. Piomelli and J. R. Chasnov, "Large-eddy simulations: theory and applications," in *Turbulence and transition modelling*. Springer, 1996, pp. 269–336.

[70] V. Koschatzky, J. Westerweel, and B. Boersma, "A study on the application of two different acoustic analogies to experimental piv data," *Physics of Fluids*, vol. 23, no. 6, p. 065112, 2011.

[71] J. Rossiter, "Wind tunnel experiments on the flow over rectangular cavities at subsonic and transonic speeds," Ministry of Aviation; Royal Aircraft Establishment; RAE Farnborough, Tech. Rep., 1964.

[72] N. R. Lomb, "Least-squares frequency analysis of unequally spaced data," *Astrophysics and space science*, vol. 39, no. 2, pp. 447–462, 1976.

[73] J. D. Scargle, "Studies in astronomical time series analysis. ii-statistical aspects of spectral analysis of unevenly spaced data," *The Astrophysical Journal*, vol. 263, pp. 835–853, 1982.

[74] H. Fletcher and W. A. Munson, "Loudness, its definition, measurement and calculation," *Bell System Technical Journal*, vol. 12, no. 4, pp. 377–430, 1933.

[75] U. Michel, "History of acoustic beamforming," in *1st. Berlin Beamforming Conference 2006*, 2006.

[76] L. Bikulciene and Z. Navickas, "Expressions of solutions of linear partial differential equations using algebraic operators and algebraic convolution." in *NAA*. Springer, 2008, pp. 208–215.